

High-Aspect Ratio Structures in
Light-Absorbers and
Electrocatalysts for Solar Fuels
Devices

Thesis by
Paul Andrew Kempler

In Partial Fulfillment of the Requirements for
the degree of
Doctor of Philosophy

The logo for the California Institute of Technology (Caltech), featuring the word "Caltech" in a bold, orange, sans-serif font.

CALIFORNIA INSTITUTE OF TECHNOLOGY
Pasadena, California

2020
(Defended September 8, 2020)

© 2020

Paul Andrew Kempler
ORCID: 0000-0003-3909-1790

ACKNOWLEDGEMENTS

I am grateful to Prof. Mark Davis, Prof. John Seinfeld, and Prof. Konstantinos Giapis, for serving on my Thesis Committee and contributing their time and feedback. Their early contributions following my Candidacy Exam were valuable in providing focus to this project. Additional thanks to Kat, John, and Lori for their feedback on the introductory chapter.

I arrived at Caltech in large part because of my undergraduate mentors within the Vanderbilt Chemical Engineering program. Prof. Paul Laibinis spent hours in the lab with me during the start of my independent study project; his teaching and advising instilled my interest in thermodynamics and surface chemistry. Without his encouragement, I would not have applied to Caltech. Prof. Kane Jennings was an excellent mentor during the summer I researched at Vanderbilt. He gave me room for creativity on a project that sent me to my first conference and led to my first publication. I owe much to Faizan Zubair and Ian Njoroge, who mentored and supervised my novice undergraduate self. They put up with both my messiness and exuberance as I learned how to do science right and their advice prepared well for graduate school.

I was welcomed into the Lewis group by a group of outstanding graduate students and postdocs. Sonja Francis and Dan Torelli designed my first project when I knew nothing about electrochemistry and immediately worked to integrate me within the large group. Sonja, your continued encouragement and mentoring are a constant reminder that I made the right decision to join. Noah, thank you for teaching me how to clean and functionalize

Si surfaces and for being a model mentor when sharing your expertise. Thank you Mita Dasog and Azhar Carim for starting me on my first Si microwires project and being patient teachers while also giving me the freedom to explore my own interests. Azhar has been and continues to be a wealth of scientific and institutional knowledge and helped me put the (photo) in (photo)electrochemistry.

I am particularly grateful to Mita for introducing me to Rob Coridan. Rob has been a second advisor to me on all things related to bubbles and I am grateful to have had the chance to collaborate with him. His high-speed videos taught us all a lot about the dynamics of gas evolution. My primary collaborator and coconspirator in all things silicon was Sisir Yalamanchili. I am ever grateful for him sharing his expertise in navigating the KNI and getting me involved on his interesting projects. Sisir, I aspire towards your work ethic and optimism in research. Katie Chen worked on a number of bubbles models that have provided insight into mass transport within microwire arrays. Her papers have taught me a lot about the inner workings of solar fuels devices. Matthias Richter was instrumental in enabling the Si/Cu photocathode project and I am grateful to have been able to rely on his instrumental wizardry during my time in graduate school. Harold, Kathleen, and I also had the pleasure of working with Jeff Cammerata at Lockheed Martin, who was an engaging industry partner for an exploratory project involving Si microcone arrays.

The Lewis Group is proof of strength in numbers. To the graduate students who saw me in: Noah Plymale, Adam Nielander, Josh Wiensch, Stefan Omelchenko, Jingjing Jiang, Xinghao Zhou, Fadl Saadi, Paul Nuñez, Jonathan Thompson, Ethan Simonoff,

Azhar Carim, Michael Lichterman, Ivan Moreno-Hernandez, Annelise Thompson, Dan Torelli, and Kyra Lee; as well as knowledgeable postdocs Mita Dasog, Sonja Francis, Carlos Read, Jesús Velázquez, Ke Sun, Miguel Cabán-Acevedo, Burt Simpson, and Renata Bagley: thank you for sharing your wisdom and helping me find my footing.

To my cohort of graduate students, Katherine Rinaldi, Ellen Yan, and Pakpoom Buabthong: I couldn't have picked a better group of people to learn, work, and grow with over the last five years. Kat, you in particular have had a profound impact on my time in graduate school. It has been a pleasure to be your roommate, bandmate, desk-mate, teammate, travel-buddy, pet-parent, and friend. It is hard to picture a Caltech experience without your spark. I am so glad that Harold Fu and Zachary Ifkovits crossed department lines to join me as fellow ChemEs in the group. I am grateful that Kathleen Kennedy is carrying forward efforts on microwires and nanowires within the KNI. Thanks Michael Mazza, Katie Hamann, Weilai Yu, Madeline Meier, Maureen Morla, and Jackie Dowling for continuing to foster a motivated and positive scientific community. Our two newest group members, Sean Byrne and Jake Evans, exemplify the enthusiasm and curiosity that thrives in our group and I look forward to following the results of their projects.

An impressive cohort of chemical engineers, along with a number of caring, more experienced graduate students and TA's, got me through my first year at Caltech. Red, Kari, Zach, Stephanie, Xinyan, Xinran, and Malaney, I am grateful for all that I learned with you during our first year. I owe particular thanks to Red, who was an enthusiastic

peer-mentor. Their good-natured approach to problem solving got me through many challenging transport problem-sets.

I had the pleasure of working with a number of motivated undergraduates while working at Caltech Miguel Gonzalez, Gianmarco Terrones, Amar Bhardwaj, and Jillian Reed: your questions and fresh set of eyes in the lab kept me motivated and provided valuable insights. I look forward to following your promising careers as scientists and engineers.

The frisbee community within Los Angeles provided me with an athletic outlet to keep me healthy throughout graduate school. Thank you, Daryl, Radka, and Zach for welcoming me into Caltech Aftermath with open arms. Thank you, Bryce, for the hours of conversation travelling to and from tournaments—I've had a number of great teammates but I can't think of a better teammate than you. Thanks to all the members of Family Style over the years, of whom there are too many to personally name. You were all a dear part of my time spent in Los Angeles. I owe an extra thank you to Bustle, Jenny, Joe, and Annie for captaining me and/or captaining with me over the years. You have taught me to be more accountable, responsible, and caring as a leader.

I have been enriched by my time working with the Solar Energy Activity Laboratory (SEAL) under the direction of Michelle DeBoever and Five-Star Solar-Army General Prof. Harry Gray. Fadl got me started with SEAL and made each week an adventure. I took over the responsibilities of Lead Mentor from Sonja after she left Caltech

and have had the opportunity to work with a number of schools, San Marino, Alverno, and Franklin; teachers, Wyeth, Russell, Monica, and Jomel; and mentors, Fadl, Charlie, Madeline, and Axl. I learned so much about teaching and mentoring during my time with SEAL. I am ever grateful that Kitty Cahalan and the C.T.L.O. have worked hard to see that the program continues and can continue to provide research experiences to high school students.

I feel privileged to have been able to rely on the expertise of the staff within the Kavli Nanoscience Institute, with particular thanks to Guy DeRose for his dedication in maintaining a productive lab space—especially during the 2020 pandemic. Thank you, Nathan Lee, for maintaining the plasma systems and ALD. All but one of these chapters were only possible due to these instruments operating reliably throughout my time at Caltech. I am grateful to Rick Gerhart for preparing custom glassware and Mike Roy for preparing custom Teflon cells and aluminum heat-sinks. I also acknowledge instrumental support from the Molecular Materials Research Center in the Beckman Institute at Caltech.

Kimberly Papadantonakis and Bruce Brunschwig have served as additional advisors to me during my time at Caltech. Their presence improves the environment of the Lewis group in so many ways. Thank you, Kim, for your tough questions and willingness to challenge conventions. Kim helped me through my first, first-author manuscript and has taught me to be a better writer and researcher. Thank you, Bruce, for your untiring willingness to discuss models of bubble nucleation and mass transport and for providing feedback on my papers, proposals, and presentations. Bruce has motivated me to learn how

to express complex ideas simply in my writing. Thank you, Barbara Miralles, for everything you do to keep the gears turning and papers in press. You are patient and kind and we are so lucky to have you. For having overlapped with all of those people above in the Lewis group—and so much more—I am grateful to my advisor, Prof. Nathan Lewis. Thank you, Nate, for creating and continuing a special type of research environment that has allowed me to flourish. You are an inspiration to many and I feel privileged to be one of your advisees. You have consistently focused my ideas into meaningful concepts while giving me the time and space to explore new areas of research. The balance of global scope, creativity, and scientific rigor within the Lewis group is something I hope to carry forward.

Lastly, I must thank my family. To my mother, Dina, the original Dr. Kempler, I owe my life, my curiosity, and my joy. My mother raised me to measure the time it took to drive different routes from our house to elementary school (with error bars!) so we could be sure we were taking the fastest route. She taught me to experiment in the kitchen, in the ocean, and in the classroom. The spark I find when I go into lab comes from her. To my father, John, I owe my patience, my will, and my love of learning. He is my role model for always being involved in one-too-many things and having the time for one more conversation with one more friend. Such involvements kept me balanced, stable, and happy through grad school. That I inherited a small fraction of his ability to write for hours on end must be the only reason I finished this thesis. My step mother Cristi welcomed me as her son and has been a constant source of encouragement and wisdom. I am lucky to have grown up with a number of siblings, Summer, Cassie, Emma, and Kayden, who kept made my childhood fun and are continued sources of laughter and a reason to fly home.

ABSTRACT

Solar fuels devices produce hydrogen fuel from water and sunlight and address a critical societal need for inexpensive, long-duration energy storage. Such devices are prepared from combinations of light-absorbing semiconductors and catalysts to sunlight to drive thermodynamically uphill reactions. This dissertation puts forth strategies for controlling the three-dimensional structure of semiconductors, electrocatalysts, and the film of gas bubbles evolved on the top and bottom of a solar fuels device. High-aspect ratio features led to unexpected effects in semiconductor/electrocatalyst assemblies. Optical losses were decoupled from the mass-loading of cobalt phosphide and copper electrocatalysts integrated onto silicon microwire photocathodes for the photoelectrochemical generation of hydrogen and hydrocarbons, respectively. Anti-reflective silicon microcone arrays were patterned with continuous films of Pt or CoP particles with minimal reflection losses due to the catalyst films. Transparent metal films were prepared from nanostructured metal phosphides, a class of earth-abundant hydrogen evolution catalysts. Silicon microwire array (photo)electrode surfaces were used to force bubbles away from electrocatalyst surfaces, even when oriented against gravity, leading to sustained operation in the absence of external convection.

PUBLISHED CONTENT AND CONTRIBUTIONS

1. **Kempler, P. A.**, Gonzalez, M. A., Papadantonakis, K. M., & Lewis, N. S. (2018). Hydrogen evolution with minimal parasitic light absorption by dense Co–P catalyst films on structured p-Si photocathodes. *ACS Energy Letters*, 3(3), 612-617. <https://doi.org/10.1021/acseenergylett.8b00034>

P.A.K. prepared the samples, collected and analyzed the data, and assisted in the writing and the editing of the manuscript.

2. **Kempler, P. A.**, Richter, M. H., Cheng, W.H., Brunshwig, B.S., & Lewis, N.S. (2020). Si Microwire-Array Photocathodes Decorated with Cu Allow CO₂ Reduction with Minimal Parasitic Absorption of Sunlight. *ACS Energy Letters*, 5(8), 2528-2534. <https://doi.org/10.1021/acseenergylett.0c01334>

P.A.K. prepared the samples, collected and analyzed the data, and assisted in the writing and the editing of the manuscript.

3. Yalamanchili, S.,* **Kempler, P. A.**,* Papadantonakis, K. M., Atwater, H. A., & Lewis, N. S. (2019). Integration of electrocatalysts with silicon microcone arrays for minimization of optical and overpotential losses during sunlight-driven hydrogen evolution. *Sustainable Energy & Fuels*, 3(9), 2227-2236. <https://doi.org/10.1039/C9SE00294D>

P.A.K. assisted in collecting and analyzing the data, and assisted in the writing and the editing of the manuscript. *Equal Contributions.

4. **Kempler, P. A.**, Fu, H. J., Ifkovits, Z. P., Papadantonakis, K. M., & Lewis, N. S. (2020). Spontaneous Formation of > 90% Optically Transmissive, Electrochemically Active CoP Films for Photoelectrochemical Hydrogen Evolution. *The Journal of Physical Chemistry Letters*. 11(1), 14-20. <https://doi.org/10.1021/acs.jpcelett.9b02926>

P.A.K. prepared the samples, collected the photoelectrochemical data, collected the data for the optical characterization of the films, developed the film model for spectroscopic ellipsometry, and assisted in the writing and the editing of the manuscript.

5. **Kempler, P.A.**, Coridan, R.H., Lewis N.S. (2020). Effects of Bubbles on the Electrochemical Behavior of Hydrogen-Evolving Si Microwire Arrays Oriented Against Gravity. *Energy & Environmental Science*, 13, 1808-1817. <https://doi.org/10.1039/D0EE00356E>

P.A.K. prepared the samples, collected and analyzed the data, and assisted in the writing and the editing of the manuscript.

6. **Kempler, P. A.**, Ifkovits, Z.P., Yu. W., Carim, A.I., & Lewis, N.S. (2020). Optical and electrochemical effects of H₂ and O₂ bubbles at upward-facing Si photoelectrodes. *In preparation*

P.A.K. prepared the samples, collected and analyzed the data, and assisted in the writing and the editing of the manuscript.

TABLE OF CONTENTS

ACKNOWLEDGEMENTS.....	III
ABSTRACT.....	IX
PUBLISHED CONTENT AND CONTRIBUTIONS.....	X
LIST OF FIGURES, TABLES AND SCHEMES	XV
INTRODUCTION	1
1.1. STORING ENERGY FROM THE SUN	1
1.2. MATERIALS FOR PRODUCING SOLAR FUELS	3
1.3. INTEGRATION OF SEMICONDUCTORS AND ELECTROCATALYSTS	6
1.3.1 <i>Thesis statement</i>	6
1.3.2 <i>Light-management at high-aspect ratio Si</i>	8
1.3.3 <i>Light-management at high-aspect ratio CoP</i>	12
1.3.4 <i>Control of H₂ and O₂ bubbles at electrode surfaces</i>	13
1.3.5 <i>Summary and Outlook</i>	16
HYDROGEN EVOLUTION WITH MINIMAL PARASITIC LIGHT ABSORPTION BY DENSE CO-P CATALYST FILMS ON STRUCTURED P-SI PHOTOCATHODES.....	18
2.1 INTRODUCTION	18
2.2 EXPERIMENTAL METHODS.....	19
2.3 RESULTS.....	20
2.4 DISCUSSION	30
2.5 CONCLUSION	32
SI MICROWIRE-ARRAY PHOTOCATHODES DECORATED WITH CU ALLOW CO₂ REDUCTION WITH MINIMAL PARASITIC ABSORPTION OF SUNLIGHT.....	33
3.1 INTRODUCTION	33
3.2 EXPERIMENTAL METHODS.....	35

3.3	RESULTS.....	36
3.4	DISCUSSION.....	43
3.5	CONCLUSION.....	51
INTEGRATION OF ELECTROCATALYSTS WITH SILICON MICROCONE ARRAYS FOR MINIMIZATION OF OPTICAL AND OVERPOTENTIAL LOSSES DURING SUNLIGHT- DRIVEN HYDROGEN EVOLUTION.....		52
4.1	INTRODUCTION.....	52
4.2	EXPERIMENTAL METHODS.....	55
4.3	RESULTS AND DISCUSSION.....	56
4.3.1	<i>Homojunction Si photocathodes with sputtered Pt catalyst.....</i>	<i>56</i>
4.3.2	<i>Si photocathodes with electrodeposited Co-P catalyst.....</i>	<i>61</i>
4.4	CONCLUSION.....	71
SPONTANEOUS FORMATION OF >90% OPTICALLY TRANSMISSIVE, ELECTROCHEMICALLY ACTIVE COP FILMS FOR PHOTOELECTROCHEMICAL HYDROGEN EVOLUTION.....		72
5.1	INTRODUCTION.....	72
5.2	EXPERIMENTAL METHODS.....	73
5.3	RESULTS AND DISCUSSION.....	74
5.4	CONCLUSION.....	87
EFFECTS OF BUBBLES ON THE ELECTROCHEMICAL BEHAVIOR OF HYDROGEN- EVOLVING SI MICROWIRE ARRAYS ORIENTED AGAINST GRAVITY.....		88
6.1	INTRODUCTION.....	88
6.2	EXPERIMENTAL METHODS.....	90
6.3	RESULTS.....	92
6.3.1	<i>Electrochemical behavior of inverted cathodes.....</i>	<i>93</i>
6.3.2	<i>Physical characterization of bubble films.....</i>	<i>94</i>
6.3.3	<i>Mass transport properties of bubble films.....</i>	<i>100</i>

6.3.4	<i>Electrochemical impedance of bubble films</i>	102
6.4	DISCUSSION.....	106
6.5	CONCLUSION.....	111
OPTICAL AND ELECTROCHEMICAL EFFECTS OF H₂ AND O₂ BUBBLES AT UPWARD-FACING SI PHOTOELECTRODES		113
7.1	INTRODUCTION.....	113
7.2	EXPERIMENTAL METHODS.....	115
7.3	RESULTS.....	117
7.3.1	<i>N-Si/TiO₂/Ni Photoanodes in 1.0 M KOH(aq)</i>	117
7.3.2	<i>Upward facing p-Si Photocathodes in 0.50 M H₂SO₄(aq)</i>	126
7.3.3	<i>Ray-Tracing Simulations of Surface Attached Bubbles</i>	128
7.2.4	<i>Downward-Facing Photoelectrodes</i>	133
7.4	CONCLUSIONS.....	136
APPENDIX.....		137
A.1	GENERAL EXPERIMENTAL METHODS.....	137
A.2	SUPPORTING INFORMATION FOR CHAPTER 2.....	138
A.3	SUPPORTING INFORMATION FOR CHAPTER 3.....	138
A.4	SUPPORTING INFORMATION FOR CHAPTER 4.....	142
A.5	SUPPORTING INFORMATION FOR CHAPTER 5.....	145
A.6	SUPPORTING INFORMATION FOR CHAPTER 6.....	150
A.7	SUPPORTING INFORMATION FOR CHAPTER 7.....	152
REFERENCES.....		155

LIST OF FIGURES, TABLES AND SCHEMES

Scheme 1.1	Layered representation of the components required for a solar fuels device.....	5
Scheme 1.2	Comparison of methods for macroscale and microscale integration of light absorbers and membranes.....	7
Scheme 1.3	Plan-view and cross section representation of catalyst integration on a planar and microstructured semiconductor.....	10
Scheme 1.4	Orientation of a solar fuels device with respect to gravity and sunlight	15
Figure 2.1	Scanning-electron micrographs of photoelectrochemically deposited Co-P on Si	21
Table 2.1	Average figures of merit for different p-Si structures loaded with Co-P and tested at 100 mW cm ⁻² of simulated sunlight in 0.50 M H ₂ SO ₄ (aq)	22
Figure 2.2	Current-potential behavior of p-Si photocathodes with 400 mC cm ⁻² Co-P in 0.50 M H ₂ SO ₄ (aq) under 1 Sun illumination.....	24
Figure 2.3	Loss in photocurrent during deposition of Co-P onto Si; Correlation between measured photocurrent during deposition and short circuit current density during hydrogen evolution prior to dissolution of excess cobalt	26
Figure 2.4	Dark catalytic behavior of Co-P on planar and microwire n ⁺ -Si; Comparison of the behavior of a high loading of Co-P on planar Si with the behavior of p-Si microwires with an equivalent Co-P loading	28
Figure 2.5	Power-conversion efficiencies for top-performing Si/Co-P devices.....	30
Figure 3.1	Cell schematic for the photoelectrochemical deposition of Cu onto n ⁺ p-Si; Photoelectrochemical current-potential behavior of Si in the Cu deposition bath; Current versus charge passed during photoelectrochemical deposition of Cu.....	38
Figure 3.2	False-color scanning-electron micrograph images of Cu on deposited onto planar and microwire-array Si.....	39

Figure 3.3	Photoelectrochemical <i>J</i> - <i>E</i> behavior of n ⁺ p-Si microwire arrays decorated with Cu compared to the dark <i>J</i> - <i>E</i> behavior of electropolished Cu.....	40
Figure 3.4	Partial current versus potential behavior for (photo)electrochemical carbon dioxide reduction to carbon monoxide, methane, ethylene, and hydrogen	40
Figure 3.5	Evaluation of the stability of photoelectrochemical devices for carbon dioxide reduction.....	42
Figure 3.6	Scanning-electron micrograph of silicon microwire arrays decorated with Cu after 96 hours of continuous photoelectrochemical operation in aqueous potassium bicarbonate and simulated sunlight.....	43
Figure 3.7	Current-overpotential behavior for planar and microwire array electrocatalysts as a function of the Tafel slope; Current-potential behavior calculated from Equation 3.1 and Equation 3.2.....	46
Figure 3.8	Measurements of the rate of Pt cross-over via X-ray photoelectron spectroscopy, scanning-electron microscopy, and inductively coupled mass-spectroscopy	49
Figure 4.1	Scheme and scanning electron-micrograph representing the fabrication of platinum coated n ⁺ p-Si microcone array photocathodes	57
Figure 4.2	Effect of Pt loading on the current-potential behavior of various Si photocathodes in 0.50 M H ₂ SO ₄ (aq) under simulated sunlight	58
Figure 4.3	Scanning-electron micrographs of cobalt phosphide deposited onto silicon microcone array photocathodes, before and after testing; Polymer embedded Si microcone arrays after removal from the substrate.....	62
Figure 4.4	Current potential behavior of Si microcone array photocathodes in 0.50 M H ₂ SO ₄ (aq) under simulated sunlight, before and after deposition of CoP electrocatalyst	63
Figure 4.5	Extended photoelectrochemical testing of a Si/CoP microcone array photocathode in 0.50 M H ₂ SO ₄ (aq) under simulated sunlight.....	65
Figure 4.6	Spectral reflectance and absorbance measurements of bare and catalyst-decorated Si microcone arrays, in air and 0.50 M H ₂ SO ₄ (aq), respectively.....	66

Figure 4.7	Representative current-potential behavior of a polymer-embedded Si microcone array photocathode decorated with CoP and tested in 0.50 M H ₂ SO ₄ (aq) under simulated sunlight	68
Figure 5.1	Scanning-electron micrograph of a cross section of a CoP film before and after activation in 0.50 M H ₂ SO ₄ (aq); Atomic force microscopy images of a CoP film before and after activation in 0.50 M H ₂ SO ₄ (aq)	75
Figure 5.2	Dissolution rates of Co and P in 0.50 M H ₂ SO ₄ (aq) as measured via inductively-coupled plasma mass spectroscopy	75
Figure 5.3	In situ transmission versus wavelength measurements of a CoP film deposited on a FTO/Co surface and immersed in 0.50 M H ₂ SO ₄ (aq); Photocurrent versus charge density passed towards CoP deposition on a Si photocathode surface under high intensity illumination from a 625 nm source; Current-potential behavior of the Si/CoP photocathode in 0.50 M H ₂ SO ₄ (aq) under simulated sunlight.....	78
Figure 5.4	Current density versus time and potential versus time for Si/CoP photocathodes in 0.50 M H ₂ SO ₄ (aq) under simulated sunlight	79
Figure 5.5	Current-potential behavior for Si photocathodes decorated with Pt and CoP catalysts in 0.50 M H ₂ SO ₄ (aq) and under simulated sunlight.....	81
Figure 5.6	Characterization of CoP films on degenerately doped Si via spectroscopic ellipsometry; simulated optical properties of transparent metal films as a function of the void fraction and depolarization parameter	82
Table 5.1	Comparison of the optical properties of various transparent metal films measured at planar semiconductors	84
Figure 5.7	Binary scanning-electron micrograph image of a CoP film at Si after activation in 0.50 M H ₂ SO ₄ (aq) for 10 min; Change in the void fraction within a CoP film as a function of time as measured via spectroscopic ellipsometry and scanning-electron microscopy	86
Scheme 6.1	Monolithic, integrated, tandem solar fuels device showing the relationship between the gravitational vector and the optimal device orientation.....	89
Figure 6.1	Scanning-electron microscope images of platinized Si microwire arrays of various diameters and pitches.....	93

Figure 6.2	Comparison of the upward-facing and downward-facing electrochemical behaviors of planar and microstructured cathodes in 0.50 M H ₂ SO ₄ (aq).....	94
Figure 6.3	Comparison of fractional gas coverage of downward-facing planar and Si microwire array cathodes in 0.50 M H ₂ SO ₄ (aq)	96
Figure 6.4	Weighted mean bubble diameters at planar and Si microwire array cathodes; Number density of bubbles on electrode surfaces as a function of time	97
Figure 6.5	High-speed microscopy measurements of upward-facing cathodes in 0.50 M H ₂ SO ₄ (aq); Radius versus square root time of individual bubbles as measured from high-speed microscopy	99
Figure 6.6	Scheme of experimental procedure for diffusion-limited current experiments; Measured diffusion limited current density and calculated concentrated boundary layer length; Representative traces of gas bubbles at an inverted electrode.....	101
Figure 6.7	Potential versus time traces for planar platinum electrodes as a function of orientation with respect to gravity, overlaid with deviation in ohmic potential drop	103
Figure 6.8	Comparison of the steady-state current-potential behavior with simulated behavior as a function of gas layer thickness and concentration overpotential.	105
Figure 6.9	High speed microscope images recorded at an upward-facing microwire electrode evolving hydrogen in 0.50 M H ₂ SO ₄ (aq).....	108
Figure 7.1	Scheme of n-Si microwires coated with TiO ₂ and Ni; Scanning-electron micrographs of n-Si/TiO ₂ /Ni microwire arrays and a p-Si microwire array	118
Figure 7.2	Current-potential behavior of upward-facing planar and microwire array photoanodes in 1.0 M KOH under simulated sunlight; Images of planar and microwire array photoanodes; extended stability test of a planar photoanode in 1.0 M KOH(aq); Current-potential behavior of Si microwire photoanodes under elevated light intensity.....	120
Figure 7.3	Measurements of mass-transport velocities as the diffusion limited current density of ferrocyanide oxidation in 1.0 M KOH(aq) as a function of the photocurrent density at planar and microwire photoanodes; False color images of bubbles departing upward facing planar and microwire photoanodes	123

Figure 7.4	Current-potential behavior for upward-facing Si photocathodes in stagnant 0.50 M H ₂ SO ₄ (aq) and under simulated sunlight; Photocurrent versus time behavior of hydride-terminated and hydroxyl-terminated Si photocathodes in stagnant 0.50 M H ₂ SO ₄ (aq)	127
Figure 7.5	Photocurrent versus radial position profiles, as simulated via ray-tracing, for various bubble radii, contact angles, and coverages	130
Figure 7.6	Results of ray-tracing simulations at a single surface-attached bubble; Results of a ray tracing simulation at multiple surface-attached bubbles.....	131
Figure 7.7	Graphical representation of the scattering distance as a function of ray position at normal incidence on a surface attached bubble; Non-dimensional plot of the scattering distance versus radial position of a ray at normal incidence	132
Figure 7.8	Coverage versus photocurrent density for downward facing photoelectrodes; Images of the gas coverage at downward facing photoelectrodes; Photocurrent density versus time for downward facing photoelectrodes.....	134
Figure A.3.1	Plot of open circuit photovoltage versus the light limited photocurrent for Si photocathodes in a Cu plating bath.....	142
Figure A.5.1	Real and imaginary components of the complex index of refraction at as-deposited CoP as measured via spectroscopic ellipsometry	149
Figure A.5.2	Real and imaginary components of the dielectric function of CoP films as a function of charge passed during deposition and time spent in 0.50 M H ₂ SO ₄ (aq)	149
Figure A.6.1	Image sequence at 200 frames per second of an upward facing bubble evolving hydrogen in 0.50 M H ₂ SO ₄ (aq).....	152
Figure A.7.1	Scan-rate dependence of cyclic voltammograms of 10 mM ferrocyanide in 1.0 M KOH(aq) at Ni and Au electrodes	154
Figure A.7.2	Electrolyte absorbance at 420 nm versus ferricyanide concentration as measured as the anodic charge passed at a Ni wire	154

Chapter 1

INTRODUCTION

1.1. Storing Energy from the Sun

An international effort is needed to stabilize the increase in global mean temperatures caused by human-derived carbon dioxide (CO₂) emissions.¹ In order to reach the target of net-zero emissions by mid-century proposed by the IPCC, massive emissions reductions are required. Such reductions rest crucially society's ability to eliminate emissions from the electricity sector.²⁻³ First and foremost we need alternatives to obtaining energy from the combustion of underground carbon to CO₂. Sunlight is a nearly inexhaustible energy resource that emits no CO₂ and is available across the Earth's surface and can therefore address this need.⁴ Photovoltaic devices allow humans to harness energy from the sun as electrical power, but early applications were restricted to photodetectors and space power due to low power conversion efficiencies and high material costs.⁵ Substantial improvements in efficiency, coupled with falling materials costs from improved manufacturing of high-purity crystalline silicon, have led to a > 15-fold reduction in the cost of power purchase agreements for installed photovoltaics.⁶ Today, solar power is often the cheapest form of electricity generation, with 635 GW of photovoltaic systems have been installed worldwide and >95% of present-day production driven by modules prepared from inexpensive, crystalline-Si light absorbers.⁷⁻⁸

Existing electricity grids balance seasonal shifts in the supply and demand of electricity via the ramping up and down of fuel-burning power plants. Increasing penetration of intermittent energy resources, such as solar and wind, into large, net-zero emission electricity grids will require new technologies for storing electricity.⁹⁻¹⁰ Extended

periods (hundreds of days) of 100% renewable electricity generation, demonstrated in countries such as Costa Rica, have been limited to regions that obtain a large fraction of their electricity from hydropower.¹¹ Prodigious expansions to the capacity and deployment of hydropower have been invoked in plans for future 100% renewable grids for the United States, but such expansions may exceed the physical capacity of the country's rivers and reservoirs.¹² Reliable zero-carbon energy systems in regions without preexisting hydroelectric resources will require methods for storing renewable energy. Mechanical methods for energy storage, such as pumped hydro and compressed air storage, could be inexpensive but afford lower energy densities than (electro)chemical energy storage in fuels and batteries.⁹

The capital cost of building electricity storage can be determined by the cost of energy or the cost of power. Power determines what we can do with electricity (e.g. turn on a cell phone or drive a car), whereas energy determines how long your electricity will last. Present-day demand for electricity storage emphasizes the cost of power and round-trip efficiency, allowing lightweight lithium-ion cells to power our phones and electric vehicles. Reductions in the cost of energy stored, however, are needed to smooth the seasonal variations in the availability of wind and solar power.^{10, 13} The average price of lithium-ion batteries has fallen rapidly, along with improving lifetimes, but the cost per kilowatt-hour (energy) would need to fall by an additional two-orders of magnitude in order to address a need for energy storage lasting more than 10 hours.¹³ A closed-process that converted electricity into fuels for long term storage would be better poised to replace existing natural gas power processes.

Nature provides inspiration for our societal need for globally-available, inexpensive energy storage. All plants use water and sunlight to capture and convert CO₂ into molecules that store energy, in a process known as photosynthesis. Using energy from the sun to form fuels has been coined Artificial Photosynthesis. Pure water is an abundant and non-toxic natural resource that can serve as the substrate for a fuel-forming reaction in such a system. The water-splitting reaction leads to the formation of oxygen and hydrogen, a fuel that stores the energy required for the reaction within its chemical bonds.¹⁴ This energy can be liberated using hydrogen fuel cells or via combustion with oxygen to produce pure water.¹⁵ In comparison to an electrolyzer powered by a photovoltaic panel, devices for artificial photosynthesis have the potential to lead to lower systems costs if they reduce the total number of components required for the balance of systems without substantive reductions in device efficiency or stability.¹⁶ Integrated devices that simultaneously capture solar energy and use it to drive electrochemical reactions will be referred to as solar fuels devices throughout this manuscript.¹⁷

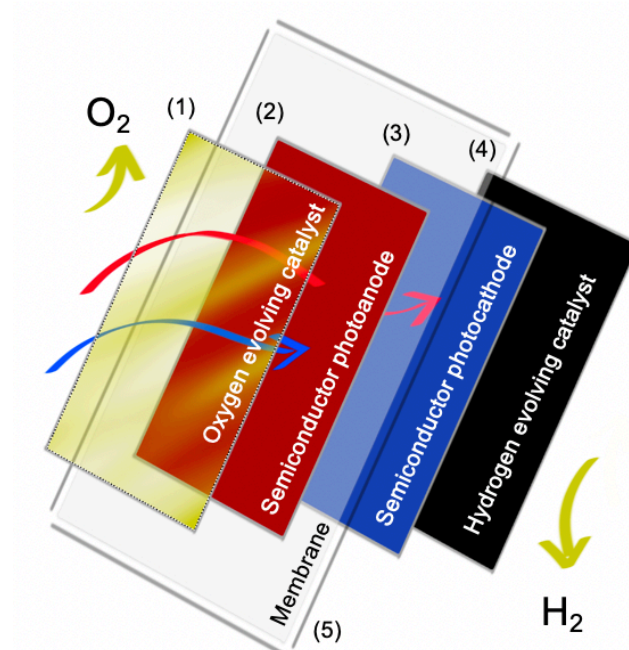
1.2 Materials for Producing Solar Fuels

Over the last 10 years, a global research effort been made towards bringing solar fuels devices from research-scale demonstrations to a commercially viable technology.¹⁸ To be considered for implementation within an energy system, devices must be safe, stable, and scalable.¹⁹ A general sketch of the components required for a practical solar fuels device meeting these requirements is provided as **Scheme 1.1**. Two catalyst layers serve to lower the energetic barriers for charge transfer when converting protons and/or hydroxide ions to oxygen and hydrogen. Two semiconductors, a photoanode and a photocathode, produce a voltage sufficient to drive the water-splitting reaction when combined in series.

Strongly acidic (pH \sim 0) or strongly basic (pH \sim 14) electrolytes are required during water-splitting to prevent the accumulation of concentration gradients within the cell, which impose stringent stability requirements on catalysts and light absorbers.²⁰ Membranes are necessary to separate explosive fuels from coevolved oxygen gas. Early reports of unassisted solar-driven water splitting under concentrated sunlight demonstrated stable operation for 20 hours.²¹ A more recent report of fully-integrated solar fuels device using Si light absorbers and rare-earth metal catalysts demonstrated 33 days of intermittent day/night cycling in 1 M H₂SO₄(aq).²² A two-order-of-magnitude increase in stability is needed in order for device lifetimes to be comparable to commercial photovoltaic modules.

Materials discovery efforts have yielded a number of light-absorbers and catalysts capable of sustained operation in strongly acidic and/or strongly basic electrolytes,²³⁻²⁴ facilitated by the development of transparent conducting oxides for use as protection layers for semiconductors that form passivating oxides.²⁵ Earth-abundant, acid-stable catalysts for the hydrogen-evolution reaction could serve as alternatives to rare earth metals such as Pt,^{24, 26} but significantly greater mass loadings are required for these catalysts to operate at acceptable overpotentials. Much of this dissertation involves cobalt phosphide, CoP, which is among the fastest catalysts that could serve as a Pt replacement. Careful investigations of metal dissolution rates under potential control suggest earth-abundant catalysts including CoP, are likely to corrode during dark, open-circuit conditions.²⁷ Increased catalyst loadings and/or new strategies for protecting catalysts against dissolution must be demonstrated in order for these materials to be considered as alternatives to thermodynamically stable Pt.²⁸ Si has been used as a model light-absorbing semiconductor throughout. Si is stable in acidic solutions and can be protected from dissolution in basic

solutions via thin layers of metal oxides.²⁵ Si can be readily cleaned and processed to form photoactive, charge-separating junctions, making it well suited for the study of electrocatalyst integration. Silicon microwires are a potentially scalable alternative to crystalline Si wafers and can be grown directly from SiCl_4 gas using copper catalysts as “seeds”.²⁹

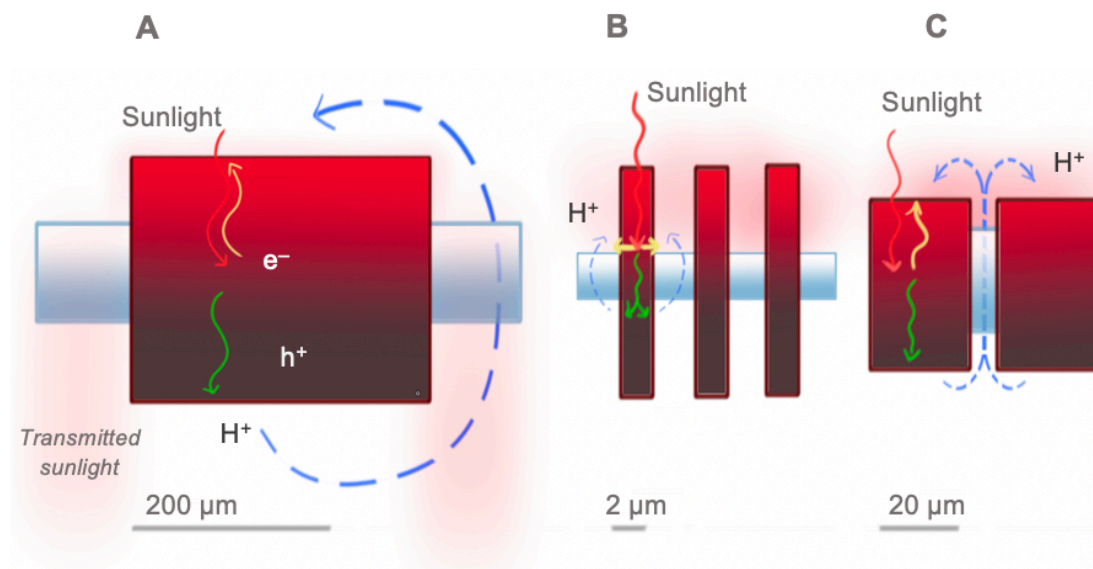


Scheme 1.1: Layered representation of the components required for a solar fuels device. In this orientation, light passes through the (1) oxygen evolution catalyst, with the blue half of the solar spectrum absorbed by a (2) semiconducting photoanode and the remaining, red photons absorbed by a (3) semiconducting photocathode. (4) A hydrogen-evolving catalyst on the bottom side of the device produces fuel for energy storage. (5) A membrane allows ions to transfer from reactions occurring at (1) and (4) while keeping the combustible products separate.

1.3 Integration of Semiconductors and Electrocatalysts

1.3.1 Thesis statement

Designing a solar fuels device that is safe, stable, and scalable requires engineers to navigate trade-offs in performance of individual components. Macroscale integration of components often leads to devices that perform equal to or worse than the sum of their parts, whereas micro- and nanoscale integration strategies can lead to complementary effects. Consider the example of a water-splitting solar fuels device in which a membrane must be incorporated to allow the transfer of ions between the anode and cathode while keeping combustible hydrogen and oxygen gases separate (**Scheme 1.2**). A macroscopic light absorber surrounded by an ion conducting membrane will absorb less light than a continuous solar panel while increasing the ohmic drop in comparison to catalysts integrated adjacent to a membrane (**Scheme 1.2A**). However, *micro- or nanoscale* light absorbing elements embedded within a polymer membrane could exhibit an absorptivity equivalent to a continuous panel while simultaneously reducing the distances required for charge carrier collection and without increasing the distance required for ion transfer (**Scheme 1.2B**).³⁰⁻³¹ Comparable results might be possible at microscale, ion-conducting channels within a monolithic solar fuels device, when illuminated at non-normal incidence or using light-scattering elements within the channel (**Scheme 1.2C**).



Scheme 1.2: Representative solar fuels device designs. **(A)** Macroscale integration of a light absorber (red) surrounded by an ion-conducting membrane (blue). The optical penetration depth and the minority carrier collection length are mutually similar. The maximum distance traveled by protons (H^+) via diffusion is set by the thickness and width of the absorber. The projected area of the light absorber is directly proportional to the quantity of light absorbed. **(B)** Microscale integration of light absorbers within an ion conducting membrane. The minority carrier collection length is much smaller than the optical penetration depth. The maximum distance traveled by ions is set by the length of the absorbing elements. The projected area of the light absorber is not necessarily proportional to the quantity of light absorbed. **(C)** Alternate microscale integration of a membrane within a light absorber.

In this dissertation stems I will address the knowledge gap associated with the design considerations discussed above: *How and why do three-dimensional structures of light-absorbing semiconductors and electrocatalysts allow solar fuels devices to avoid trade-offs during integration?* In particular, high-aspect ratio structures—where the ratio between two length scales defining a feature exceeds 10:1—were found to afford considerable opportunities for improving device performance. High-aspect ratio Si

microwire and microcone arrays allowed for increased loadings of electrocatalysts to be used without substantial absorption or reflection of incident sunlight. Nanostructured metal-phosphide catalyst layers decoupled optical losses from the fractional coverage of the light absorber surface. Downward-facing microwire arrays produced thin films of gas bubbles at high coverages, leading to efficient collection of gaseous products without substantial voltage losses due to catalyst obstruction and ohmic resistance. Planar and microwire-array photoanodes produced gas bubble films that led to minimal optical losses on the sunlight-facing side of a solar fuels device and generated sufficient convection for passive device operation without external convection.

1.3.2 Light-management at high-aspect ratio Si

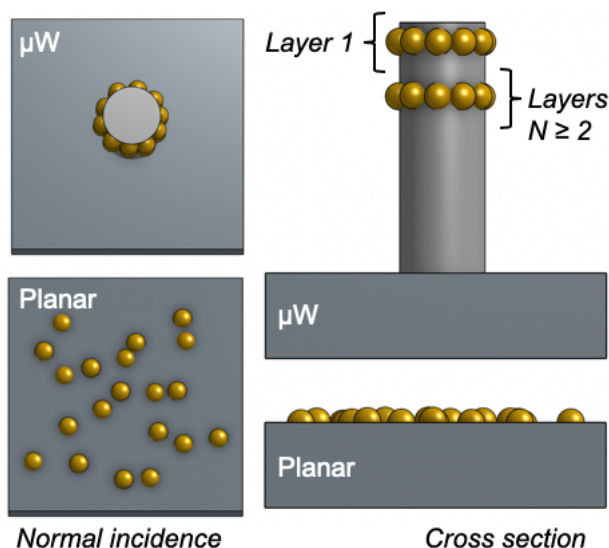
Fully integrated solar fuels devices require that either the oxygen-evolving catalyst and/or the fuel-forming catalyst be placed in the path of incident sunlight.¹⁹ Optical losses due to reflection and parasitic absorption occur when metallic electrocatalysts are placed on the light-facing side of a solar fuels device.^{14, 32} Increasing the density of the catalyst on the surface increases the efficiency of fuel formation by reducing the additional voltage required to drive charge transfer at the electrolyte interface.^{24, 32-33} Conversely, increasing the loading of catalyst on the surface also attenuates the light reaching the semiconductor. The optimal catalyst loading maximizes the charge transfer kinetics while reflecting and absorbing a minimum amount of photons.³⁴ Multi-electron reduction reactions generating products such as methane and ethylene require greater mass loadings of catalyst, which makes such optimization challenging at a planar semiconductor surface. Light management is less challenging for metal oxide catalysts and protection layers

prepared from wide-band gap semiconductors such as nickel-oxide, which exhibit minimal absorptivity towards photons in the visible range of the electromagnetic spectrum.³⁵⁻³⁶

Microstructured photoelectrodes have several advantages in integrated systems for solar fuel production relative to planar electrodes. High-aspect ratio microwires allow for collection of light along the long microwire axis and collection of photogenerated carriers along the narrow microwire radius, which could optimize carrier collection in impure, inexpensive semiconductors grown by scalable methods.³⁷⁻³⁸ Furthermore, the increased area of the semiconductor/electrolyte interface affords an opportunity to support high loadings of electrocatalysts without deleterious absorption of incident photons.³⁹ When the light absorber and electrocatalyst are both on the sunlight-facing surface, strategic placement of the catalyst out of the path has been shown to reduce optical losses due to parasitic light-absorption.⁴⁰

Chapter 2 reports the use of Si photocathodes for sunlight-driven hydrogen evolution using electrodeposited cobalt phosphide, CoP, as a catalyst. CoP is among the most active earth-abundant catalysts for the hydrogen evolution reaction in acid but strongly absorbs and reflects incident sunlight. Integration of a few nm of CoP on planar Si had previously been shown to contribute to a 30% reduction in the photocurrent relative to a polished Si surface.⁴¹ We prepared p-Si microwire-array photocathodes decorated with CoP through a low-temperature and rapid electrodeposition process that led to the selective placement of catalyst along the microwire sidewalls.⁴² At normal incidence, this integration strategy decoupled the projected area of the electrocatalyst from the electrochemically active surface area (**Scheme 1.3**); equivalent loadings, as measured by the charge passed

during electrodeposition, led to 22% reductions in the photocurrent at a p-Si microwire-array electrode whereas the photocurrent at a planar p-Si surface was reduced by 49%.



Scheme 1.3: Identical catalyst loadings on microstructured and planar semiconductors showing the different effects of light blocking at normal incidence. Relative to a planar surface, the shaded area produced by a single hemisphere located on a vertical microwire sidewall is reduced by approximately a factor of two (Layer 1) and additional layers of catalyst particles (Layers $N \geq 2$) do not contribute significantly to shaded areas on the semiconductor.

Chapter 3 extends the strategy of depositing electrocatalysts on vertical sidewalls to the (photo)electrochemical reduction of CO_2 to hydrocarbons. The charge transfer kinetics of CO_2 reduction to methane and ethylene at copper surfaces are many orders of magnitude slower than proton reduction to hydrogen at Pt. Light management at high surface area Cu films used for electrochemical CO_2 reduction has been a bottleneck for the preparation of photocathodes capable of generating hydrocarbon fuels. Photocathodes prepared from nanoparticulate Cu at polished p-Si surfaces exhibited absolute photocurrent

densities $> 20 \text{ mA cm}^{-2}$ but the onset of the production of hydrocarbons was shifted $+0.3 \text{ V}$ —less than the photovoltage provided by the Si. CuAg films on the backside of a Si light absorber—out of the path of incident sunlight—yielded absolute photocurrent densities $> 32 \text{ mA cm}^{-2}$. We deposited high mass loadings of Cu electrocatalyst onto p-Si microwire-arrays doped with a radial-junction n^+ emitter layers leading to efficient photocathodes for the production of CH_4 and C_2H_4 from CO_2 under simulated sunlight. Although the increased junction area at a radially doped n^+ p-Si microwire-array photocathode is expected to lead to a reduced photovoltage in comparison to a planar n^+ p-Si photocathode, a simplified device physics model showed that this reduced photovoltage could be fully offset by increased rates of electrocatalysis for reactions requiring the use of sluggish electrocatalysts.

Chapter 4 investigates the use of an alternate microstructuring strategy: Si microcone, μ -cone, arrays.⁴³ Optical simulation of Si μ W arrays had previously revealed that the planar, top surface of the cylindrical μ Ws contributed significantly to reflections of incident sunlight. Microcones prepared via deep reactive-ion etching with positive tapering exhibited tip radii $\sim 25 \text{ nm}$, and led to surfaces that exhibited 99.5% of the light-trapping limit for wavelengths of light 400–1100 nm. To preserve the optimal light-absorption properties of the Si μ -cone arrays while integrating highly reflective electrocatalysts, we used a templated deposition of Ti/Pt thin films that selectively placed catalyst at the tips of individual μ -cones.⁴⁴ Reflections at the Pt/electrolyte interface were directed towards the internal volume of the μ -cone array such that the otherwise highly reflective catalyst layer did not contribute to reductions in photocurrent relative to a bare μ -cone array. This strategy of leveraging guided reflections from the metal surface is

similar to that used for the preparation effectively transparent contacts (ETCs) for photovoltaics.⁴⁵

1.3.3 *Light-management at high-aspect ratio CoP*

Noble metal catalysts for the hydrogen-evolution reaction in acidic electrolytes lead to efficient devices based on p-type Si and InP photocathodes, because the films can be structured as small islands that are effectively transparent.⁴⁶ In acid, Pt catalyzes the hydrogen evolution reaction at rates that are Nernstian in character—the rate is controlled by mass-transport and not by charge transfer kinetics.⁴⁷ More recently, a transparent Rh film enabled the highest reported solar-to-hydrogen conversion efficiency at a photocathode under 1-Sun.⁴⁸ Integration of earth-abundant catalysts is made more challenging by the higher-mass loadings and decreased stability of such films in corrosive environments.²⁷ Semiconducting transition-metal selenides and transition-metal sulfides, which require absolute overpotentials of 150–183 mV to drive the HER at a current density (J) of -10 mA cm^{-2} , have been integrated with textured, antireflective silicon photocathodes as uniform, amorphous films, approximately 50 nm in thickness.⁴⁹ Such devices have exhibited high photocurrent densities ($|J| > 30 \text{ mA cm}^{-2}$) for 2 h in 0.50 M $\text{H}_2\text{SO}_4(\text{aq})$.⁵⁰⁻⁵² Substantially longer stabilities under reductive bias, and thus increased catalyst loadings or more stable catalyst materials, are required for a practical solar fuels device.

In Chapter 5, we extend the preparation of effectively transparent films, previously demonstrated at noble metals, to transition metal phosphides. Prior integration efforts focused on the three-dimensional structure of the light-absorbing semiconductor to assist in light management; this work showed that the structural control of the electrocatalyst could also allow the catalyst area and optical losses to be decoupled. Continuous films of

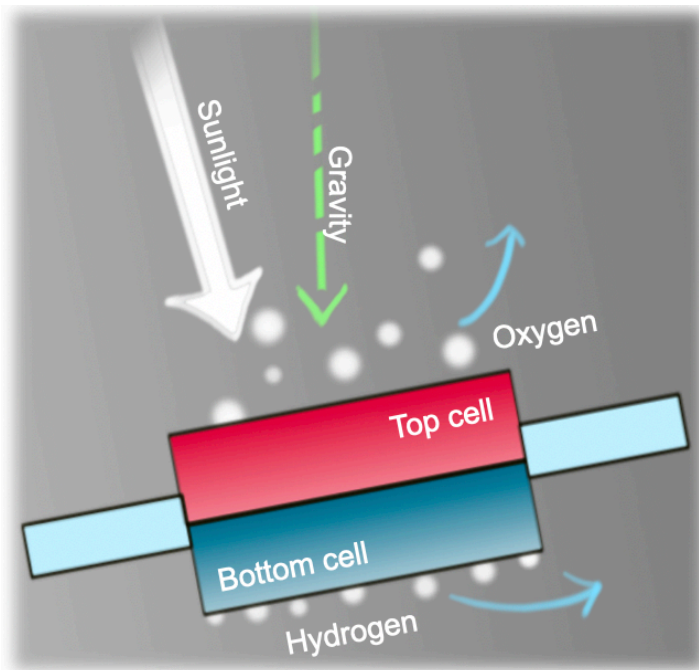
CoP were electrodeposited onto planar n⁺p-Si that had been pre-nucleated for deposition with a thin layer of Co on top of a Ti adhesion layer. Although deposition of this catalyst film led to a > 70% reduction in the photocurrent, operation of the device in 0.50 M H₂SO₄ led to a spontaneous reorganization of the films nanostructure that was accompanied by a > 250% *increase* in the photocurrent. Physical characterization of thin CoP films on polished Si surfaces before and after exposure to H₂SO₄ indicated that the changes to the optical properties of the film were accompanied by the formation of oriented cracks that extended from the substrate to the surface of the film. The optical properties of the film were measured and modeled using spectroscopic ellipsometry, which revealed that the increased transmissivity was due to the film behaving as an effective medium, wherein electromagnetic radiation was forced into the narrow cracks such that the reflection of light was no longer proportional to the fraction of the surface covered by catalyst. Such a strategy for light management is significant in that it does not depend strongly on the optical properties of the metal, and thus can be extended to a variety of other earth abundant catalysts, and could be complementary with other strategies for light-management such as selective placement onto μ W sidewalls.^{42, 53-54} or patterning as catalyst islands.^{32, 55}

1.3.4 Control of H₂ and O₂ bubbles at electrode surfaces

A common feature of water-splitting solar fuels systems is the production of bubbles of H₂ or O₂ on both the light, upward-facing and the dark, downwards-facing sides of the device, once the activity of H₂(aq) or O₂(aq) is sufficient to surpass the free-energy barrier to nucleation.⁴⁻⁶ Bubbles can deleteriously refract light away from the light absorber;⁷ preclude effective contact between the liquid electrolyte and the electrocatalyst;⁸⁻⁹ and affect mass transport of species in the boundary layer as well as in

the internal volume of porous, structured electrodes. In small-scale laboratory demonstration systems, effects of bubbles are often minimized by vigorously stirring the solution and/or by testing the electrodes in a side-facing or upwards-facing geometry.¹ In most device configurations that are contemplated for use in the field, active stirring of the electrolyte over large areas is not practical.³ Management of gas coverage is essential at industrial-scale electrodes, such as downward-facing, CO₂(g)-evolving anodes required for aluminum manufacturing, in which the thickness of bubble fronts moving across the surface can exceed 1 cm.¹⁰

We were motivated to understand the effects of bubbles on solar fuels devices, particularly on devices of a practical size and orientation. Our research efforts considered gas evolution at the illuminated, upward-facing top cell and at the dark, downward-facing bottom cell (**Scheme 1.4**). Our assumption was that most designs would choose to evolve oxygen on the sunlight facing side of the device, such that gas could be vented out into the atmosphere, and hydrogen on the bottom side of the device where it would be collected and stored. Ideally, a solar fuels device could operate passively, with bubbles rising via natural buoyancy, obviating the need for external pumps to stir the electrolyte.



Scheme 1.4: Fully integrated, tandem solar fuels device where the absorber is oriented towards the sun. Such orientation leads to misalignment with the gravitational vector at latitudes off the equator. In the cell represented here, oxygen is evolved from the sunlight facing photoanode whereas hydrogen is evolved from the downward facing photocathode.

In Chapter 6, we considered the effects of hydrogen gas evolution on cathodes oriented against gravity. This allowed us to focus on the electrochemical effects of gas evolution without light as a confounding variable. High-speed videos recorded during testing characterized how the coverage and thickness of the gas layer at a downward-facing electrode impacted the electrochemical performance. The key finding was that capillary forces within Si μ W arrays provided a mechanism for gas bubble removal from a downward-facing electrode surface. Whereas planar surfaces accumulated large, cm-scale gas bubbles that contributed to a significant increase in ohmic resistance, microwire arrays rapidly released small bubbles. Sparsely packed microwire arrays exhibited high gas coverages that led to minimal increases in the ohmic drop and kinetic overpotential but

reduced the concentration overpotential and increased mass-transport in comparison to a bubble-free electrolyte.

The effects of gas bubble evolution on an upward-facing top cell are discussed in Chapter 7. Although crystalline Si would likely serve as the bottom-cell in an integrated device, TiO₂-protected Si photoanodes enabled careful tuning of the electrode microstructure such that its effect on gas bubbles emanating from an upward facing photoanode could be characterized. Very low gas coverages were observed at oxygen-evolving top cells, in stark contrast to coverages previously observed at hydrogen-evolving bottom cells. Ray tracing simulations predicted that higher gas coverages could be tolerated without leading to significant increases in the fraction of light lost, consistent with measurements at photoelectrodes evolving hydrogen and oxygen. Calculated mass-transport velocities indicated that the microconvection generated by the departure of gas bubbles from the surface was sufficient to eliminate the need for external pumping and stirring in solar fuels devices. Microwire surfaces led to smaller and more numerous gas bubbles in comparison to planar surfaces, which could improve the uniformity of bubble-generated microconvection.

1.3.5 Summary and Outlook

In the following chapters, I will share a number of strategies for controlling the three-dimensional structure of semiconductors, electrocatalysts, and the film of gas bubbles evolved on the top and bottom of a solar fuels device. Three-dimensional structures that incorporate high-aspect ratio features can lead to unexpected effects, such as transparent metal films (Chapter 5). New challenges arise when designing microstructured architectures for solar fuels devices, e.g. increased charge-separating junction areas can

lead to unacceptable reductions in photovoltage and may require improved passivation to be viable (Chapter 4). Kinetically-limited, multielectron reductions, such as the reduction of CO₂ to methane and ethylene, require increased mass-loadings of electrocatalysts and thus offset reductions in photovoltage with a greater reduction in overpotential (Chapter 3). Microstructured surfaces can force bubbles away from the surface, even when oriented against gravity, leading to sustained operation in the absence of external convection (Chapters 6 and 7). Although previous advances to the efficiency of solar fuels devices have involved planar, macroscale integration strategies, major breakthroughs in the cost and stability of such systems are required for Artificial Photosynthesis to be deployed. Such breakthroughs may require rethinking the rules of device integration via microstructural design, thus enabling a transition to a cleaner and more sustainable future.

Chapter 2

HYDROGEN EVOLUTION WITH MINIMAL PARASITIC LIGHT ABSORPTION BY DENSE CO-P CATALYST FILMS ON STRUCTURED P-SI PHOTOCATHODES

Kempler, P. A., Gonzalez, M. A., Papadantonakis, K. M., & Lewis, N. S. (2018).

Hydrogen evolution with minimal parasitic light absorption by dense Co–P catalyst films on structured p-Si photocathodes. *ACS Energy Letters*, 3(3), 612-617.

<https://doi.org/10.1021/acseenergylett.8b00034>

2.1 Introduction

Low filling fractions of catalyst islands on planar photocathodes minimize optical losses but yield increases in overpotential due to the concentration of current density at the catalyst-coated regions of the electrode.³² Moreover, the approach either requires an emitter layer for efficient carrier transport to the catalyst-coated regions, or requires that the islands are separated by less than the minority-carrier collection length and optimally operate in the pinch-off regime to avoid excess majority-carrier recombination.⁵⁶ Microstructured electrode morphologies also have been used, and films of opaque catalyst nanoparticles (NPs) can yield minimal photocurrent losses when deposited strategically on emitter-containing p-Si microwire arrays.⁵⁷⁻⁶⁰ Specifically, high-lifetime n⁺p-Si microwire-array (μ W) cathodes with CoP NPs loaded at the base of the μ Ws yield an ideal regenerative cell efficiency (η_{IRC}) of 1.9% under 1 Sun illumination, but these devices

exhibit low fill factors.⁵⁹ Designs using n⁺p Si μ W-array cathodes with NiMo loaded at the base of the μ Ws, beneath a layer of TiO₂ NPs, or directed to the tips by an insulating, antireflective SiO₂ layer, yielded $\eta_{\text{IRC}} = 2.9\%$ and 10.8% respectively.^{58, 60} These systems require a radial emitter to facilitate carrier transport axially from the site of photogeneration to the location of the catalyst. We demonstrate herein that three-dimensionally structured semiconductors allow dense films of Co-P to be integrated with photocathodes in designs that place the opaque catalysts in the path of incident sunlight, but produce minimal parasitic absorption because the catalysts are primarily placed on surfaces that are orthogonal to the incident rays. This strategy is beneficial in the presence or absence of an emitter layer, and thus is a promising design for efficient photoelectrodes for solar fuel production.

2.2 Experimental Methods

Randomly textured micropyramidal, μ P, Si structures were formed via anisotropic etching of an unpatterned P-type Si <100> wafer with resistivity 10-20 Ω -cm that was first cleaned in 3:1 H₂SO₄ to 30% wt H₂O₂ for 10 min. The wafer was then etched for 1 h at 80 °C in an aqueous solution of 2% wt potassium hydroxide/20% v isopropyl alcohol. Silicon microwire arrays 30 μ m in height and 3 μ m in diameter were formed via deep reactive-ion etching in an SF₆/O₂ plasma, with a photolithographically patterned alumina mask used to define the microwire dimensions. **(A.1)** All Si samples were cleaned in a RCA SC1 bath (5:1:1 H₂O/NH₄OH/H₂O₂, 80 °C for >10 min), buffered oxide etch (at room temperature for 5 min), and a RCA SC2 bath (6:1:1 H₂O/HCl/H₂O₂, 70°C for >10 min) to remove SiO₂, Al₂O₃ and trace metal impurities. An n⁺p junction was formed via diffusion doping with CeP₂O₁₄ doping wafers **(A.1)**. Si samples were coated with a Co-P catalyst via low-

temperature, scalable photoelectrochemical deposition.²⁶ The cathodic charge density passed during deposition, normalized to the projected area of the individual electrode, was used to determine the catalyst loading. Immediately after deposition of the catalyst, electrodes were tested for hydrogen evolution in a cell filled with 0.50 M H₂SO₄(aq) (TraceMetals grade, Fisher) that was continuously purged with 1 atm of H₂(g) and illuminated with 100 mW cm⁻² of simulated AM1.5 sunlight. The acidic testing environment leached excess Co from the films, reduced the absolute overpotential for hydrogen evolution until a stable value was reached within 30 min, and left islands of Co-P with an elemental Co/P ratio of ~2:1 on the substrates. The ~2:1 Co/P ratio obtained after the catalyst-activation step is in close agreement with values measured for electrochemically deposited Co-P.^{26, 61}

2.3 Results

Figure 2.1 shows scanning-electron micrographs (SEMs) of each of the p-Si/Co-P cathode structures examined in this work: planar p-Si, as well as p-Si microwires (μ W) or p-Si micropyramids (μ P on a planar, photoactive substrate). After etching, the height of the vertical Si microwires was 30 μ m and the heights of the $\langle 111 \rangle$ Si micropyramids were ≤ 3 μ m. Photoelectrodeposition of Co-P resulted in discontinuous islands of Co-P distributed over the planar or microstructured p-Si surface. The vertical sidewalls of the μ Ws comprised the majority of the geometric surface area for the p-Si μ W-on-planar substrate. Electrodeposition directed the opaque catalyst preferentially to the surface of the μ Ws and away from the planar portion of the substrates, which remained mostly bare. Notably, deposition at high, mass-transport limited, current densities directed the catalyst deposits towards the tips of the microwires (**Figure 2.1D**). Electrodeposition of Co-P onto

n^+ -Si μ W substrates in the dark produced a similar distribution of catalyst along the length of the μ W as was observed for p-Si μ W substrates. Top-down comparisons of microwires and planar substrates with equal amounts of charge passed for Co-P electrodeposition showed that a substantially larger portion of the light-absorbing face of the semiconductor remained exposed than for deposition on planar Si electrodes (**Fig 2.1A,C**).

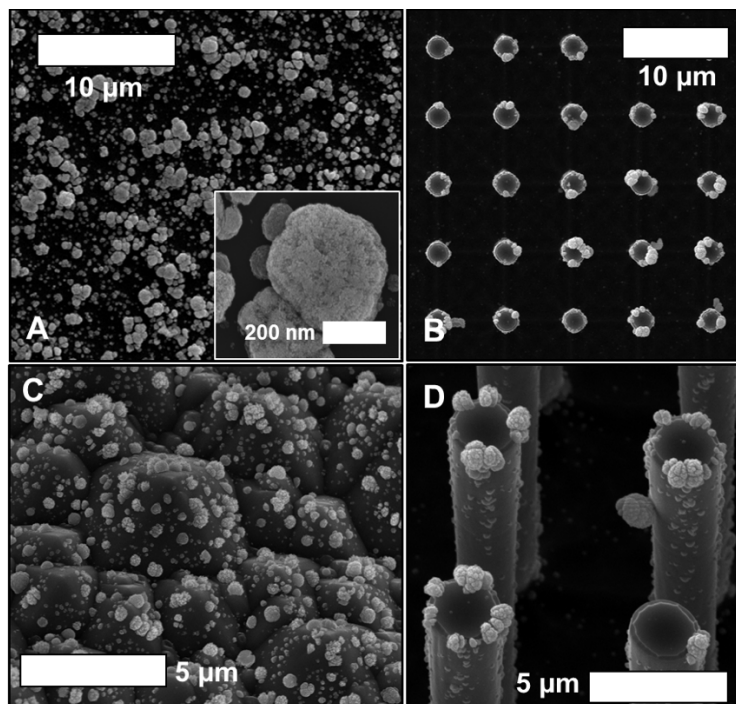


Figure 2.1: Scanning-electron micrographs of photoelectrochemically deposited Co-P particles after 400 mC cm^{-2} charge was passed. **(A)** Top-down image of planar p-Si, inset: magnified image of individual particle showing nanoscale roughness; **(B)** Top-down image of p-Si microwire array showing minimal deposition along the base and caps of the wires; **(C)** Image at 30-degrees tilt of p-Si micropyramid array; **(D)** Image at 20-degrees tilt of p-Si microwire array.

Figure 2.2 compares the current density vs potential (J - E) behavior for representative planar p-Si, μ P p-Si, and μ W p-Si/Co-P cathodes for a 400 mC cm^{-2} loading of electrodeposited and activated Co-P HER catalyst. Planar p-Si loaded with 400 mC cm^{-2}

² of Co-P exhibited substantial parasitic absorption as well as low fill factors, and these devices yielded short-circuit (i.e. at 0 V vs RHE) current densities of $-13.6 \pm 0.6 \text{ mA cm}^{-2}$ and cathodic current densities $> 10 \text{ mA cm}^{-2}$ at an average potential of $74 \pm 10 \text{ mV}$ vs RHE. Structured p-Si/Co-P devices exhibited a larger cathodic current density at all potentials relative to planar devices, or equivalently, a more positive potential vs RHE at all operational current densities. For example, μP p-Si/Co-P and μW p-Si/Co-P devices exhibited cathodic current densities $> 10 \text{ mA cm}^{-2}$ at potentials of $181 \pm 19 \text{ mV}$ and $211 \pm 11 \text{ mV}$, respectively, vs RHE.

Table 2.1: Average figures of merit for different p-Si structures loaded with Co-P and tested at 100 mW cm^{-2} of simulated sunlight in $0.50 \text{ M H}_2\text{SO}_4(\text{aq})$. The short-circuit current density, J_{sc} is the current density at the equilibrium potential for hydrogen evolution, RHE. The limiting current density, J_{lim} , was recorded at -0.3 V vs RHE and is proportional to the total number of photons collected by the underlying Si. These values are compared to the limiting current density recorded for the bare Si devices. The potential at -10 mA cm^{-2} and 0 mA cm^{-2} , as well as V_{oc} , determined by the difference between the open-circuit potential and RHE, are also reported. Data points were recorded during scans at 50 mV s^{-1} after the device performance had stabilized.

Cathode structure	$ J_{\max} $ (mA cm^{-2})	Co-P loading = 400 mC cm^{-2}			
		$ J_{sc} $ (mA cm^{-2})	V_{oc} (V vs RHE)	V_{10} (V vs RHE)	J_{sc}/J_{\max}
p-Si/Co-P planar	27 ± 0.5	13 ± 1	0.265 ± 0.026	0.074 ± 0.010	0.51 ± 0.02
p-Si/Co-P μP	31 ± 2	18 ± 1	0.286 ± 0.011	0.181 ± 0.019	0.58 ± 0.05
p-Si/Co-P μW	28 ± 1	22 ± 2	0.342 ± 0.024	0.211 ± 0.012	0.78 ± 0.05

The difference in V_{oc} between μ W and μ P p-Si/Co-P compared to planar p-Si/Co-P electrodes cannot be explained solely by the decrease in light-limited photocurrent densities, and hence must be due to some interfacial phenomena, including possibly oxide formation or other interfacial kinetic processes differentially affecting the anodic and cathodic current densities that determine the potential of net zero current for the electrode/electrolyte system of interest. A comparison of these figures-of-merit is provided as **Table 2.1**. Prior to deposition of the catalyst, the photocathode structures exhibited similar limiting current densities while in contact with 0.50 M $H_2SO_4(aq)$ and under 100 $mW\ cm^{-2}$ of simulated AM1.5 illumination. The limiting current density was $26.7 \pm 0.5\ mA\ cm^{-2}$ for planar p-Si, $31 \pm 2\ mA\ cm^{-2}$ for p-Si μ P, and $28 \pm 1\ mA\ cm^{-2}$ for bare p-Si μ W devices. These values represent the maximum photocurrent densities, $|J_{max}|$, obtainable for each device type before losses due to parasitic absorption by the catalyst are introduced. The measured $|J_{max}|$ was consistent with the theoretical maximum photocurrent density simulated for a planar Si slab, after correcting for losses due to reflection at the Si/0.50 M $H_2SO_4(aq)$ interface and absorption in the $\sim 1\ cm$ of electrolyte between the cell window and the surface of the sample.⁶²⁻⁶³

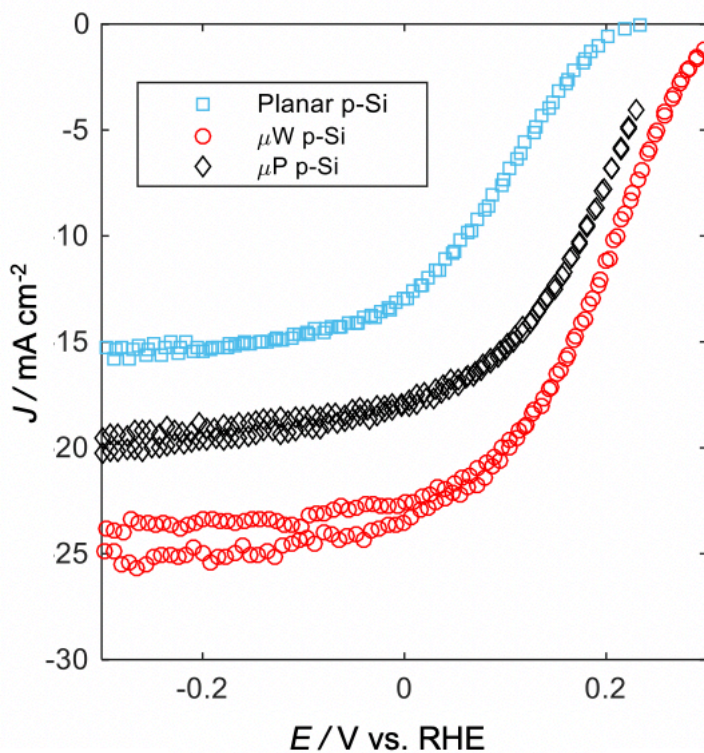


Figure 2.2: J - E behavior of p-Si photocathodes with 400 mC cm^{-2} of Co-P catalyst in $0.50 \text{ M H}_2\text{SO}_4(\text{aq})$ under simulated 1 Sun illumination. Scans were recorded at 50 mV s^{-1} at potentials negative of the open-circuit potential, to avoid oxidation of the Si/catalyst interface.

For each structure, $|J_{sc}|$ was lower than $|J_{max}|$ for the respective bare p-Si structured electrode, indicating that in all cases addition of the Co-P catalyst introduced some parasitic optical absorption. However, equivalent catalyst loadings impeded light absorption differently depending on the structure of the Si substrate. The 400 mC cm^{-2} loading of Co-P blocked more light for the planar p-Si/Co-P and μP p-Si/Co-P devices, which yielded J_{sc} / J_{max} values of 0.51 and 0.58, respectively, than for the μW p-Si/Co-P devices, which yielded $J_{sc} / J_{max} = 0.78$ (**Table 2.1**). Thus, the Si μW structure reduced parasitic optical absorption due to deposited Co-P deposition by a factor of 2 relative to the planar surface.

Figure 2.3 illustrates the effect of electrode structuring on obscuration by opaque films, by displaying the photocurrent obtained from each of the device structures during photoelectrodeposition of the opaque Co-P catalyst-precursor film, i.e. prior to the activation step that removed excess Co and structured the film as islands, leaving exposed areas on the substrate. The planar and μP p-Si devices both exhibited a rapid rate of decrease in photocurrent as the loading of the opaque film was increased, whereas the p-Si μW photocathode showed a much lower rate of decrease in photocurrent with increased loading of the opaque film than the other types of Si photocathodes. The decrease in $|J_{sc}|$ after catalyst deposition for planar and μP Si devices was due to masking of the light-absorbing surfaces by the catalyst film. For Si μW devices, the high-aspect ratio structure of the substrate provided a geometric surface area that was several times larger than the projected surface area, allowing the total mass of catalyst supported on the electrode to be increased without proportionately increasing shadowing of the planar surfaces of the structure. Most of the geometric surface area of the Si μW -on-planar devices is on the sidewalls of the Si μW s and oriented normal to the direction of illumination, so additional catalyst deposition did not substantially increase the parasitic optical absorption, and large catalyst loadings can be used without substantial losses of $|J_{sc}|$.

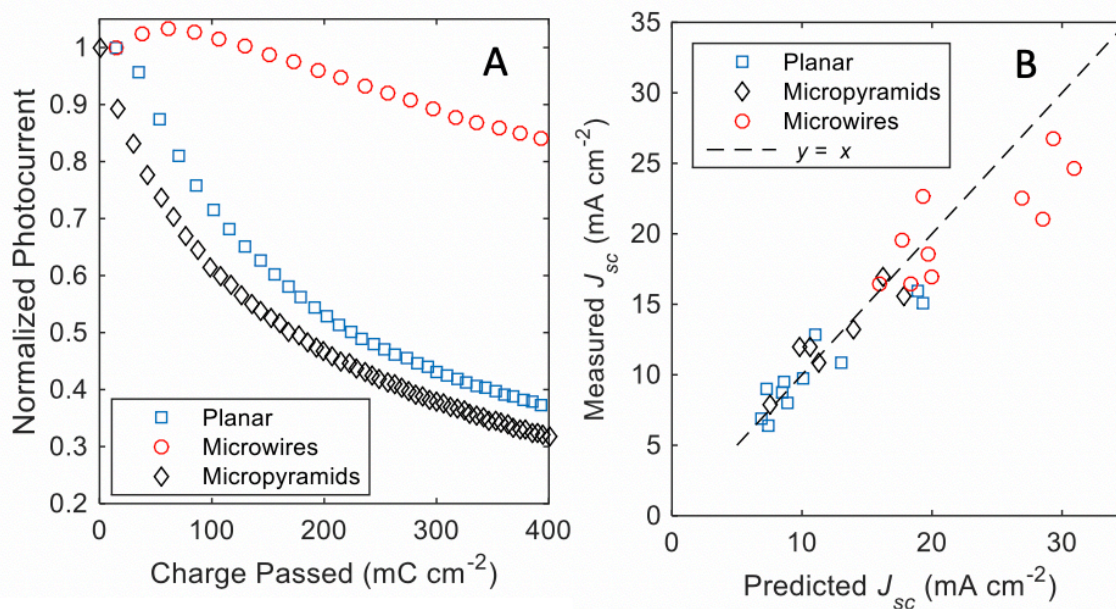


Figure 2.3: (A) Loss in photocurrent during deposition of Co-P on various p-Si structures, expressed as the light-limited current density vs. passed cathodic charge density. For clarity, the current density was normalized to the initial current density recorded for the bare photocathode in the deposition cell. (B) The measured photocurrent density in the deposition cell was highly correlated with J_{sc} for hydrogen evolution prior to dissolution of excess cobalt during activation. The predicted values of J_{sc} under 100 mW cm^{-2} of simulated solar illumination in $0.50 \text{ M H}_2\text{SO}_4(\text{aq})$ were calculated based on the ratio of the initial photocurrent and final photocurrent during deposition, multiplied by the limiting photocurrent measured for the bare photocathode in $0.50 \text{ M H}_2\text{SO}_4(\text{aq})$ under nominally identical illumination conditions

Activation of the catalyst-precursor films resulted in a catalyst structured as islands, allowing more light to reach the semiconducting substrate after activation of the catalyst than during electrodeposition. Upon activation, $|J_{lim}|$ remained stable for $> 30 \text{ h}$ of continuous operation. Higher photocurrents were thus obtained from devices with activated catalyst islands (Figure 2.2) than from devices with an equivalent loading of catalyst structured as a continuous film (Figure 2.3B). When catalysts with low Tafel

slopes are used, structuring opaque catalyst films as islands has been shown to lead to improved efficiencies in planar devices relative to structuring the catalyst as a continuous film,³² but the catalyst-island strategy for minimizing parasitic absorption is limited for most catalyst-deposition methods other than lithography, because increases to the surface area of the catalyst typically result in lateral growth of the islands and therefore increased shadowing of the semiconductor by the catalyst. The structuring of the Co-P films as islands improved the performance of these devices relative to devices having continuous films, but the strategic placement of the catalyst onto a three-dimensionally structured electrode is the predominant factor responsible for the improvement in performance of the μW Si devices relative to μP and planar Si cathodes observed herein. To assess the effect of the increased surface area available for catalyst loading provided by the Si μW structure, the dark catalytic behavior was compared for electrodeposited Co-P on planar $\text{n}^+\text{-Si}$ and μW $\text{n}^+\text{-Si}$ electrodes (**Figure 2.4A**). The overpotential required to reach -10 mA cm^{-2} was reduced to 170 mV from 190 mV for the $\text{n}^+\text{-Si}$ μW sample relative to a planar $\text{n}^+\text{-Si}$ substrate. **Figure 2.4B** presents a comparison of the photoelectrochemical behavior of planar p-Si and μW p-Si electrodes at increased loading, 800 mC cm^{-2} , of Co-P. When the illumination intensity was increased to 125 mW cm^{-2} on the planar p-Si sample, J_{lim} increased to a value comparable to that of the μW device, but the increase in J_{sc} did not proportionally reflect this change. Furthermore, the potential at which -10 mA cm^{-2} was produced increased slightly, but remained over 100 mV more negative, for the planar p-Si sample relative to that of the μW p-Si electrodes. This behavior demonstrates that the improved light absorption by the μW device is not sufficient to explain the increased photoelectrochemical performance of these devices relative to the planar controls.

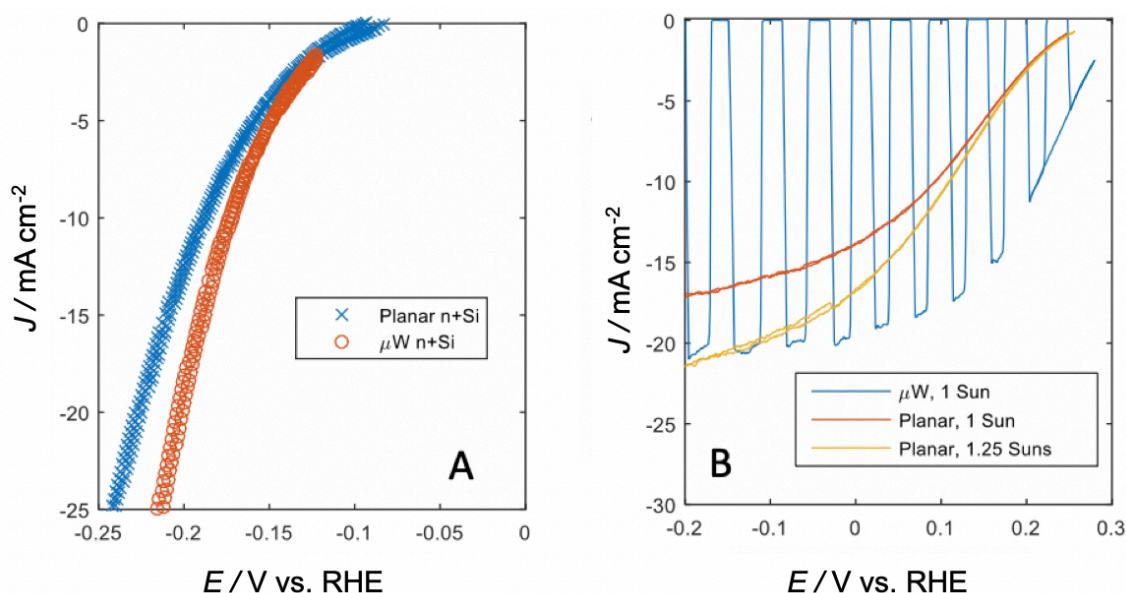


Figure 2.4: (A) Dark catalytic behavior of Co-P on planar n⁺-Si and on an n⁺-Si μ W array with 7 μ m pitch and 3 μ m diameter in 0.50 M H₂SO₄(aq). (B) Comparison at increased light intensity of the behavior of a high loading (800 mC cm⁻² of cathodic charge density passed) of Co-P on planar p-Si with the behavior of Co-P loaded p-Si microwires, demonstrating that the observed increases in performance for the p-Si μ W/Co-P array cannot be explained solely by an increase in the collection of photons.

The potential vs RHE required to reach an absolute current density of 10 mA cm⁻², E_{10} , is a figure of merit that relates the performance of a component half-cell measured using a three-electrode experiment, such as the photocathode described herein, to the performance that would be expected for a full cell with an operating current density of 10 mA cm⁻² and containing the component half-cell.⁶⁴⁻⁶⁵ The average E_{10} obtained for a p-Si μ W-array photocathode in this work, +211 mV versus RHE, is a substantial improvement relative to the +134 mV versus RHE reported for photoelectrochemically deposited Co-P on porous ‘black’ p-Si or +150 mV versus RHE for NiCoSe_x on nanopillar ‘black’ p-Si.⁵⁰

⁶⁶ With the inclusion of an emitter layer, the champion E_{10} for $\mu\text{W n}^+\text{p-Si/Co-P}$, +310 mV vs RHE (**Figure 2.5**), is slightly less positive than the $E_{10} = +345$ mV versus RHE value observed for crystalline, nanometer-thick films of CoP on planar $\text{n}^+\text{p-Si}$ cathode. The latter comparison is noteworthy because the $\text{n}^+\text{p-Si}$ μW -array photocathode exhibited a more rapid onset to -10 mA cm^{-2} relative to V_{oc} , indicating that the catalyst film was able to compensate for the decreased photovoltage relative to the planar film in the earlier study. When utilizing earth abundant catalysts with low Tafel slopes, the photovoltage lost from increased junction area can be offset by the lower overpotential that results from the increased area available for catalyst loading. The improved E_{10} for $\mu\text{W Si}$ relative to planar and μP counterparts, with and without a buried junction, is a direct demonstration of this design principle.

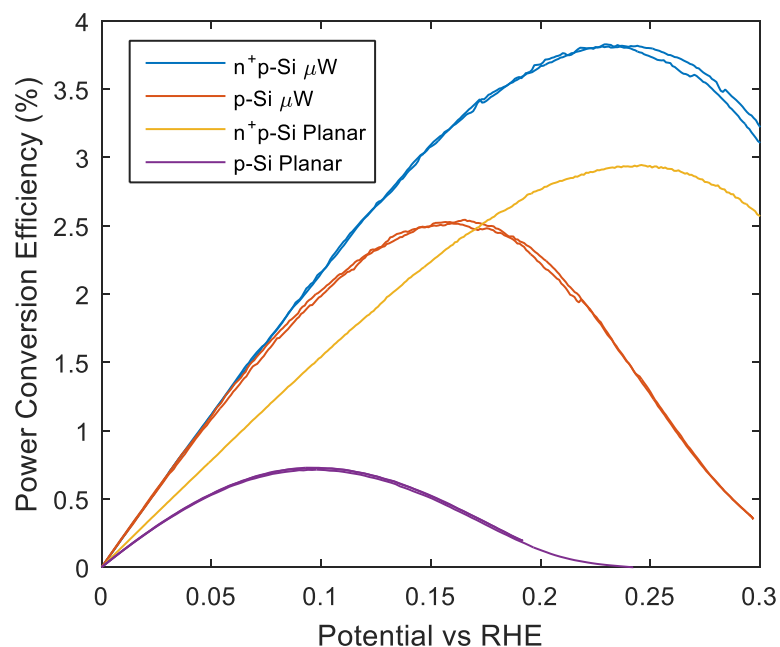


Figure 2.5: Power-conversion efficiencies for top-performing μW devices under 1 Sun illumination (100 mW cm^{-2}). The efficiency was calculated assuming 100% faradaic efficiency towards hydrogen evolution. $n^+p\text{-Si}$ devices outperformed $p\text{-Si}$ devices due to the increased voltage provided by the solid-state junction relative to the $p\text{-Si}/\text{liquid}$ junction. The maximum efficiency of $p\text{-Si}$ μW devices approached that of a planar $n^+p\text{-Si}$ device, due to the more efficient catalyst utilization on the surface of the microstructured photocathode.

2.4 Discussion

For Si photocathodes decorated with earth-abundant catalysts, the device efficiency can thus be increased substantially by minimizing the geometric footprint of the opaque catalyst over the light-absorbing surfaces of the semiconductor. Structured substrates allow for the catalyst footprint to be minimized without a reduction in the active surface area of the catalyst. The performance of the silicon microwire devices reported herein relied on long carrier-collection lengths in the axial direction. Free-standing microwire

arrays achieve optimal performance when minority carriers are collected radially, which requires that the catalyst loading be distributed along the length of the microwire to match the local carrier generation rate. The more general approach should be also useful for other semiconductor materials that can be structured such that the majority of the electrochemically active surface area is located on surfaces orthogonal to incident illumination,³⁷ provided that optical carrier generation is maximized and is spatially comparable to the photogenerated charge-carrier collection distances and catalyst location.⁶⁷⁻⁶⁸ Structuring Si into an array of microwires improved the peak power conversion efficiency by 250% while shifting the maximum power point positive by 65 mV (**Figure 2.5**). The photoactive planar substrate supporting the Si μ W-on-planar device described herein is not desirable for a completely membrane-embedded water-splitting device, hence study of catalyst placement onto Si μ W arrays that have been removed from the planar Si substrate and embedded in ion-exchange membranes, and testing of the membrane-embedded Si μ W arrays under a variety of device conditions, e.g. back-side illumination through the membrane, will be needed to evaluate these approaches in the context of specific device designs.³¹ Such studies may include selective deposition of the catalyst onto selected regions of structured semiconductors, e.g. the tips of the Si μ Ws, using wavelength-dependent photoelectrochemical deposition to further reduce parasitic absorption by the catalyst.⁶⁸ The bare Si μ W-arrays in this study were not optimized to minimize reflection, absorbing < 65% of incident photons. Silicon photocathodes textured to minimize reflection have achieved measured photocurrents near the absorption limit of silicon under AM1.5 illumination^{49-50, 66, 69}. Texturing High-aspect ratio structures with

antireflective surfaces could further improve the utilization of earth-abundant catalysts in photocathodes used for the HER.

2.5 Conclusion

P-type Si photocathodes incorporating high-aspect ratio microwire structures and supporting high mass loadings of an opaque earth-abundant catalyst showed substantially improved values of $|J_{sc}|$ relative to planar p-Si devices or p-Si devices textured with micropyramids. The vertical sidewalls of the microwires provided surfaces that supported high surface areas of the catalyst in an orientation that minimized the area of the semiconductor shadowed by the catalyst, thereby reducing parasitic optical absorption by the catalyst and improving $|J_{sc}|$ relative to the other photocathode structures. The potential required to reach -10 mA cm^{-2} of current density for hydrogen production using the microwire-based devices was $+210 \text{ mV vs RHE}$ for p-Si and $+300 \text{ mV vs RHE}$ for n⁺p-Si, both of which are among the most positive reported values for Si-based HER photocathodes utilizing earth-abundant materials, without and including a solid-state junction, respectively. Hence, catalyst placement on sidewalls of high-aspect ratio structures is a viable strategy for incorporating large loadings of opaque catalysts directly on the surface of light absorbers.

Chapter 3

SI MICROWIRE-ARRAY PHOTOCATHODES DECORATED WITH CU ALLOW CO₂ REDUCTION WITH MINIMAL PARASITIC ABSORPTION OF SUNLIGHT

Kempler, P. A., Richter, M. H., Cheng, W.H., Brunshwig, B.S., & Lewis, N.S. (2020).

Si Microwire-Array Photocathodes Decorated with Cu Allow CO₂ Reduction with Minimal Parasitic Absorption of Sunlight. *ACS Energy Letters*, 5(8), 2528-2534.

<https://doi.org/10.1021/acsenergylett.0c01334>

3.1 Introduction

Electrochemical reduction of carbon dioxide, CO₂R, to carbon monoxide,⁷⁰⁻⁷¹ methane, ethylene,⁷²⁻⁷³ and other reduced hydrocarbons and oxygenates provides a method of converting an industrial waste product into a feedstock for commodity chemicals and fuels.⁷⁴ Both the activity and selectivity towards the generation of hydrocarbons can be controlled via the preparation of new intermetallic and alloy materials,⁷⁵ but the sum of the absolute partial current densities towards hydrocarbons, $|j_{\text{HC}}|$, at such catalysts is typically $< 1 \text{ mA}\cdot\text{cm}^{-2}$ at overpotentials $< 0.5 \text{ V}$.⁷⁶⁻⁷⁷ Under 1 atm of CO₂(g) and modest overpotentials, $< 0.5 \text{ V}$, the reduction of CO₂ is kinetically limited as opposed to mass-transport limited. Therefore, at a given potential, use of nanostructured, high surface area catalysts will yield an increased $|j_{\text{HC}}|$.⁷⁸⁻⁷⁹

Photoelectrochemical CO₂R, wherein accumulated photogenerated charge carriers lead to a positive shift in the potential required to effect the electrochemical reduction, requires appropriate integration of semiconductors and catalysts.¹⁹ Nanostructured semiconductors have previously been used as photocathodes for CO₂R that produce CO, but not hydrocarbons. Silicon decorated with Ag nanoparticles during metal-assisted chemical etching was illuminated with 50 mW·cm⁻² of simulated sunlight and exhibited absolute photocurrent densities of 8 mA·cm⁻² at -0.5 V vs. the reversible hydrogen electrode (RHE), with > 80% Faradaic efficiency towards CO.⁸⁰ Silicon nanowires decorated with Au₃Cu nanoparticles and under 20 mW·cm⁻² of 740 nm illumination exhibited an absolute photocurrent density > 5.5 mA·cm⁻² at -0.4 V vs. RHE with 67% Faradaic efficiency towards CO.⁸¹ The generation of hydrocarbons has been reported at Si-based photocathodes, but when the catalyst is loaded on the light-facing side of the photoelectrode absolute photocurrent densities, $|J_{ph}|$, have been limited to < 2 mA·cm⁻² at potentials less negative than -1.0 V vs. RHE.⁸²⁻⁸³ Larger absolute photocurrent densities can be obtained when the catalyst is not in the path of incident illumination. For example, a Cu-Ag alloy has been integrated onto the dark-facing side of a p⁺nn⁺-Si light absorber and produced $|J_{ph}| > 30$ mA·cm⁻² at -1.1 V vs. RHE under 100 mW·cm⁻² of Air Mass (AM) 1.5 simulated sunlight.⁸⁴

Herein, we investigate whether Si μ W-arrays can minimize trade-offs between catalyst loading and light collection for light-facing photocathodes effecting CO₂R to hydrocarbons. We demonstrate a Si photocathode with Cu electrodeposited onto the vertical sidewalls of high-aspect ratio microwires that exhibits minimal parasitic absorption by the catalyst with a maximum $|J_{ph}| > 25$ mA·cm⁻² before and after 48 h of

photoelectrochemical CO₂R conditions, leading to the generation of C₂H₄ at more positive potentials than previously reported for photocathodes under 1-Sun illumination. The positive shift in the onset potential for C₂H₄ production, relative to that of a polished Cu foil electrode, exceeded the photovoltage of the n⁺p-Si μW array electrode due to the increased surface area within the internal volume of the μW array. An analytical expression is presented to express the effect of microstructure on the current density vs. potential (*J-E*) behavior of a photoelectrode, as a function of the diode quality factor of the semiconductor and the Tafel slope of the electrocatalyst.

3.2 Experimental Methods

(Photo)electrodepositions of Catalyst: Prior to electrodeposition of Cu, electrodes were rinsed sequentially with acetone, isopropyl alcohol, methanol, and deionized water and then dipped into buffered oxide etchant for 60 s. Electrodepositions were controlled with a BioLogic SP-200 potentiostat. The Cu-plating bath was continuously purged with Ar(g) and contained 0.10 M CuSO₄(aq), 5.0 mM H₂SO₄(aq), and 0.10 M K₂SO₄(aq), at a pH of ~3. A saturated calomel electrode (SCE, CH Instruments) was used as a reference and the counter electrode was a high-purity graphite rod (Alfa Aesar, 5N) (**Figure 3.1A**). The illumination source was an array of narrowband light-emitting diodes (Luxeon Rebel Blue SMD, FWHM 22 nm) with a peak intensity at 465 nm. The illumination wavelength was selected to maximize transmission of light through the colored electrolyte. Cu was deposited potentiostatically at 0.0 V vs. SCE until the desired charge density had passed, normalized to the projected area of the electrode.

Photoelectrochemical CO₂ Reduction Testing: The electrochemical setup was operated in a continuous flow mode. Carbon dioxide was provided to the electrochemical cell at a

flow rate of 5 sccm as controlled by an Alicat flow controller. The carbon dioxide stream was supplied as humidified CO₂ with a gas bubbler placed between the cell and flow controller. The exhaust gases went through a liquid trap, then an Alicat flow meter, and finally to a gas chromatograph (SRI-8610) using a Hayesep D column and a Molsieve 5A column with N₂ as the carrier gas. The gaseous products were detected using a thermal conductivity detector (TCD) and a flame ionization detector (FID) equipped with a methanizer. Quantitative analysis of gaseous products was based on calibrations with several gas standards over many orders of magnitude in concentration. The calibrations were used to calculate the partial current density, j , towards products of the CO₂R and hydrogen evolution reaction. To measure liquid products, the electrolyte on the anode and cathode sides of the cell was sampled at the end of the run and was analyzed by high-performance liquid chromatography (HPLC, Thermo Scientific Ultimate 3000). Products were not quantified in Faradaic efficiency calculations because continuous purging of the catholyte with CO₂ expelled accumulated products. Moreover, crossover of products to the anolyte was observed and oxidation at the anode could potentially occur. An Oriel Instruments 75 W Solar Simulator supplied 100 mW·cm⁻² of AM 1.5 illumination. The light intensity was calibrated using the measured photocurrent at a calibrated (350 to 1100 nm, 1 cm²) NIST traceable Si photodiode (Thorlabs FDS1010-CAL) mounted within the testing cell prior to the addition of the electrolyte.

3.3 Results

Figure 3.1 compares the photoelectrochemical behavior of planar n⁺p-Si to the behavior of a radially doped n⁺p-Si μW-array electrode. A schematic of the photoelectrochemical cell is presented in **Figure 3.1A**. A comparison of the J - E behavior

of illuminated planar n⁺p-Si/Cu and n⁺p-Si μW/Cu electrodes in the plating cell before and after, respectively, -1.00 C·cm⁻² of charge passed towards Cu deposition is presented in **Figure 3.1B**. For the planar n⁺p-Si electrode, $|J_{ph}|$ at -0.2 V vs. the saturated calomel electrode (SCE) decreased by 29% of its initial value, whereas $|J_{ph}|$ for the μW-array electrode remained unchanged from its initial value. The photocurrent at 0.0 V vs. SCE versus Cu loading, as measured by the cathodic charge density passed, is presented in **Figure 3.1C**. Initially, both the planar and μW electrode had similar photocurrent densities. However, for the planar, n⁺p-Si, $|J_{ph}|$ continuously decreased with increased loadings of Cu, whereas at the n⁺p-Si μW electrode, $|J_{ph}|$ increased and then remained nearly constant. Planar and μW electrodes exhibited $|J_{ph}| = 17.9$ and 26.0 mA·cm⁻² after -148 and -1000 C·cm⁻², respectively, had been passed towards Cu deposition. These geometric charge densities were equivalent after renormalization to the greater microstructured area of the μW array and thus the photoelectrochemical behavior was not solely a function of microstructured area.

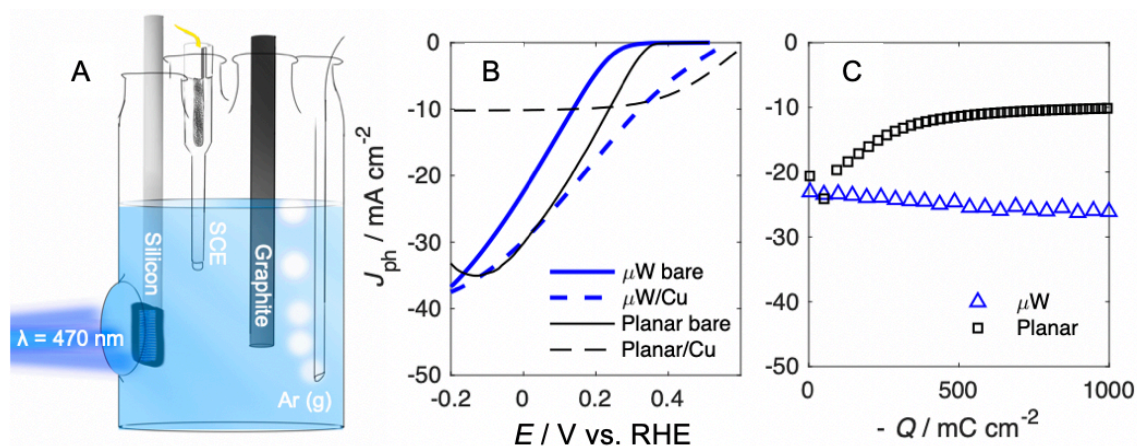


Figure 3.1: (A) Cell schematic for the photoelectrochemical deposition of Cu onto n^+p -Si. (B) Photoelectrochemical $J_{\text{ph}}-E$ behavior of n^+p -Si μW (blue lines) and planar n^+p -Si (black lines) in an Ar purged Cu deposition bath, before (solid) and after (dashed) passage of $-1.00 \text{ C}\cdot\text{cm}^{-2}$. Linear sweep voltammograms were recorded at $-200 \text{ mV}\cdot\text{s}^{-1}$. (C) $J_{\text{ph}}-Q$ behavior for n^+p -Si μW and planar n^+p -Si during photoelectrochemical deposition of Cu at 0.0 V vs. SCE.

Scanning-electron micrograph, SEM, images of electrodeposited Cu on planar n^+p -Si and n^+p -Si μW electrodes are presented as **Figure 3.2**. On the planar electrode, Cu electrodeposited as discontinuous particles that began to merge at high loadings, leading to nearly continuous islands that were distributed unevenly and were prone to delamination (**Figure 3.2A-B**). In contrast, on n^+p -Si μW electrodes, nominally identical Cu loadings, as measured by the geometric charge density passed, led to discontinuous catalyst films that were distributed across the tips, sidewalls, and base of the μW array (**Figure 3.2C**). The Si μW -array was composed of cylinders with a nominal diameter, pitch, and height of 3, 7, and 30 μm , respectively, leading to a microstructured area 6.8 times that of a planar surface. A few Cu particles $\sim 5 \mu\text{m}$ in diameter were visible on the tips of individual wires (**Figure 3.2D**).

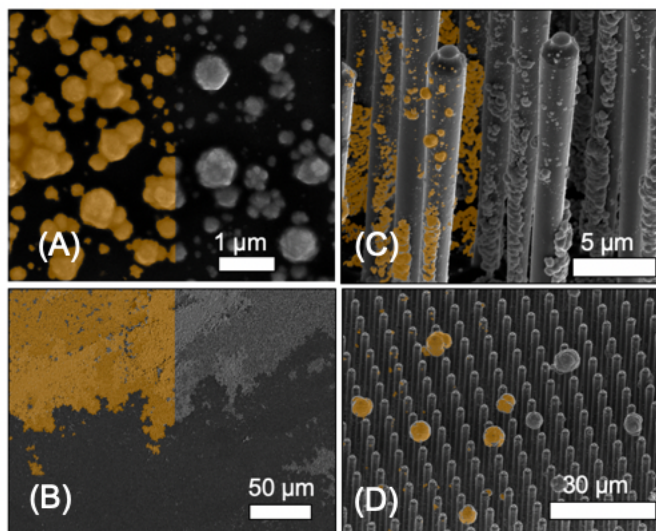


Figure 3.2: False-color SEM images of Cu (orange) photoelectrodeposited onto planar n⁺p Si after (A) -148 mC·cm⁻² (B) and -1.00 C·cm⁻² geometric charge density had been passed. (C-D) n⁺p-Si μW after a geometric charge density of -1.00 C·cm⁻² had been passed.

The n⁺p-Si μW/Cu electrodes were evaluated as photocathodes for CO₂R, with online GC-FID/TCD detection of gaseous products, to determine the activity of the microstructured catalyst film and the effects of the photovoltage on the product distribution. **Figure 3.3A** compares the *J-E* behavior of an electropolished Cu foil in the dark to an illuminated n⁺p-Si μW/Cu electrode in 0.10 M KHCO₃ saturated with CO₂(g) at 1 atm. Illumination produced a substantial positive shift in the onset of cathodic current, with a saturated $|J_{\text{ph}}|$ of 31 ± 3 mA·cm⁻² observed at -0.62 V vs. RHE. The partial current density behaviors, j_x-E , of Cu deposited on n⁺p-Si μW catalyzing the formation of CO, CH₄, and C₂H₄ consistently shifted towards more positive potentials, with the magnitude of the shift varying for different reduction products (**Figures 3.3-3.4**). The activity of n⁺p-Si μW/Cu electrodes towards H₂ was larger than that of a Cu foil (**Figure 3.4**).

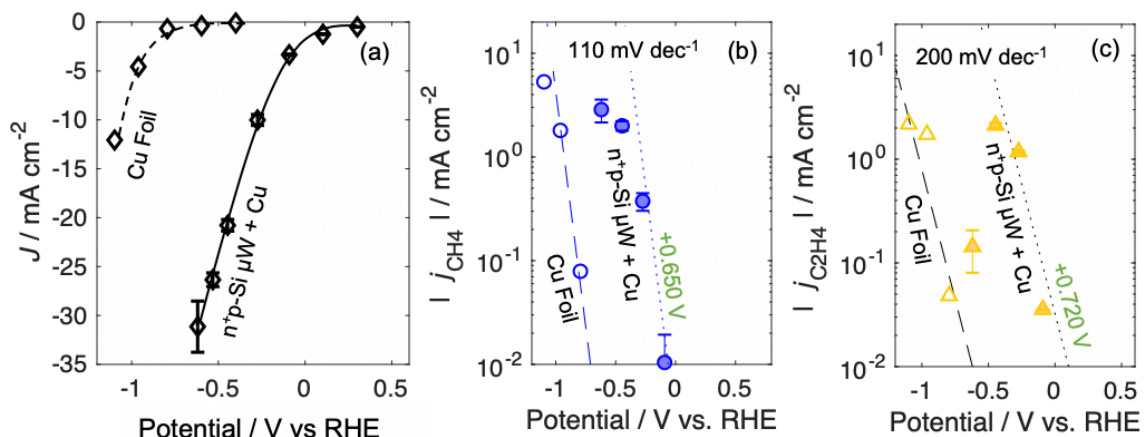


Figure 3.3: (A) J - E behavior of electropolished Cu (open markers) in 0.10 M KHCO₃(aq) to the photoelectrochemical J_{ph} - E behavior of n⁺p-Si μW (filled markers) under 100 mW·cm⁻² simulated sunlight in a nominally identical electrochemical cell. (B) Absolute partial current density towards CH₄ vs. potential, j_{CH_4} - E , behavior measured via online GC-FID/TCD, for electropolished Cu and n⁺p-Si μW. (C) Absolute partial current density towards C₂H₄ vs. potential, $j_{C_2H_4}$ - E , behavior measured via online GC-FID/TCD, for electropolished Cu and n⁺p-Si μW. Guidelines in (B,C) represent predicted behavior from measured Tafel slopes and photovoltages (*vide infra*).

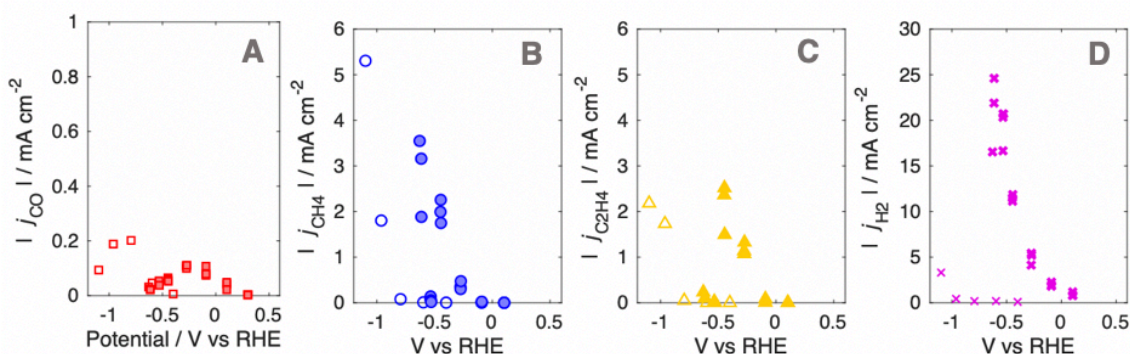


Figure 3.4: Plots of the partial current densities towards (photo)electrochemical CO₂R products vs. potential for n⁺p-Si μW/Cu electrodes (filled markers) compared to planar Cu electrodes (open markers). (A) j_{CO} - E behavior for production of CO, (B) j_{CH_4} - E behavior for production of CH₄, (C) $j_{C_2H_4}$ - E behavior for production of C₂H₄, and (D) j_{H_2} - E behavior for production of H₂, detected by online GC-FID/TCD.

The n⁺p-Si μW/Cu electrode exhibited a peak $|j_{\text{C}_2\text{H}_4}|$ of $2.1 \pm 0.2 \text{ mA}\cdot\text{cm}^{-2}$ at a potential of -0.44 V vs. RHE, and the peak $|j_{\text{CH}_4}|$ of $2.9 \pm 0.7 \text{ mA}\cdot\text{cm}^{-2}$ was observed at -0.62 V vs. RHE. The total $|j_{\text{HC}}|$ at $E = -0.44 \text{ V}$ vs. RHE was $4.1 \pm 0.2 \text{ mA}\cdot\text{cm}^{-2}$. Onset potentials for H₂ and CO were positive of RHE, while those for C₂H₄ and CH₄ generation were observed at -0.09 V vs. RHE.

Delamination of Cu films from planar n⁺p-Si/Cu electrodes during electrolysis led to increasing photocurrents and decreasing activity towards photoelectrochemical CO₂R. The average j_{CH_4} was $-0.9 \pm 0.3 \text{ mA}\cdot\text{cm}^{-2}$ and $-0.7 \pm 0.3 \text{ mA}\cdot\text{cm}^{-2}$, during the first 10 min of electrolysis, for n⁺p-Si/Cu photoelectrodes having a catalyst loading of $-148 \text{ mC}\cdot\text{cm}^{-2}$ and $-1.00 \text{ C}\cdot\text{cm}^{-2}$, respectively. The declined activity of planar n⁺p-Si/Cu electrodes within the first 20 min of controlled potential electrolysis prevented a quantitative assessment of the J - E behavior. The loss in activity was likely due to passivation of the Si/Cu interface and/or more rapid poisoning of the reduced catalyst surface area relative to the behavior of Cu in Si μW-arrays.

The stability of n⁺p-Si μW/Cu electrodes was investigated via extended chronoamperometry at -0.58 V vs. RHE under $100 \text{ mW}\cdot\text{cm}^{-2}$ of Air Mass (AM) 1.5 simulated sunlight (details on intensity calibrations are provided in the Appendix, **A.3**). After an initial increase in $|J_{\text{ph}}|$ upon reduction of Cu to its metallic state, the maximum photocurrent density remained stable for 48 h under constant potential (**Figure 3.5A**). The J - E behavior of the n⁺p-Si μW/Cu electrode, as measured via linear sweep voltammetry at a scan rate of $-50 \text{ mV}\cdot\text{s}^{-1}$ at 4 h intervals during the chronoamperometry, indicated that the optical properties of the integrated Si/Cu microstructure, the photovoltage of the n⁺p-Si junction, and the electrical resistance of the Si/Cu interface remained stable after a brief

initial period of activation (**Figure 3.5A**). Greater than 90% of the photocurrent density eventually resulted in the formation of $\text{H}_2(\text{g})$ (**Figure 3.5C**). During continuous potential control of $\text{n}^+\text{p-Si } \mu\text{W/Cu}$ electrodes at -0.58 V vs. RHE , $|j_{\text{C}_2\text{H}_4}|$ and $|j_{\text{CH}_4}|$ decreased after 4 and 8 h, respectively, whereas $|j_{\text{CO}}|$ increased with time (**Figure 3.5D**).

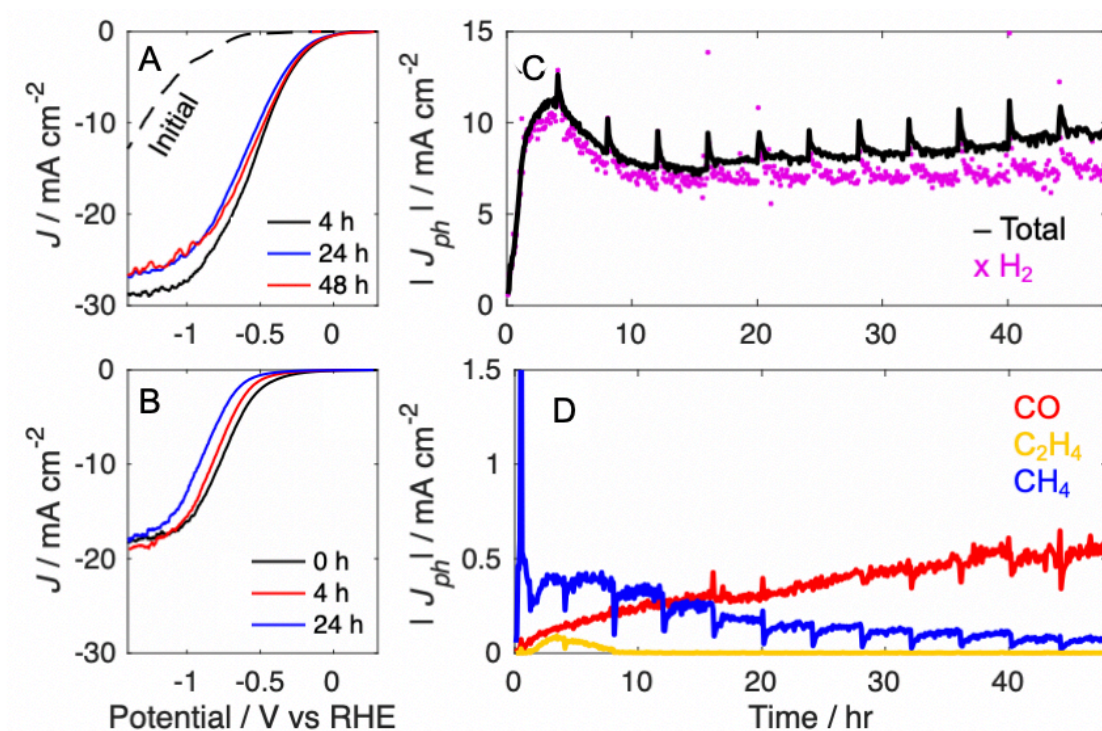


Figure 3.5: Photoelectrochemical data for $\text{n}^+\text{p-Si Cu}$ electrodes during stability evaluation at -0.58 V vs. RHE in CO_2 -purged $0.10 \text{ M KHCO}_3(\text{aq})$ under $100 \text{ mW}\cdot\text{cm}^{-2}$ simulated sunlight. (**A-B**) Time dependent J - E behavior for a (**A**) $\text{n}^+\text{p-Si } \mu\text{W/Cu}$ electrode and (**B**) planar $\text{n}^+\text{p-Si/Cu}$ electrode, loaded with -1.00 and -0.148 C cm^{-2} , respectively, as measured by a linear sweep voltammogram recorded at a scan rate of $50 \text{ mV}\cdot\text{s}^{-1}$. (**C**) Absolute photocurrent density and partial photocurrent density towards $\text{H}_2(\text{g})$, as measured via GC-FID/TCD, represented as black x's and a gray line, respectively for a $\text{n}^+\text{p-Si } \mu\text{W/Cu}$ electrode. (**D**) Absolute partial photocurrent density towards $\text{CO}(\text{g})$, $\text{C}_2\text{H}_4(\text{g})$, and $\text{CH}_4(\text{g})$ presented as red, gold, and blue lines, respectively for a $\text{n}^+\text{p-Si } \mu\text{W/Cu}$ electrode.

Aqueous products were collected from the electrolyte in the cathode and anode compartments at the conclusion of the 48 h chronoamperometry stability experiment and were analyzed via HPLC. SEM images of the n^+p -Si μ W electrode (**Figure 3.6**) showed that the morphology of the deposited Cu catalyst particles changed during extended chronoamperometry, whereas the morphology of the Si μ W-array electrode remained unchanged.

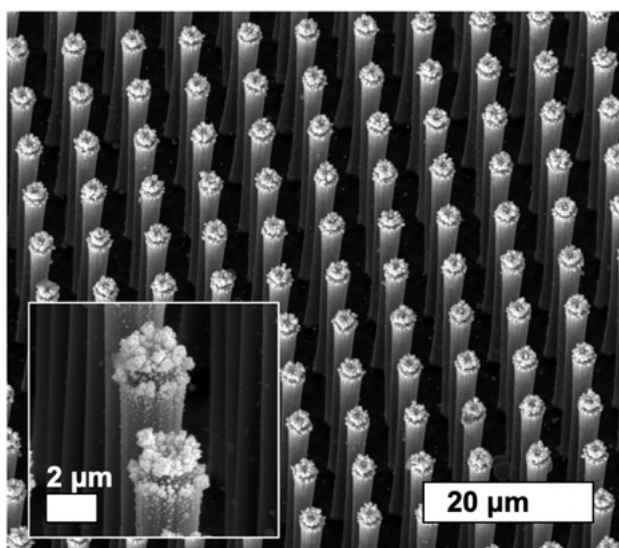


Figure 3.6 SEM of an n^+p -Si- μ W/Cu photocathode after 96 h of continuous photoelectrochemical operation in CO_2 -purged 0.10 M $\text{KHCO}_3(\text{aq})$ under $100 \text{ mW}\cdot\text{cm}^{-2}$ of simulated sunlight. Primary scale bar represents 20 μm , inset scale bar represents 2 μm .

3.4 Discussion

Arrays of vertically-oriented Si μ Ws allow for high mass loadings of electrodeposited Cu on the light-facing side of photoelectrodes without substantial reductions in $|J_{\text{ph}}|$ (**Figure 3.1C**). Despite the high ($0.33 \text{ mg}\cdot\text{cm}^{-2}$) mass loading of electrocatalyst on the light-facing side of the electrode (Equation A.3.1), n^+p -Si μ W/Cu

electrodes exhibited absolute photocurrent densities $> 30 \text{ mA}\cdot\text{cm}^{-2}$ under AM 1.5 simulated solar illumination. The predicted $|J_{\text{ph}}|$ at a $500 \text{ }\mu\text{m}$ thick Si slab in air, under AM 1.5 simulated solar illumination is $29 \text{ mA}\cdot\text{cm}^{-2}$ and uncovered, planar $\text{n}^+\text{p-Si}$ in $0.50 \text{ M H}_2\text{SO}_4(\text{aq})$ under AM 1.5 simulated solar illumination exhibited a limiting $|J_{\text{ph}}|$ of 27.5 mA cm^{-2} .^{44, 63} The generation rate of hydrocarbons at $\text{n}^+\text{p-Si } \mu\text{W/Cu}$ electrodes in $0.10 \text{ M KHCO}_3(\text{aq})$ saturated with $\text{CO}_2(\text{g})$ matched or exceeded the performance of an electrode possessing the electrocatalytic activity of an electropolished Cu film in series with the photovoltage of a microstructured Si photovoltaic (**Figure 3.3-3.4**).

The yield of hydrocarbon and oxygenate products in the (photo)electrochemical CO_2R is a function of both the catalyst used and the overpotential. Decreasing the coverage of catalysts on a photoelectrode can lead to increased light transmission, photocurrent, and photovoltage but will adversely affect the total rate of reaction if kinetic losses at the catalysts are not overcome by the increased photovoltage. Furthermore, the regions responsible for catalysis and light absorption must be within the diffusion length of the excited charge carriers to prevent losses due to carrier recombination. Microstructured semiconductors provide additional surface area for light collection and electrocatalysis, but must overcome a reduction in photovoltage due to the increased surface area available for recombination. The photovoltage, V_{ph} , provided by a microstructured semiconductor with a junction uniformly distributed across the surface is described by **Equation 3.1**:

$$V_{\text{ph}}(J) = \frac{2.3nk_bT}{q} \log_{10} \left(\frac{|J_{\text{ph}}| - |J|}{(R_{\mu})|J_0|} + 1 \right) \quad (3.1)$$

where n is the diode quality factor, k_b is Boltzmann's constant, T is the operating temperature, q is the unsigned elementary charge, J_0 is the dark current density across the charge-separating junction, and R_{μ} is the ratio of the microstructured area to the geometric

area. Current densities are normalized to the geometric area of the device. **Equation 3.2** represents the η - J relationship at electrocatalysts on a microstructured electrode as described by the Tafel equation:

$$\eta(J) = b \log_{10}(|J|/R_{\mu}) - a \quad (3.2)$$

where b is the measured Tafel slope and a can be calculated from the measured exchange current density.⁴⁷

The effect of increasing the microstructured area of a photoelectrode on the illuminated j - E behavior can be described by the sum of **Equations 3.1** and **3.2**. Increasing the microstructured area at an ideal diode ($n = 1$) leads to a $60 \text{ mV}\cdot\text{dec}^{-1}$ reduction in $|V_{\text{ph}}|$, whereas the reduction in $|\eta|$ depends on the Tafel slope of the catalyst (**Figure 3.6A**). The Tafel slopes for Cu catalyzing CO_2R to CH_4 and C_2H_4 in $0.50 \text{ M KHCO}_3(\text{aq})$ have been reported as $110 \text{ mV}\cdot\text{dec}^{-1}$ and $200 \text{ mV}\cdot\text{dec}^{-1}$, respectively.²⁶ Hence microstructured photocathodes prepared from ideal diodes decorated with Cu will produce C_2H_4 at more positive potentials than an equivalent planar photocathode (**Figure 3.6B**). For catalysts that exhibit small Tafel slopes $< 60 \text{ mV}\cdot\text{dec}^{-1}$, e.g. Pt effecting the HER at pH 0 ($b = 28 \text{ mV}\cdot\text{dec}^{-1}$), reductions in photovoltage will match or exceed reductions in the overpotential that result from microstructuring, leading to a negative potential shift in the j - E behavior (**Figure 3.6B**). For $b = 60 - 120 \text{ mV}\cdot\text{dec}^{-1}$ the net effect of microstructuring depends on n , while for $b > 120 \text{ mV}\cdot\text{dec}^{-1}$, in the absence of mass transport limitations, reductions in V_{ph} will typically be fully offset by reductions in η (**Figure 3.6C**).

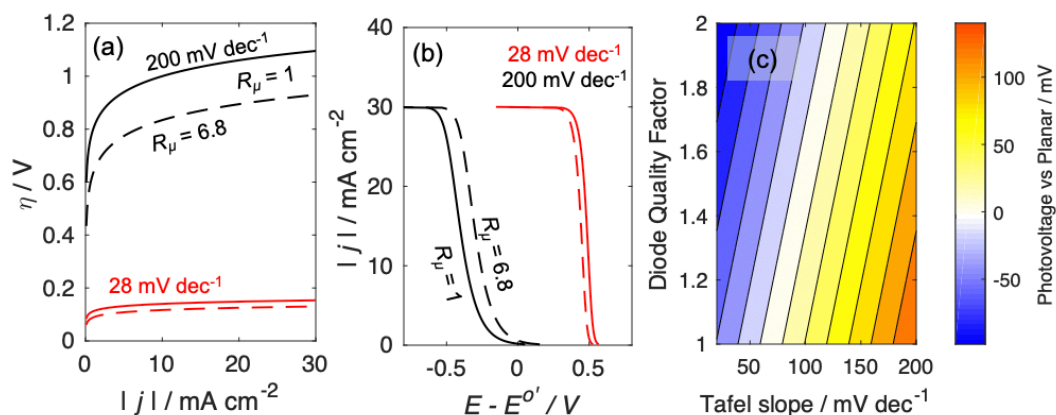


Figure 3.6: (A) η - J behavior for planar ($R_\mu = 1$), continuous lines, and μ W ($R_\mu = 6.8$), dashed lines, for electrocatalysts exhibiting $b = 0.028$ and $0.200\ V\cdot dec^{-1}$, shown in red and black, respectively. (B) j - E behavior calculated from the sum of Equations 1 and 2 for planar, continuous lines, and μ W, dashed lines, photocathodes as a function of b , for $J_{ph} = 30\ mA\cdot cm^{-2}$ and $n = 1.3$. (C) Contour lines comparing the shift in photovoltage at $|J_{ph}| = 10\ mA\cdot cm^{-2}$, due to increasing R_μ by a factor of 10, as a function of n and b . Details on the calculations are provided in the Appendix, A.3.

The observations herein demonstrate that microstructured photoelectrodes can yield a positive shift in the j - E behavior in excess of the photovoltage of a planar semiconductor, thereby increasing j_{CO_2R} . Semi-log plots of $|j_{CH_4}|$ and $|j_{C_2H_4}|$ versus E for planar and μ W n^+p -Si electrodes exhibited mutually similar Tafel slopes that were moreover in agreement with literature values (Figure 3.3B-C).⁸⁵ Over a range of photocurrent densities relevant to solar-fuels device operation, planar n^+p -Si junctions ($R_\mu = 1$) exhibited $n = 1.3$ and $J_0 = 9 \times 10^{-10}\ A\cdot cm^{-2}$, whereas μ W n^+p -Si junctions ($R_\mu = 6.8$) exhibited $n = 2.5$ and $J_0 = 7 \times 10^{-7}\ A\cdot cm^{-2}$ (Figure A.3). The value of J_0 increased for the radial-junction relative to the planar junction, possibly as a consequence of the reactive-etching process. This explanation is consistent with the large value of n observed at the

μW junction. Relative to the planar $\text{n}^+\text{p-Si}$ junction, the reduction in $|V_{\text{ph}}|$ obtained at the μW $\text{n}^+\text{p-Si}$ junction was less than the expected V_{ph} based on changes to J_o , due to the simultaneous increase in n . At $|J_{\text{ph}}|$ comparable to those observed under simulated sunlight ($30 \text{ mA}\cdot\text{cm}^{-2}$), the μW junction yielded a V_{ph} that was 14 mV less than the planar junction. Based on the increased catalyst area and the measured V_{ph} , the predicted potential shifts in j_{CH_4} and $j_{\text{C}_2\text{H}_4}$ at the μW $\text{n}^+\text{p-Si/Cu}$ electrode are 0.650 and 0.720 V, respectively. The $j_{\text{C}_2\text{H}_4}$ - E data were in close agreement with the predicted values, while the j_{CH_4} - E data were shifted less positive, relative to polycrystalline Cu, than the predicted shift (**Figure 3.3B-C**). Details on the calculations of the potential shift in j_x - E are provided in the Appendix, **A.3**.

The onset of photocurrent at front-side illuminated $\text{n}^+\text{p-Si}$ $\mu\text{W/Cu}$ electrodes was observed at potentials $> 1 \text{ V}$ more positive than those previously reported at p-Si/Cu electrodes.⁸³ Planar $\text{n}^+\text{p-Si}$ with Cu at low or high catalyst loadings did not produce C_2H_4 in quantities sufficient for quantification and exhibited $j_{\text{CH}_4} < 0.5 \text{ mA}\cdot\text{cm}^{-2}$ within 20 min of potential control at -0.598 V vs. RHE. This behavior indicates that Cu loadings suitable for transmission of light on planar surfaces have low activity and/or electrochemical stability towards CO_2R . Glass with a 45 nm Cu film reflects $> 90\%$ of photons at wavelengths $> 600 \text{ nm}$ and $> 50\%$ of photons at wavelengths between 400–600 nm.⁸⁶ $|J_{\text{ph}}|$ values obtained at planar and μW $\text{n}^+\text{p-Si/Cu}$ photocathodes were larger than what would be expected given coverage of the surface with a continuous film, consistent with the discontinuous coating of opaque metal islands observed via SEM (**Figure 3.2B**). Semiconductors that cannot be readily microstructured or which exhibit high diode quality factors could benefit from the use of transparent, high surface-area, conductive supports for metallic catalysts for CO_2R .⁸⁷

High photocurrent densities were sustained at n⁺p-Si μW/Cu photocathodes for 48 h of photoelectrochemical operation, demonstrating that the exposed Si surfaces were passivated towards dissolution and that the electrical contact between the light-absorber and catalyst islands was stable (**Figures 3.4**). Prior experimental results on the electrocatalytic activity of Cu towards CH₄ and C₂H₄ in 0.1 M KHCO₃(aq) have been assessed on timescales ≤ 1 h, commensurate with the stability of photoelectrodes in this work.^{73, 88} Experiments conducted in flowing electrolytes have yielded Faradaic efficiencies which are significantly more stable towards CO₂R. A $|j_{\text{CO}}| > 130 \text{ mA cm}^{-2}$ was demonstrated for 100 h at PTFE-supported Ag in flowing 1 M KOH(aq).⁸⁹ Carbon-nanoparticle-supported Cu has yielded $|j_{\text{C}_2\text{H}_4}| \geq 50 \text{ mA cm}^{-2}$ for 150 h in flowing 7 M KOH(aq).⁹⁰ Increases in j_{H_2} and j_{CO} with time at n⁺p-Si μW/Cu photocathodes could be due to deposition of metal impurities from the solution either onto the Cu surface, reducing the catalytic efficiency of the Cu for CO₂R, or deposition onto the bare Si surface increasing its catalytic efficiency for H₂ and CO (**Figure 3.4**). Crossover of dissolved Pt from the anode to the Cu or Si surface could play this role. Inductively-coupled plasma mass-spectrometry and XPS, following a 5 day galvanostatic experiment at 10 mA in 0.10 M KCHO₃(aq) using a Pt foil anode and graphite cathode separated by a Selemion AMV membrane confirmed the presence of dissolved Pt in the anolyte and catholyte, and plating of metal onto the graphite surface (**Figure 3.7**). The graphite cathode was chosen so that peaks in the Pt 4f region of the XPS data could be resolved without interference from the substantially more intense Cu 3p peak. Photoelectrochemical cells that use the same catalyst for both CO₂R and water oxidation have been beneficially used to avoid such poisoning.⁹¹

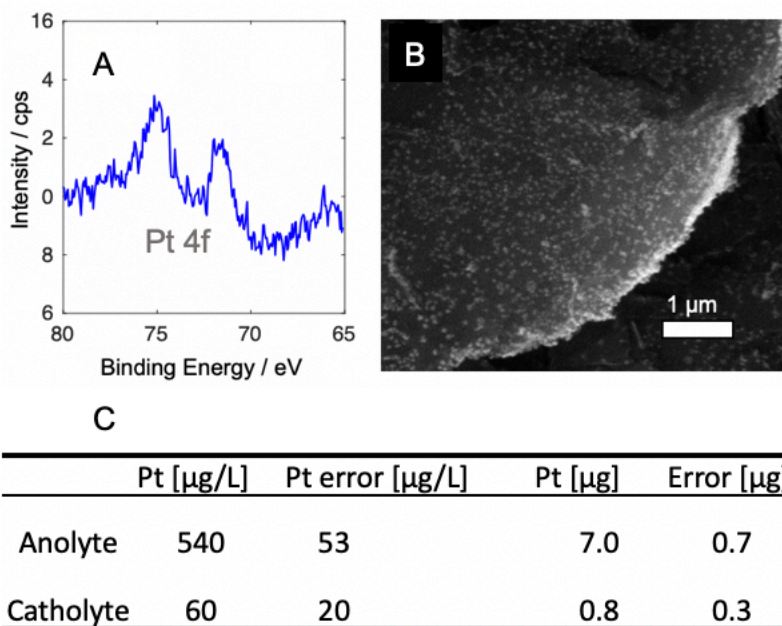


Figure 3.7: (A) X-ray photoelectron spectra of the surface of a graphite cathode in the Pt 4f region after 5 days under galvanostatic control at -10 mA in 0.10 M $\text{KHCO}_3(\text{aq})$. The graphite cathode was separated from a Pt anode by a Selemion membrane. (B) SEM image of the surface of the graphite surface measured in (A). Small metal nanoparticles, visible as white dots, were not present prior to the galvanostatic experiment. (C) Dissolved Pt concentration in the anolyte and catholyte, measured via inductively-coupled plasma mass-spectrometry, following a 5 day experiment with a constant current of 10 mA applied between a Pt foil anode and graphite cathode separated by Selemion AMV membrane.

Backside illuminated, textured Si photocathodes exhibit a $|j_{\text{HC}}|$, of $< 2 \text{ mA}\cdot\text{cm}^{-2}$ at -0.4 V vs. RHE.²⁵ Although the $\text{n}^+\text{p-Si } \mu\text{W/Cu}$ photocathodes reported herein exhibited a larger total $|j_{\text{HC}}| > 4 \text{ mA}\cdot\text{cm}^{-2}$ at -0.44 V vs. RHE, substantially lower Faradaic efficiencies were observed towards CO_2R relative to these previous reports. Cu supported on Ag has been shown to suppress the generation of $\text{H}_2(\text{g})$ such that greater Faradaic efficiencies towards hydrocarbons can be obtained.³³ CuAg alloys could be integrated onto Si μW -arrays to reduce the partial current density towards H_2 ,⁹² but at backside illuminated Si

photocathodes the HER was not suppressed without complete coverage of the photocathode surface by catalyst,⁸⁴ which is incompatible with the microstructuring strategy employed herein. Alternatively, suppression of the parasitic photocurrent density towards H₂ by passivation of the exposed light absorbing regions with an insulating, chemically inert layer such as SiN_x could lead to increased photovoltages and Faradaic efficiencies for CO₂R.⁹³

The results from this work have important applications in designs for electrode systems that use H₂O and CO₂ to store sunlight as fuels. Mass loadings of Cu, sufficient to meet the *j-E* behavior of a Cu foil, can be deposited on the light-absorbing surface of a microstructured photocathode for which the reduction in overpotential due to the microstructured surface area can meet or exceed the reductions in photovoltage due to increased dark current. Microstructured semiconductors will be required to ensure efficient and stable solar fuels generation so that membranes can be incorporated at length scales smaller than the minority-carrier diffusion length in the semiconductor.²² Although the Si μ W arrays in this work were formed via reactive-ion etching, similar structures can be grown from gas precursors such as SiCl₄ and SiH₄, over large areas, and have been used as efficient photocathodes.²⁹

Electrochemical reactions that consume protons generate pH gradients that can lead to shifts in the product distribution. Previous studies on micro- and nanostructured cathodes have used proton-concentration gradients to suppress the hydrogen-evolution reaction and increase the Faradaic efficiency of Au towards CO production.⁹⁴⁻⁹⁵ The short, sparse microwire array used in this work exhibited a similar product distribution relative to the polished Cu foil. The Tafel slopes were also mutually similar for both types of electrodes.

Future studies on densely packed microwire arrays with heights greater than the boundary layer thickness would enable the effects of concentration gradients of protons and $\text{CO}_2(\text{aq})$ within the electrode to be explored. In this work, photocathodes were operated under 1 atm of CO_2 and at near-neutral pH. In contrast, practical devices will require a concentrated source of CO_2 , higher pH values, forced convection of the electrolyte to minimize the thickness of the concentration boundary layer, and/or methods of interconverting HCO_3^- (aq) and $\text{CO}_2(\text{aq})$ to sustain $|J_{\text{ph}}|$ equal or greater than the values reported herein for devices covering areas relevant to commercial, scalable fuel formation.⁹⁶

3.5 Conclusion

Vertically oriented Si μW arrays allowed for the integration of discontinuous, electrodeposited Cu films at mass-loadings sufficient to drive photoelectrochemical CO_2R at overpotentials comparable to a continuous planar Cu film, while maintaining stable photocurrent densities comparable to those exhibited by a planar Si surface with no Cu. Metallic catalysts that exhibit large Tafel slopes and primarily reflect, rather than absorb, light benefit from this method of semiconductor-catalyst integration. The $|J_{\text{ph}}|$ obtained at the $\text{n}^+\text{p-Si } \mu\text{W}/\text{Cu}$ electrodes under 1 Sun illumination in this work are among the highest reported values for photocathodes for CO_2R , independent of where the catalyst was located. Thus, semiconductors that can be structured into high-aspect ratio features, larger than a wavelength of light, are suitable for integration with high loadings of metallic electrocatalysts for photoelectrochemical devices.

Chapter 4

INTEGRATION OF ELECTROCATALYSTS WITH SILICON MICROCONE ARRAYS FOR MINIMIZATION OF OPTICAL AND OVERPOTENTIAL LOSSES DURING SUNLIGHT- DRIVEN HYDROGEN EVOLUTION

Yalamanchili, S.,* Kempler, P. A.,* Papadantonakis, K. M., Atwater, H. A., & Lewis, N. S. (2019). Integration of electrocatalysts with silicon microcone arrays for minimization of optical and overpotential losses during sunlight-driven hydrogen evolution. *Sustainable Energy & Fuels*, 3(9), 2227-2236. <https://doi.org/10.1039/C9SE00294D>

4.1 Introduction

Polished Si photocathodes exhibit light-limited photocurrent densities $|J_{\text{ph}}| < 29 \text{ mA cm}^{-2}$, due to optical losses arising from front-surface reflection.⁹⁷ $|J_{\text{ph}}|$ can approach the theoretical maximum of $\sim 44 \text{ mA cm}^{-2}$ for Si under 100 mW cm^{-2} of Air Mass 1.5 illumination⁹⁸ by use of an antireflective coating, combined with surface texturing such as micropyramids (μ -pyramids) produced by anisotropic wet-chemical etching, or by high-aspect ratio structuring of the Si.^{43, 99-101} Antireflective coatings such as SiO_2 , Si_3N_4 , or Al_2O_3 , as commonly used in photovoltaic devices, are not catalytically active or electronically conductive; the use of such materials in a photoelectrode system in which charge-transfer occurs across the illuminated solid/liquid interface requires separation of regions responsible for charge transfer and light absorption.^{93, 102} Si photocathodes with a

passivated front surface and Pt loaded on the rear surface, out of the path of incident light, exhibit photovoltages in excess of 630 mV under 1 Sun illumination and exhibit limiting photocurrent densities that are relatively independent of the mass loading of electrocatalyst.¹⁰³

Most of the highly active catalysts for fuel production reflect and parasitically absorb light in the solar spectrum. These optical losses by the catalyst can be reduced by decreasing the catalyst loading to increase transmissivity,¹⁰⁴ by developing transparent and antireflective catalysts,^{51, 105} by depositing the catalyst as islands rather than as a continuous film;¹⁰⁶ and/or by strategically placing the catalyst out of the path of incident light on three-dimensionally structured Si substrates.⁴⁰ On planar surfaces, increases in the catalyst loading and/or surface coverage decrease the effective current density at the catalyst, so the reduced overpotential and consequent increase in fill factor can partially offset the efficiency losses that would otherwise result from a decrease in J_{ph} .¹⁰⁶ The ideal electrode microstructure would therefore simultaneously minimize reflection and absorption losses in the catalyst while optimizing the catalyst loading to reduce the overpotential required to convert photogenerated charge carriers into fuel.

H₂-evolving Si photocathodes have been made using surface texturing such as μ -pyramids,^{51, 107} nanowires,^{50, 108-110} and microwires (μ -wires).^{30, 39, 54, 104} Light-limited current densities as high as $|J_{ph}| = 43 \text{ mA cm}^{-2}$ have been reported for Si μ -pyramids coated with a highly transparent and potentially antireflective MoS_xCl_y catalyst grown by chemical-vapor deposition.⁵¹ A photocurrent density at the reversible hydrogen electrode (RHE) potential, $J_{RHE} = -37.5 \text{ mA cm}^{-2}$ was obtained for over 30 min, using a transparent NiCoSe_x catalyst formed via light-assisted electrodeposition onto Si nanowire array

photocathodes.⁵⁰ For Si microwires (μ -wires), $J_{\text{RHE}} = -35.5 \text{ mA cm}^{-2}$ was obtained by optimizing both the coverage of an electrodeposited Ni-Mo catalyst on the μ -wires and the pitch of the μ -wires.⁵⁴ Replacing the catalyst in these structures with thin Pt ($\sim 5 \text{ nm}$ or less), which is widely used because of its high activity and stability in corrosive environments, led to substantial optical absorption and reflection losses, and produced a decrease of $5\text{--}7 \text{ mA cm}^{-2}$ in $|J_{\text{RHE}}|$.^{50-51, 54}

Polymer-embedded Si μ -wires with an antireflective Si_3N_4 coating and scattering particles can absorb up to 84.4% of the incident radiation at normal incidence, which is above the light-trapping limit for an equivalently thick Si substrate.^{30, 111} However, widely spaced Si μ -wires on a Si substrate reflect $>30\%$ of normally incident light, due to the flat tops of the μ -wires. In contrast, tapering the cylindrical shape of Si μ -wires into Si microcones (μ -cones) with a tip curvature of 25 nm enhances the absorption of Si to $> 90\%$ at normal incidence, equivalent to 99.5% of the classical broadband light-trapping limit, with above-the-limit absorption observed at long wavelengths.^{43, 101} Such Si μ -cones reflect only $\sim 1\%$ of normally incident light, which is comparable to the reflection from black silicon substrates.^{99-100, 112} This behavior arises from the coupling of broad-band light to multiple available waveguide modes whose resonance exists at various radii resulting from the conical geometry.^{43, 113-114} The high surface area for catalyst loading provided by the μ -cone geometry makes Si μ -cones an attractive architecture for Si photocathodes in hydrogen-producing systems. Herein we investigate the H_2 -evolution performance of Si μ -cone array photocathodes coupled with either a highly active but reflective thin film of Pt catalyst, or with a discontinuous film of Co-P as an example of an electrocatalyst composed of earth-abundant elements. Si μ -cones were removed from the substrate in a

flexible polymer support leading to devices which demonstrated H₂ evolution at potentials positive of RHE.

4.2 Experimental Methods

(Photo)electrochemical measurements: The performance of photocathodes for photoelectrochemical hydrogen evolution was measured in H₂-purged 0.50 M H₂SO₄(aq) (TraceMetals grade, Fisher) under 100 mW cm⁻² of simulated AM1.5 illumination produced by a filtered Hg (Xe) lamp powered at 290 W. A Biologic SP-200 was used for the potentiostat, and the electrochemical cell had a three-electrode configuration. A Ag/AgCl (Saturated KCl) or Saturated Calomel reference electrode was calibrated against the RHE potential using a platinum-black electrode, and a graphite rod positioned behind a porous glass frit served as the counter electrode. Current density vs potential, *J-E*, data were obtained by sweeping the potential at 50 mV s⁻¹ from open circuit to -0.2 V vs RHE. The electrolyte was stirred rapidly with a magnetic stir bar, to remove hydrogen bubbles from the surface of the device.

Spectral response measurements: The external quantum yield of n⁺p-Si/Ti/Pt and p-Si/Co-P μ-cone arrays were recorded using a Biologic VMP3 Multichannel potentiostat connected to a lock-in amplifier with illumination from a Xe lamp powered at 150 W passed through a monochromator controlled via LabView and chopped at 10-15 Hz. Spectra were referenced to a calibrated reference diode (Thorlabs FDS100-CAL). The potential of p-Si/Co-P photocathodes was held at -200 mV vs RHE to ensure that the sample remained under reductive bias in the dark, while the potential of n⁺p-Si/Ti/Pt photocathodes was held at 0 V vs RHE.

Details on the fabrication of n^+p -Si/Pt, p-Si/Co-P μ -cones, and membrane embedded photocathodes, as well as experimental procedures for stability testing are provided in the Appendix (A.4).

4.3 Results and Discussion

4.3.1 Homojunction Si photocathodes with sputtered Pt catalyst

Arrays of Si μ -cones with n^+p homojunctions were prepared by inductively coupled plasma reactive-ion etching (ICP-RIE) of a patterned $\langle 100 \rangle$ -oriented p-type Si wafer, followed by diffusion doping with P to form the n^+ emitter layer (experimental details are provided in the Appendix (A.1 and A.4) **Figure 4.1 (A-F)** schematically shows the fabrication process for the n^+p -Si μ -cone array photocathodes, with the tips of the μ -cones supporting a Pt catalyst (n^+p -Si/Pt μ -cones) for the hydrogen-evolution reaction (HER). **Figure 4.1G** shows a scanning-electron micrograph (SEM) of a cross section of an as-prepared n^+p -Si/Pt μ -cone array photocathode with Pt covering 6-9 μm at the tips of the μ -cones.

Figure 4.2 compares the current density vs potential (J - E) behavior under 100 mW cm^{-2} of simulated AM1.5 illumination for varied thicknesses of Pt deposited onto as-fabricated n^+p -Si/Pt μ -cone array photocathodes, planar n^+p -Si/Pt photocathodes, and pyramidally-textured n^+p -Si/Pt photocathodes (μ -pyramid), when operated in contact with H_2 -saturated 0.50 M $\text{H}_2\text{SO}_4(\text{aq})$. Of the three photocathode geometries, the μ -cone array exhibited the highest light-limited photocurrent density $|J_{\text{ph}}|$ (at large negative biases, < -1.5 V versus RHE).

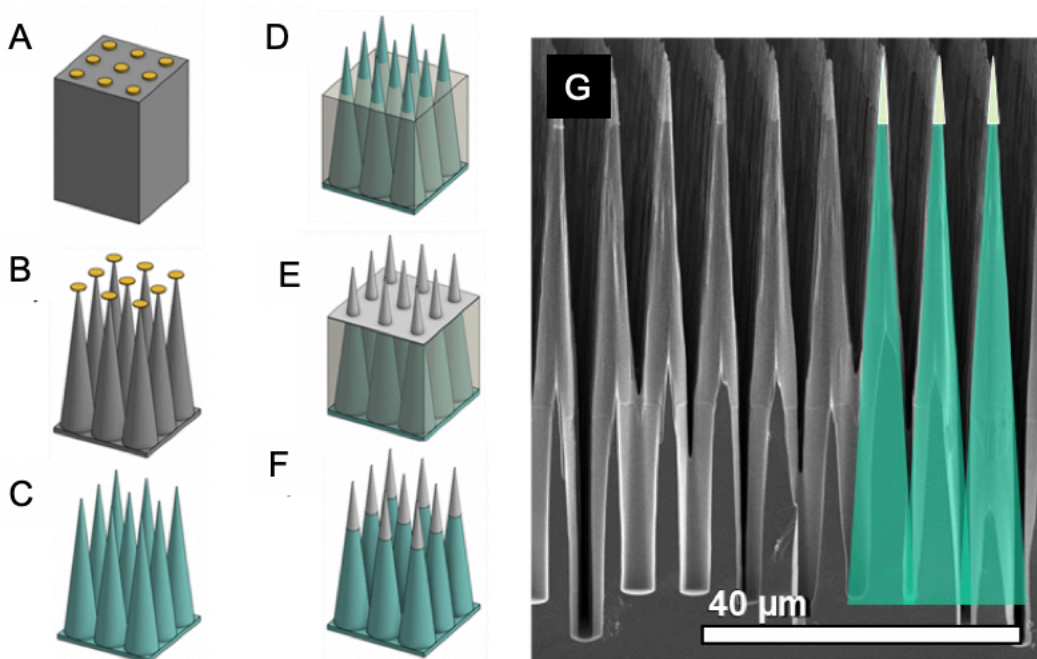


Figure 4.1: (A-F) Schematic for the fabrication of n^+p -Si μ -cone array photocathodes with Pt selectively loaded on the tips of the μ -cones. (A) Aluminum oxide mask (yellow) patterned on p-type silicon (gray). (B) Controlled undercutting of the etch mask leads to high-aspect ratio cones. (C) Removal of the etch mask followed by formation of an n^+ -emitter layer (green) via phosphorus doping. (D) Infilling with wax (transparent gray) followed by directional O_2 etching to expose tips. (E) Uniform deposition of Pt via sputtering. (F) Removal of the wax with acetone leaves Pt only at the cone tips. (G) Scanning-electron micrograph of n^+p -Si μ -cone photocathodes with Pt selectively deposited on the tips of the μ -cones

The overpotential required for the HER decreased as Pt was added to the photocathodes. For the planar and μ -pyramid geometries, increasing the thickness of the Pt resulted in improvements to the fill factors (ff) of the J - E characteristic; however, increasing the thickness of the Pt catalyst beyond 2 nm resulted in reductions to $|J_{ph}|$ due to optical absorption and reflection losses associated with the Pt layer. For the planar and μ -pyramid geometries, $-J_{RHE}$ decreased to $< 10 \text{ mA cm}^{-2}$ when the thickness of the Pt layer

reached 8 nm or 16 nm, respectively. However, Si μ -cone array photocathodes with 8 nm of Pt yielded $-J_{\text{RHE}} = 33 \pm 2 \text{ mA cm}^{-2}$, only $\sim 6\%$ less than $-J_{\text{ph}} = 35.0 \text{ mA cm}^{-2}$ observed for bare $\text{n}^+\text{p-Si}$ μ -cone photocathode arrays (**Figure 4.2D**). For $\text{n}^+\text{p-Si/Pt}$ μ -cone array photocathodes with 8 nm of Pt, the voltage required to drive the HER at a rate corresponding to a current density of -10 mA cm^{-2} , V_{-10} , was -70 mV relative to the open-circuit potential (E_{oc}). Doubling the thickness of the Pt layer, from 8 nm to 16 nm, on the tips of the μ -cones resulted in a slight decrease in $-J_{\text{RHE}}$, to $31 \pm 3 \text{ mA cm}^{-2}$, but did not change V_{-10} . The addition of a titanium adhesion layer between the Si and Pt did not change V_{oc} or V_{-10} and did not produce a decrease in $|J_{\text{ph}}|$ relative to the bare $\text{n}^+\text{p-Si}$ μ -cone array.

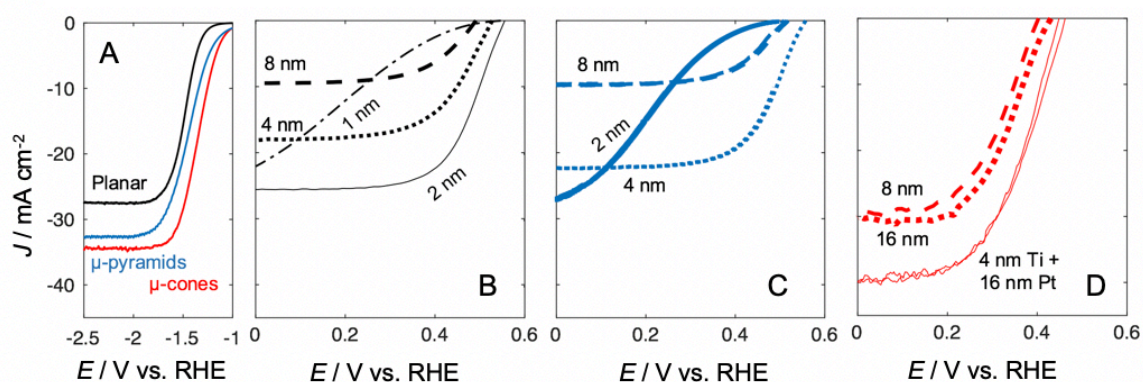


Figure 4.2: Effect of Pt loading on the J - E behavior of $\text{n}^+\text{p-Si}$ photocathodes with planar (black traces), μ -pyramid (blue traces), and μ -cone array (red traces) morphologies, as measured in contact with H_2 -saturated $0.50 \text{ M H}_2\text{SO}_4(\text{aq})$ while illuminated by 100 mW cm^{-2} of simulated Air Mass (AM) 1.5 illumination. (A) J - E behavior of bare (no Pt) $\text{n}^+\text{p-Si}$ photocathodes. Representative J - E behavior for $\text{n}^+\text{p-Si/Pt}$ photocathodes with varied Pt loadings for the (B) planar, (C) μ -pyramid, and (D) μ -cone morphologies.

This behavior indicated that either increased reflection into the internal volume of the array, or reduced parasitic absorption due to increased continuity of the film, reduced the optical losses in the catalyst layer. The values of $-V_{-10}$ for planar Si and μ -pyramidal Si

photocathodes, 87 mV and 80 mV respectively, were slightly higher than those observed for Si μ -cone arrays with at least 8 nm of Pt, despite complete coverage of the Si surface with 4 nm of Pt. Further increases to the thickness of the Pt, to 8 nm on planar Si, and to 16 nm on μ -pyramidal arrays, led to improved ff but resulted in $-J_{ph} < 10 \text{ mA cm}^{-2}$. Despite the Pt catalyst covering just $\sim 2\%$ of the total surface area of the Si μ -cone array photocathode, the μ -cone geometry maintained a relatively low overpotential while simultaneously exhibiting a value of $-J_{ph}$ that was higher than the values exhibited by bare planar or random μ -pyramidal textured Si photocathodes.

The ideal regenerative cell efficiency (η_{IRC}) represents the efficiency of a photoelectrode operating in conjunction with a nonpolarizable counter electrode performing the reverse reaction of interest, and was used as a metric to compare the performance of various different photocathodes.¹¹⁵ The η_{IRC} for n^+p -Si/Pt μ -cone photocathodes with 8 nm of Pt was $5.8 \pm 1.1 \%$, with a best-performing device yielding $\eta_{IRC} = 6.9\%$. The η_{IRC} for n^+p -Si/Pt μ -cone photocathodes with 16 nm Pt and 4 nm of titanium was $6.7 \pm 2.4 \%$, with a best-performing device yielding $\eta_{IRC} = 9.8\%$. The use of an n^+p -Si homojunction with 8 nm, 16 nm of Pt, or a Ti/Pt stack on Si μ -cones resulted in an open-circuit potential (E_{oc}) of $416 \pm 15 \text{ mV}$, $402 \pm 22 \text{ mV}$, and $416 \pm 60 \text{ mV}$ respectively, vs RHE, and yielded light-limited photocurrent densities at potentials $> 0 \text{ V}$ vs RHE. The E_{oc} values for the best-performing device were 431 mV for 8 nm Pt films and were 442 mV for 16 nm Pt films. Thus the open-circuit voltage was insensitive to the thickness of the catalyst layer but greater $|J_{ph}|$ was obtained with the inclusion of a Ti adhesion layer separating the Si/Pt interface. The primary difference between the

performance of best-performing devices and average devices thus arose from the higher photovoltages of best-performing devices relative to average photocathodes.

The planar and μ -pyramid Si photocathodes showed higher photovoltages than the μ -cone photocathodes (**Figure 4.2**), even though all of the photocathodes were diffusion doped by a nominally identical process (**A.4**). SEM images indicated that the Si μ -cone arrays had an ~ 12.5 -fold increase in junction area compared to a planar Si electrode, leading to an expected decrease in E_{oc} of ~ 65 mV assuming a diode quality factor of 1.0.¹¹⁶⁻¹¹⁷ Diffusion-doped, etched Si μ -wire based photocathodes for HER have been reported to exhibit E_{oc} up to 480 mV.¹⁰⁴ The observed E_{oc} of 440 mV for the highest-efficiency photocathodes thus suggests that more voltage was being lost than expected from the increase in surface area. The three-dimensional diffusion of P atoms is likely to preferentially dope the tips of the microcones, which could further enhance the recombination and thus lower the photovoltage.¹¹⁸ Hence, optimization of the doping process at the tips of the microcones could potentially improve the photovoltage of similar devices.

When Pt was deposited to a thickness >4 nm, n^+p -Si/Pt photocathodes were stable under air exposure for a few days between fabrication and testing. These electrodes also reversibly passed anodic current, indicating that the Pt layer protected the Si from forming an insulating interfacial oxide layer. Even though the catalytic overpotential was not changed by increasing the thickness of Pt beyond 4 nm for n^+p -Si/Pt photocathodes with planar or μ -pyramid geometries, the increased thickness of the Pt layer thus beneficially improved the stability of these electrodes. The increased Pt thickness needed for stability decreased the amount of light transmitted into the Si and limited the photocurrent densities

obtainable from n⁺p-Si/Pt planar and μ-pyramid photocathodes. In contrast, little or no loss of J_{ph} or ff accompanied the increase in Pt thickness (16 nm) required for stable performance of the n⁺p-Si/Pt μ-cone array photocathodes. Extended testing of n⁺p-Si/Pt μ-cone array photocathodes was performed using chronopotentiometry at -10 mA cm⁻². The potential of the photocathode drifted negative with time while E_{oc} remained relatively constant, indicating an increase in V_{-10} at the catalyst. The losses in photocurrent onset could be reversed by cleaning the photoelectrode in concentrated HCl/HNO₃ followed by deionized H₂O (A.4).

4.3.2 Si photocathodes with electrodeposited Co-P catalyst

Co-P, an earth abundant, active HER electrocatalyst, was used to explore the compatibility of Si μ-cone arrays with catalysts other than noble metals such as Pt. Additionally, on p-type Si, Co-P produces a photovoltage in the absence of a homojunction,⁴² providing the opportunity to compare the behavior of systems that have an emitter, in n⁺-p structures, with photocathodes that instead primarily rely on minority-carrier collection in the light absorber to determine the spatial location of interfacial photocurrent collection at the solid/catalyst/liquid interface. To fabricate such photocathodes, Co/Co-P was electrodeposited onto Si μ-cones using a narrow-band light-emitting diode with an intensity-averaged wavelength of 625 nm, until a charge density of 400 mC cm⁻² was passed. The bare p-Si μ-cone arrays predominantly absorbed light at 625 nm at the tips of the μ-cones.⁴³ Due to deposition at mass-transport-limited current densities, photoelectrodeposition of the Co/Co-P film occurred preferentially at the tips of the Si μ-cones, producing clumps > 1 μm in diameter that shadowed the underlying array (Figure 4.3A). To obtain an active Co-P catalyst, excess Co was removed by extended

potential cycling in contact with 0.50 M H₂SO₄(aq) while under 100 mW cm⁻² of simulated AM1.5 solar illumination.⁴² Potential cycling resulted in a restructuring of the catalyst film into nanoscale islands that were located predominantly at the tips of the μ-cones (Figure 3b).

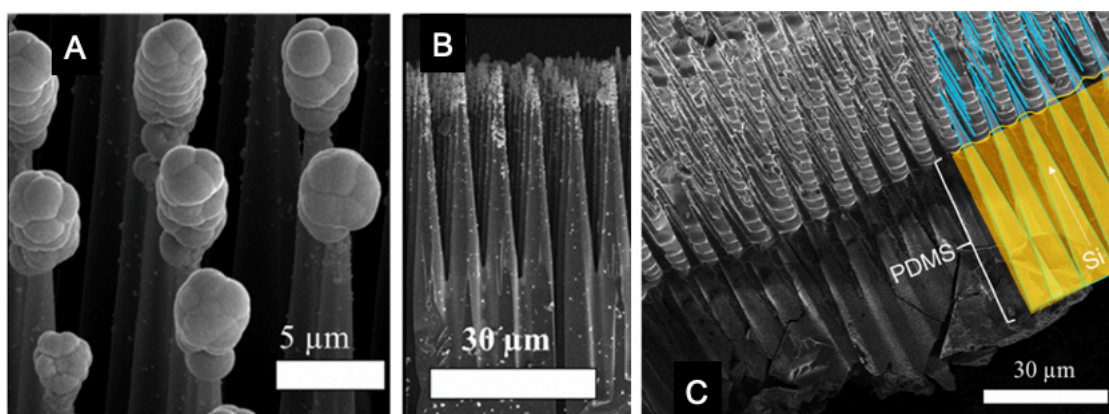


Figure 4.3: (A) Scanning-electron micrograph (SEM) of as-deposited Co/Co-P photoelectrodeposited onto the tips of p-Si μ-cones. The Co/Co-P loading, as determined by the charge density passed during the photoelectrodeposition, was 400 mC cm⁻². (B) SEM image of a cross section of a p-Si/Co-P μ-cone array after removal of excess Co by potential cycling in 0.50 M H₂SO₄(aq). (C) SEM of polymer embedded Si μ-cones removed from substrate, after deposition of Co-P and potential cycling in 0.50 M H₂SO₄(aq).

Figure 4.4 shows the J - E behavior of an illuminated bare p-Si μ-cone array photocathode, as well as the evolution of the J - E behavior of a p-Si/Co-P μ-cone array photocathode operated in contact with 0.50 M H₂SO₄(aq). Both J_{ph} and E_{oc} of the p-Si/Co-P μ-cone array photocathode improved with cycling and began to stabilize after ~ 16 voltammetric J - E cycles. Deposition of Co-P on planar, μ-pyramid, or μ-wire Si photocathodes yielded $-J_{ph}$ of 15 mA cm⁻², 20 mA cm⁻², and 25 mA cm⁻² respectively⁴², whereas p-type Si μ-cone/Co-P photocathodes exhibited $-J_{ph} = 32 \pm 2$ mA cm⁻². Compared

to bare p-type Si μ -cone array photocathodes, the deposition of Co-P on the Si μ -cone tips resulted in an average decrease in $-J_{\text{ph}}$ of 3 mA cm^{-2} . Si μ -cone array photocathodes exhibited $-J_{\text{RHE}} = 29 \pm 2 \text{ mA cm}^{-2}$ compared to $-J_{\text{RHE}} = 13 \text{ mA cm}^{-2}$, 18 mA cm^{-2} , and 22 mA cm^{-2} from planar, μ -pyramidal, and μ -wire array Si photocathodes, respectively,⁴² demonstrating the beneficial light trapping properties of the Si μ -cone morphology when coupled with the Co-P HER catalyst.

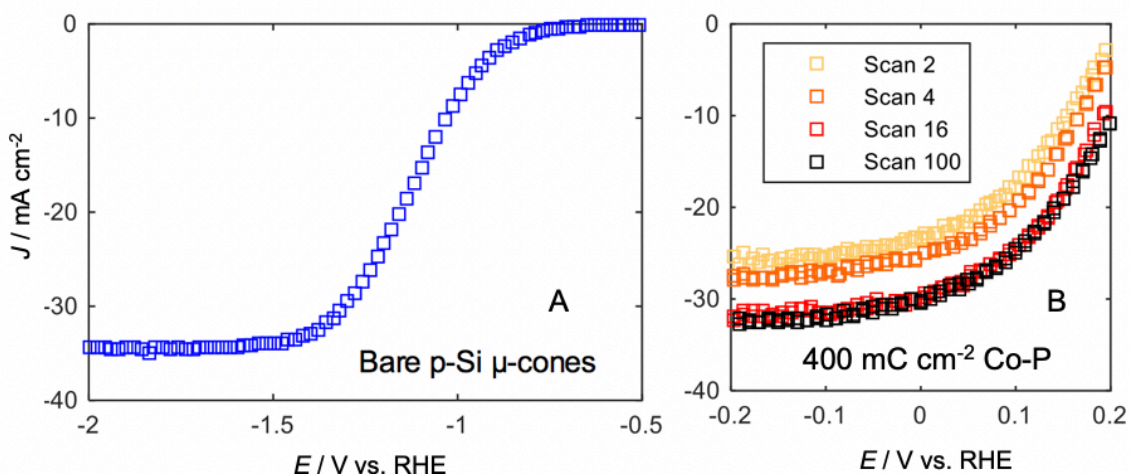


Figure 4.4: J - E behavior of p-Si μ -cone array photocathodes immersed in H_2 -saturated $0.50 \text{ M H}_2\text{SO}_4(\text{aq})$, illuminated with 100 mW cm^{-2} of simulated AM1.5 illumination, and with rapid stirring. J - E behavior (A) prior to catalyst deposition and (B) after being loaded with Co/CoP after 2, 4, 16, and 100 scans from -0.376 V to $+0.224 \text{ V}$ vs RHE at 50 mV s^{-1} . The first and last scans were recorded after 20 s and 40 min, respectively.

The average E_{oc} for the p-Si/Co-P μ -cone array photocathodes was $331 \pm 50 \text{ mV}$ vs RHE, and the highest observed E_{oc} for the p-Si/Co-P μ -cone photocathodes was 384 mV vs RHE. The p-Si/Co-P μ -cone array photocathodes did not require a diffusion-doped homojunction but yielded lower E_{oc} values than the $\text{n}^+\text{p-Si/Pt}$ μ -cone array photoelectrodes. The p-Si/Co-P μ -cone array photocathodes reached a solar-to-fuel current density of -10 mA cm^{-2} at $+197 \pm 20 \text{ mV}$ vs RHE. The best-performing device exhibited this current

density at +220 mV versus RHE, with $\eta_{\text{IRC}} = 3.1\%$. Extended testing of p-Si/Co-P μ -cone array photocathodes at 0 V vs RHE showed that after the initial increase in $|J_{ph}|$ during the first 30 min of cycling, the optical properties of the device remained stable for 24 h (**Figure 4.5**). SEM images of electrodes before and after extended testing in 0.50 M H₂SO₄(aq) showed that the structure of the Si μ -cone array was unchanged whereas the Co-P catalyst layer had restructured from μ m-scale particles to nanoscale islands (**Figure 4.5**).

Figure 4.6A compares the reflectance in the wavelength range of 400 nm – 1100 nm for bare Si μ -cone array, a Si μ -cone array with 8 nm or 16 nm of Pt selectively deposited at the tips of the μ -cones, and a p-Si/Co-P μ -cone array electrode. No substantial change was observed in reflectance between n⁺p-Si μ -cone arrays with and without a Pt coating, indicating that the incident light that is typically reflected from planar or μ -pyramid Si surfaces was redirected into the Si substrate due to the conical geometry. Hence, the Si μ -cone arrays had superior light-trapping properties relative to the bare Si pyramid structures before and after deposition of the catalyst. This concept is similar to that observed previously in effectively transparent contacts for silicon solar cells.^{45, 119-120}

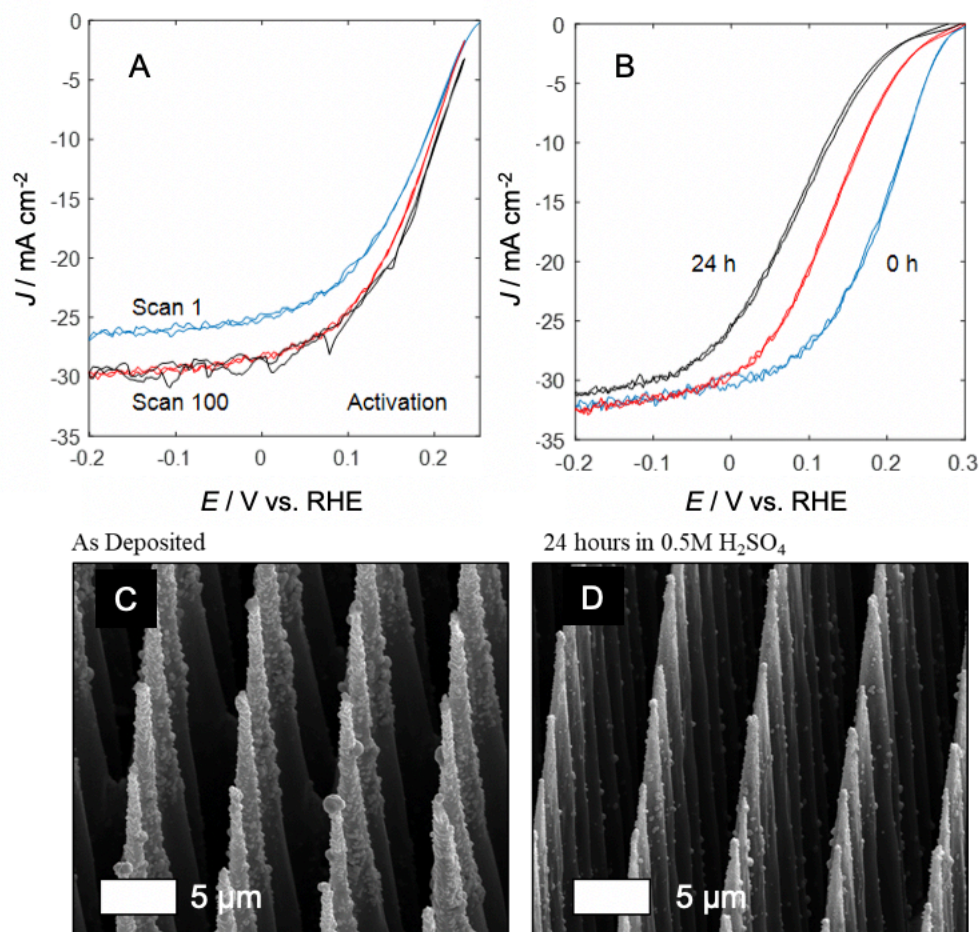


Figure 4.5: Extended photoelectrochemical testing of a p-Si/CoP μ -cone photocathode with 400 mC cm⁻² Co-P. **(A)** Current density vs potential behavior in H₂-saturated 0.50 M H₂SO₄(aq) under 100 mW cm⁻² of simulated AM1.5 illumination, with rapid stirring of the electrolyte for the 1st, 10th, and 100th cycle at 50 mV s⁻¹, blue, red, and black circles, respectively. The 100th scan occurred after 30 min of cycling. **(B)** Comparison of the J - E behavior over 24 h of continuous H₂(g) evolution at RHE under 1-Sun illumination for the device activated in (A). **(C-D)** Scanning-electron micrographs of the p-Si/CoP μ -cone photocathode with 400 mC cm⁻² Co-P before (C) and after (D) testing in 0.50 M H₂SO₄(aq) under 1-Sun illumination for 24 h. Scale bars represent 5 μ m at 0 degrees tilt.

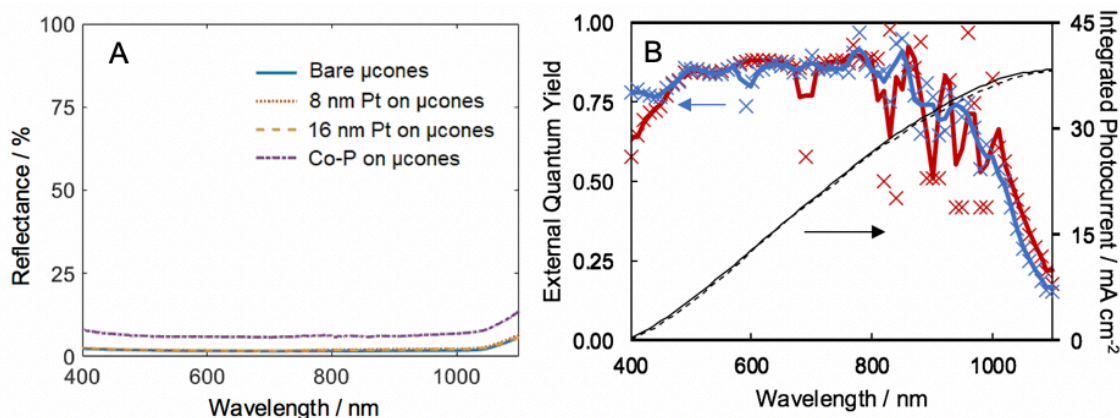


Figure 4.6: (A) Reflectance measurement of bare Si μ -cone arrays, Si μ -cone arrays with 8 and 16 nm of Pt or Co-P on their tips, as measured using a Cary 5000 UV-Vis-NIR with an integrating sphere. (B) Spectral response of a n^+p -Si/Pt μ -cone array at 0 V RHE (red) and p -Si μ -cone array in with 400 mC cm^{-2} Co-P at -200 mV vs RHE after activation in H_2 saturated $0.50 \text{ M H}_2\text{SO}_4$ for 30 min (blue). Individual data points were recorded every 10 nm, with a continuous line plotting the midpoint average for three data points. The maximum integrated photocurrent is plotted as a black line for a p -Si/Co-P μ -cone array (continuous) and n^+p -Si/Pt μ -cone array (dashed) from 400 nm to 1100 nm based on the photon density of the AM1.5 spectrum.

The reflectance of the p -Si/Co-P μ -cone array was 5% higher than the reflectance of the n^+p -Si/Pt μ -cone array because the Co-P islands were rough compared to the sputtered Pt coating, allowing relatively higher outward scattering of light from the Co-P islands on the tips of the μ -cones. Although the p -Si/Co-P μ -cones exhibited higher reflectance than the Pt-loaded μ -cones, the average J_{ph} was the same (-32 mA cm^{-2}) for p -Si/Co-P μ -cone arrays and n^+p -Si/Pt μ -cone arrays with 16 nm of Pt, indicating that in the 400 nm – 1100 nm wavelength range, 16 nm of Pt has a higher parasitic absorption than Co-P. Figure 5b compares the spectral response of an n^+p -Si/Ti/Pt μ -cone array to a p -Si/Co-P μ -cone array in $0.50 \text{ M H}_2\text{SO}_4(\text{aq})$ at 0 V and -0.2 V vs RHE, respectively. Both

photocathodes exhibited external quantum yields, defined as the fraction of photons collected as photocurrent, $\phi_{ext}(\lambda)$, in excess of 0.8 for wavelengths between 450-900 nm. The integrated photocurrent density for the AM1.5 spectrum was calculated via **Equation 4.1**:

$$J_{ph} = \frac{q}{hc} \int_{400 \text{ nm}}^{1100 \text{ nm}} \phi_{ext}(\lambda) \cdot P_{AM1.5}(\lambda) \cdot d\lambda \quad (4.1)$$

where $P_{AM1.5}(\lambda)$ is the power density per cm^2 of the AM1.5 spectrum at the specified wavelength. The predicted limiting photocurrent density under AM1.5 illumination was in excellent accord with the measured J_{ph} .

Bare p-type Si μ -cone arrays were also embedded in polydimethylsiloxane (PDMS), peeled off the substrate, and fabricated into electrodes by deposition of a Au back contact using electron-beam evaporation (see Methods for more detail). **Figure 4.3C** shows a SEM image of Si μ -cone arrays in PDMS with $\sim 15 \mu\text{m}$ of the tips exposed, with the freestanding, polymer-embedded μ -cones arrays decorated with Co-P using the same procedure as described for the on-substrate p-type Si μ -cones. Free-standing devices were tested as photocathodes in 0.50 M $\text{H}_2\text{SO}_4(\text{aq})$, to evaluate the performance of μ -cones in a membrane-embedded photocathode for $\text{H}_2(\text{g})$ generation. **Figure 4.7** presents representative J - E data in 0.50 M $\text{H}_2\text{SO}_4(\text{aq})$ under 100 mW cm^{-2} of simulated AM1.5 illumination. These devices exhibited $E_{oc} = 150 \pm 36 \text{ mV}$ and $J_{RHE} = -0.94 \pm 0.32 \text{ mA cm}^{-2}$, with a best-performing device exhibiting $J_{RHE} = -1.41 \text{ mA cm}^{-2}$. At -200 mV vs RHE, free-standing Si μ -cones exhibited an average $J_{ph} = -6.5 \text{ mA cm}^{-2}$, and the best-performing device exhibited $J_{ph} = -8.1 \text{ mA cm}^{-2}$ and remained active for 3 h of testing.

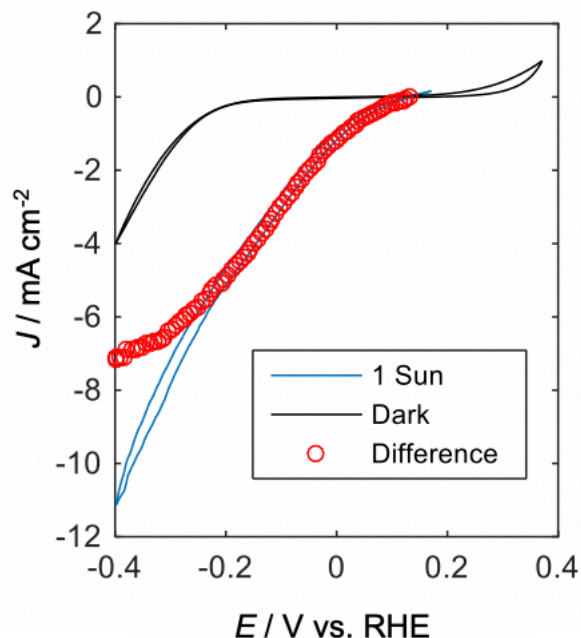


Figure 4.7: Representative J - E behavior of PDMS-embedded Si μ -cone array photocathodes decorated with Co-P and tested in 0.50 M $\text{H}_2\text{SO}_4(\text{aq})$ under 100 mW cm^{-2} of simulated AM1.5 illumination (blue). For comparison, the J - E behavior was recorded in the absence of illumination (black), and the difference between the two measured values was taken to be the photocurrent density for a given potential (red circle)

The photoactivity indicated that many of the individual p-type Si μ -cones were directly contacted with electrolyte during the Co-P catalyst deposition, and also while being tested as photocathodes. The absolute photocurrent density was higher than previous reports for Si μ -wires embedded in polymer membranes,^{31, 39, 121} but lower than the photocurrent density for Si μ -cones on a substrate. Incomplete contact between the Au back contact and individual Si μ -cones may be responsible for the reduced photon collection of the free-standing array fabricated for proof-of-concept purposes in this work. Further optimization of the placement of the catalysts, in order to more optimally match local carrier generation rate, could be achieved using light-guided deposition of catalysts.¹²²

The p-Si μ -cone/Co-P photocathodes do not require formation of a homojunction or emitter layer. Use of surface passivation and/or a homojunction or amorphous silicon heterojunction on the Si μ -cone arrays could thus improve the efficiency by reducing surface recombination velocities while retaining the benefit of high light absorption in Si μ -cones. Si μ -cones with $< 100 \text{ cm s}^{-1}$ surface passivation can in principle produce $E_{oc} > 650 \text{ mV}$,^{43, 101} and membrane-embedded μ -cones absorb $> 90\%$ of the light relative to their on-substrate counterpart. Polymer-embedded Si μ -cone arrays could thus produce $-J_{ph} > 25 \text{ mA cm}^{-2}$. Under standard conditions, HI splitting requires a minimum voltage of $\sim 0.53 \text{ V}$, so utilizing a highly active catalyst such as Pt for the HER, along with improving the current collection could lead to flexible membrane-embedded photocathodes for HI splitting potentially reaching $\eta_{IRC} > 10\%$.

Microcone array photoelectrodes can principle be fabricated in a scalable manner over large areas either by controlled electrochemical etching and/or by transferring the microcone arrays into peeled polymer films with subsequent re-use of the patterned growth substrate (**Scheme 4.1**).¹²³ The approach of structuring a photoelectrode, in which both the absorber and electrocatalyst are in the illumination path, into microcone arrays provides a general strategy for optimization of light absorption in the photoelectrode without producing obscuration by high mass loadings of optically absorbing and/or reflecting electrocatalyst films often required for the low-overpotential production of fuel and/or for efficient water oxidation to $\text{O}_2(\text{g})$. Photoelectrodes utilizing Si μ -cones could additionally be implemented as a tandem junction to produce photovoltages necessary for water-splitting, with a wider band gap material deposited on the surface of the cones, in a similar fashion to previous studies that used a core-shell design on Si microwire arrays (**Scheme**

4.1).¹²⁴⁻¹²⁵ In a core-shell tandem device, both semiconductors and one of two electrocatalysts would be on the sunlight-facing side of the membrane. Mesoscale metal films avoid parasitic absorption of photons due to resonant coupling,¹²⁰ thus Si μ -cone arrays are an advantageous scaffold for integrating wide band gap semiconductors in an architecture which can minimize reflection by the electrocatalyst in the illumination path.

Designs that utilize planar photoelectrodes integrated in a monolithic stack have consistently demonstrated the highest efficiencies for unassisted water splitting.^{21, 48, 126} In microstructured electrodes, losses due to the increased area available for recombination at the charge-separating junction lead to lower photovoltages in comparison to planar devices.¹⁰³ GaAs microcells that have been transfer printed following epitaxial growth onto devices that used separate surfaces for light absorption and catalysis exhibited high efficiencies when normalized to the active area of the photovoltaics.¹²⁷ Printed assemblies of high-efficiency photovoltaics, wired to catalysts that are outside the optical path of incident light, thus could be integrated with ion-exchange membranes to ensure long term, stable sunlight-driven water splitting. However, such devices will necessarily encounter losses in active area when integrating the electrocatalysts and ion conducting membranes necessary for efficient and safe operation, limiting the maximum achievable photocurrent density from such systems. The increased theoretical photocurrent density that could be obtained by appropriately integrated mesoscale-structured semiconductors, electrocatalysts, and ion-exchange membranes may be able offset the losses in photovoltage associated with structured semiconductors, motivating further study into such systems.

4.4 Conclusion

High photocurrent densities were exhibited by n^+p -Si/Pt and p -Si/Co-P μ -cone array photocathodes when either Pt or Co-P hydrogen-evolution catalysts were deposited on the tips of the μ -cones. n^+p -Si/Pt μ -cone array photocathodes yielded an average η_{IRC} of 5.7% at the maximum power point, and best-performing n^+p -Si/Ti/Pt μ -cone devices yielded $\eta_{\text{IRC}} = 9.8\%$. Thick (~ 16 nm) Pt and Co-P deposited onto Si μ -cone arrays produced only a 6% reduction in photocurrent density compared to bare photocathodes having the same morphology and microstructure. However, the Si μ -cone arrays exhibited photovoltages that were lower in magnitude by > 100 mV than the photovoltages obtained on planar or μ -pyramidally textured Si photocathodes. The photovoltage of the Si μ -cone arrays may be improved by optimizing the homojunction doping distribution. Greater than 90% of the incident light is absorbed in the μ -cones, as opposed to by the p -Si substrate at the base of the μ -cones,^{43, 101} so removal of the μ -cones from the substrate will result in confinement of light in an effectively thin silicon absorber layer, facilitating that higher photovoltages from the μ -cone arrays provided that surface recombination can be minimized.¹¹⁹ The p -Si/Co-P devices showed an average open-circuit voltage of 331 mV vs RHE without an emitter, which in combination with $J_{\text{ph}} = -32$ mA cm⁻² resulted in $\eta_{\text{IRC}} = 3.1\%$. Substantial improvements to the photovoltage obtained at the Si/Co-P junction will be required for such μ -cone arrays to be used as a practical photocathode in a tandem device. As a proof of concept, Si μ -cone arrays were also embedded in a flexible polymeric membrane, allowing for high catalyst loadings with minimal losses in photocurrent due to catalyst obscuration, and operation in a form factor which could facilitate integration into a tandem device for unassisted sunlight-driven water splitting.

Chapter 5

SPONTANEOUS FORMATION OF >90% OPTICALLY TRANSMISSIVE, ELECTROCHEMICALLY ACTIVE COP FILMS FOR PHOTOELECTROCHEMICAL HYDROGEN EVOLUTION

Kempler, P. A., Fu, H. J., Ifkovits, Z. P., Papadantonakis, K. M., & Lewis, N. S. (2020). Spontaneous Formation of > 90% Optically Transmissive, Electrochemically Active CoP Films for Photoelectrochemical Hydrogen Evolution. *The Journal of Physical Chemistry Letters*. 11(1), 14-20. <https://doi.org/10.1021/acs.jpcllett.9b02926>

5.1 Introduction

Transparent metal films with an open micro- or nano-structure have been prepared from precious metals such as Pt, Pd, Re, and Rh by controlled deposition or by etching in acidic electrolytes. Such Pt and Rh films have been integrated as catalysts into efficient and stable devices for photoelectrochemical hydrogen evolution.^{46, 48, 128} Pt films on p-InP photocathodes have been reported to exhibit substantial optical transparency for 20 h in 4.0 M HClO₄(aq).¹²⁹

The optical properties of nanostructured metal films are strong functions of the volume fraction and orientation of voids within the film, but are relatively insensitive to the nature of the host metal.¹³⁰ Hence, similar optical properties should be observable in films composed of a wide range of metals and HER electrocatalysts, including transition-

metal phosphides, a class of materials that is capable of driving HER current densities of $\sim 10 \text{ mA cm}^{-2}$ at absolute overpotentials $< 100 \text{ mV}$ in acidic media.¹³¹⁻¹³³ Within the family of transition-metal phosphides, CoP exhibits one of the highest average turnover frequencies per surface site, due to its intermediate binding energy for molecular hydrogen.¹³⁴ High-surface-area, amorphous CoP films can be prepared at room temperature and atmospheric pressure via electrodeposition from baths containing CoCl_2 and H_2PO_2 salts, with the deposited film containing oxidized cobalt and phosphorous species that are converted under cathodic bias in acidic media to a material with near-zerovalent Co and reduced P.^{26, 61} Prior reports of integration of electrodeposited CoP films on planar p-Si and Cu_2O have focused on thick, discontinuous catalyst films whose performances are limited by a trade-off between optical losses and overpotential towards the HER.^{42, 135}

We report herein a method for preparing transparent CoP films on Si(100) and fluorine-doped tin oxide (FTO) substrates. The electrocatalytic and optical properties of the films were assessed via optical transmission measurements during continuous hydrogen evolution in $0.50 \text{ M H}_2\text{SO}_4(\text{aq})$ to approximate conditions relevant to a solar-to-hydrogen device. A two-parameter optical model for the transparent, electrocatalytic CoP films was developed using spectroscopic ellipsometry, and the model was validated by independent measurements of the film nanostructure.

5.2 Experimental Methods

A detailed experimental section is provided in the Appendix (A.5). Prior to the electrodeposition of Co, degenerately doped n-type Si(100) ($\text{n}^+\text{-Si}$) surfaces were metallized with 1 nm of Ti via RF sputtering to form an ohmic contact and adhesion layer

for the CoP film. Metallized Si wafers and cleaned fluorine-doped tin-oxide samples were pre-nucleated with 2.5 nm of Co via RF sputtering. Electrodeposition was performed galvanostatically at a cathodic current density of 20 mA cm^{-2} in a plating bath containing $0.20 \text{ M CoCl}_2(\text{aq})$ and $0.30 \text{ M NaPO}_2\text{H}_2(\text{aq})$ continuously purged with Ar.²⁶ The thickness of the CoP film was controlled by varying the deposition time. Films were activated via exposure to $0.50 \text{ M H}_2\text{SO}_4(\text{aq})$. The effects of the acidic environment on the optical properties of the film were characterized in situ under 1 atm of $\text{H}_2(\text{g})$ by transmission measurements during (photo)electrochemical hydrogen evolution. The effects of activation on the film nanostructure were characterized ex situ by scanning-electron microscopy (SEM), atomic-force microscopy (AFM), and spectroscopic ellipsometry, after rinsing the films with deionized H_2O and drying in $\text{N}_2(\text{g})$.

5.3 Results and Discussion

Figure 5.1A shows a representative SEM cross section of a CoP film that was electrodeposited onto $\text{n}^+\text{-Si}$ to a loading of 1200 mC cm^{-2} ($\text{n}^+\text{-Si}(100)/\text{Ti}/\text{CoP}(1200 \text{ mC cm}^{-2})$). Electrodeposition onto pre-nucleated, $\text{n}^+\text{-Si}(100)/\text{Ti}/\text{Co}$ surfaces led to lustrous films with uniform coverage. Exposure of the films to $0.50 \text{ M H}_2\text{SO}_4(\text{aq})$ led to the dissolution of Co, which was accompanied by the formation of small H_2 bubbles on the surface. **Figure 5.1B** shows a representative SEM cross section of the same film after 3 min of activation in $0.50 \text{ M H}_2\text{SO}_4(\text{aq})$. Crevices that extended vertically from the surface to the substrate were observed, while the total thickness of the film remaining essentially constant. Determination via inductively coupled plasma mass spectrometry, ICP-MS, of the dissolution products of as deposited CoP films in $0.50 \text{ M H}_2\text{SO}_4(\text{aq})$ under cathodic bias,

indicated that the majority of material removed was Co (**Figure 5.2**). The majority of cobalt corrosion occurred within the first 10 min of exposure to 0.50 M H₂SO₄(aq)

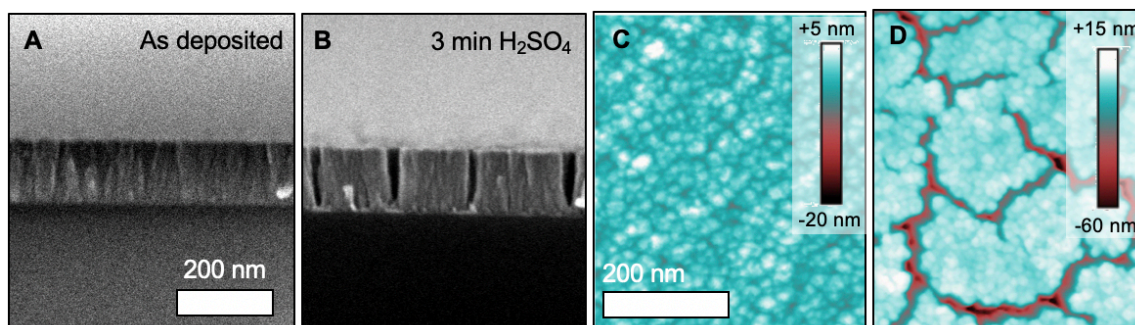


Figure 5.1: (A) SEM image of a cross section of a CoP film deposited onto n⁺-Si(100)/Ti/Co and (B) exposed to 0.50 M H₂SO₄(aq) for 3 min. (C-D) AFM images of an as-deposited n⁺-Si(100)/Ti/CoP surface recorded in tapping mode with a Si tip having a nominal radius of 2 nm and (D) after 3 min exposure to 0.50 M H₂SO₄(aq).

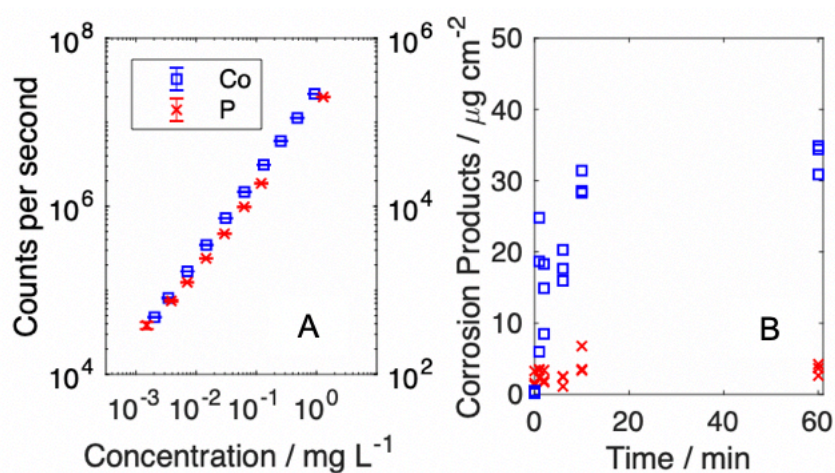


Figure 5.2: (A) Calibration of ICP-MS method from TraceCERT® standard solutions for P and Co prepared by serial dilution. (B) Corrosion products detected by ICP-MS for n⁺-Si(100)/Ti/CoP(800 mC cm⁻²) electrodes held at -10 mA cm⁻² in H₂ purged 0.50 M H₂SO₄.

Figure 5.1C shows an AFM image of an electrodeposited CoP film on an n⁺-Si(100)/Ti/Co surface after 40 s of electrodeposition. The mean surface roughness was 1.2 nm and the surface was composed of spherical grains that were 10-25 nm in diameter. Exposure of the film to 0.50 M H₂SO₄(aq) led to the formation of small crevices with a mean full width at half max (*FWHM*) of 6 ± 3 and a depth (*d*) of 11 ± 3 nm after 1 min of immersion, with these values increasing to *FWHM* = 13 ± 4 and *d* = 41 ± 15 nm after 3 min of exposure time (**Figure 5.1**). The formation of crevices led to a 50% increase in the nanoscale roughness, from 1.07 to 1.60 times the geometric area of the film. The areal density of crevices, measured as the total length per unit area, increased to $7.3 \mu\text{m}^{-1}$ after 60 s and remained essentially constant at 11.2 and $11.3 \mu\text{m}^{-1}$ after 120 s and 180 s of exposure time, respectively. The rate of change in crevice height relative to the rate of change in crevice width was 4 to 1.

Collective physical characterization indicates that the composition and structure of the as-deposited film was suitable for spontaneous formation of nanostructured catalyst films having feature sizes smaller than half the wavelength of visible light. Energy dispersive X-ray spectroscopy,⁴² X-ray photoelectron spectroscopy,²⁶ and X-ray absorption spectroscopy,⁶¹ of electrodeposited CoP have shown that that exposure of films to 0.50 M H₂SO₄(aq) leads to a reduction in the molar ratio of Co:P.^{26, 61} The predominance of Co in the corrosion products detected via ICP-MS is consistent with prior observations of a decrease in the Co:P ratio following acid exposure. During the first 10 minutes of exposure to electrolyte, phosphorus was detected as a minor product of corrosion, in insufficient amounts for quantification, and therefore phosphorus containing species are not the primary film components removed during activation.

Figure 5.3A shows a series of optical transmission spectra for a CoP film, as a function of time immersed in 0.50 M H₂SO₄(aq). The transmission of CoP films was characterized as a function of the applied electrochemical potential using transparent, conductive, FTO as a substrate. Immediately after immersion in 0.50 M H₂SO₄(aq), the films exhibited an optical transmittance ranging from 37% at 400 nm to 77% at 1000 nm. The weighted average transmittance, T_{avg} , was calculated from the individual fractional transmittance as a function of wavelength, weighted by the flux of photons at a given wavelength in the Air Mass (AM) 1.5 spectrum, and normalized to unity (**Equation 4.1**):

$$T_{avg} = \frac{1}{\int_{400}^{1100} \phi_{AM1.5}(\lambda) d\lambda} \int_{400 \text{ nm}}^{1100 \text{ nm}} \phi_{AM1.5}(\lambda) T(\lambda) d\lambda \quad (4.1)$$

$T(\lambda)$ represents the fractional transmittance and $\phi(\lambda)$ is the photon density per unit of wavelength in the solar spectrum. T_{avg} increased continuously with immersion time in the solution, from an initial value of $T_{avg} = 0.67$ to $T_{avg} = 0.85$ after 10 min at open circuit. Upon application of a cathodic current density of 10 mA cm⁻², relevant to photoelectrochemical H₂ evolution in unconcentrated sunlight, T_{avg} increased to 0.89 and remained stable for > 10 min of testing. At negative potentials for which cathodic current was observed, the transmittance increased by over 10% between $\lambda = 400$ and $\lambda = 450$ nm.

Irreversible changes in the optical properties of the CoP films correlated with the time scales observed for nanostructuring of the films. Application of a reducing bias produced improvements in the transmissivity that can be consistently ascribed to previously observed chemical changes in the film composition that occur under applied bias in 0.50 M H₂SO₄(aq), such as reduction of phosphorus and dissolution of cobalt oxide.⁶¹

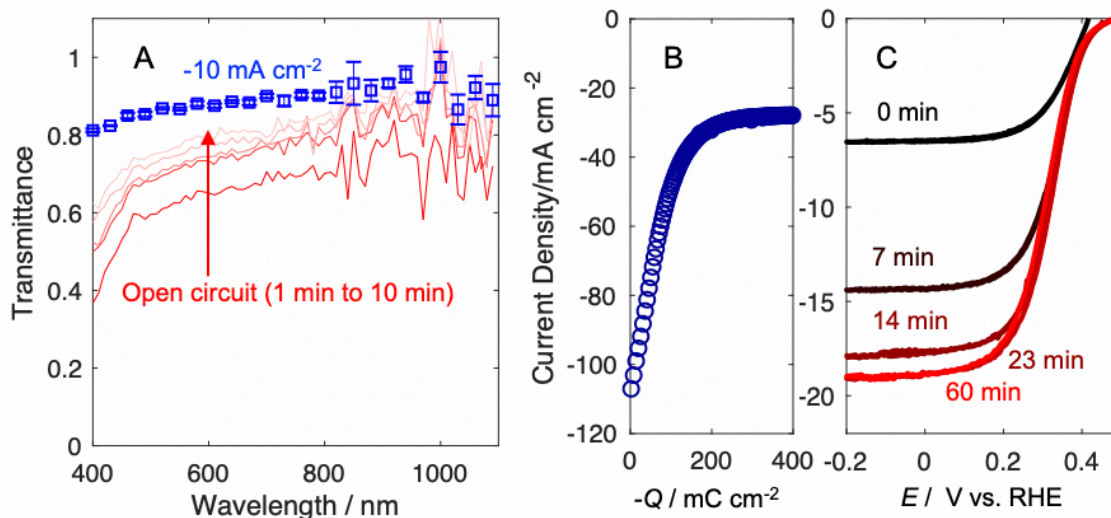


Figure 5.3: (A) In situ transmission versus wavelength measurements of a CoP film deposited to a charge density of 400 mC cm^{-2} onto an FTO/Co surface and immersed in $0.50 \text{ M H}_2\text{SO}_4(\text{aq})$. Red traces indicate transmission measurements collected sequentially at open circuit, while the blue data points represent the average transmission collected during 10 minutes of cathodic bias at -10 mA cm^{-2} (B) Photocurrent density vs. charge density, Q , passed for an $\text{n}^+\text{p-Si}(100)/\text{Ti}/\text{Co}$ electrode during deposition of CoP at -0.60 V versus a saturated calomel electrode under high-intensity 625 nm illumination from a narrow-band light-emitting diode. (C) J - E behavior as a function of time for an $\text{n}^+\text{p-Si}(100)/\text{Ti}/\text{Co}/\text{CoP}(400 \text{ mC cm}^{-2})$ electrode under 100 mW cm^{-2} of simulated Air Mass 1.5 illumination in $0.50 \text{ M H}_2\text{SO}_4(\text{aq})$ that was continuously purged with $\text{H}_2(\text{g})$. Scans were recorded at 50 mV s^{-1} and were separated by pauses at open circuit in the absence of illumination.

The optical properties of CoP were characterized on representative H_2 -evolving photocathodes using metallized $\text{n}^+\text{p-Si}(100)/\text{Ti}/\text{Co}$ samples as substrates. Crystalline Si exhibits long minority-carrier lifetimes, so the light-limited photocurrent density, J_{ph} , serves as a quantitative measure of the total amount of photons that pass through the catalyst film and are collected by the Si. **Figure 5.3B** shows the effect of charge passed during CoP deposition, Q , on the photocurrent density of an $\text{n}^+\text{p-Si}(100)/\text{Ti}/\text{Co}$ electrode.

Deposition of 400 mC cm^{-2} of CoP at light-limited photocurrent densities led to a decrease in $|J_{ph}|$ from 107 mA cm^{-2} to 28 mA cm^{-2} . **Figure 5.3C** shows the current density vs potential (J - E) response of an n^+p -Si(100)/Ti/CoP(400 mC cm^{-2}) electrode, under 100 mW cm^{-2} of simulated AM1.5 illumination in H_2 -saturated $0.50 \text{ M H}_2\text{SO}_4(\text{aq})$, as a function of the time spent in the acidic environment. Following pauses at open circuit in the absence of illumination, with successive scans $-J_{ph}$ increased from 6.6 mA cm^{-2} to 19.1 mA cm^{-2} . For 12 h, the current density at 0.0 V versus the reversible hydrogen electrode (RHE) remained within 12% of the maximum value (**Figure 5.4A**). The potential at a n^+ -Si(100)/Ti/CoP(800 mC cm^{-2}) in H_2 -saturated $0.50 \text{ M H}_2\text{SO}_4(\text{aq})$, held at -10 mA cm^{-2} in the absence of direct illumination, was observed to gradually decrease relative to RHE (**Figure 5.4B**).

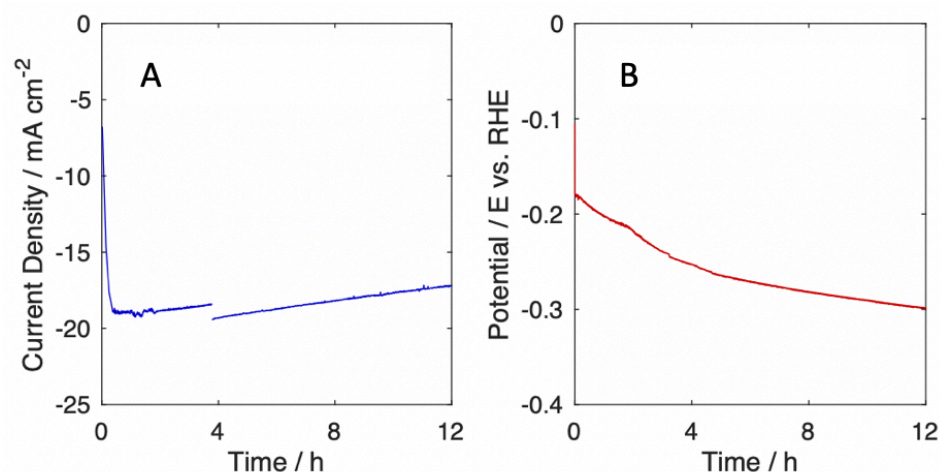


Figure 5.4: (A) Current density versus time behavior at 0 V vs the reversible hydrogen electrode (RHE) of an n^+p -Si(100)/Ti/CoP(400 mC cm^{-2}) photocathode under simulated 100 mW cm^{-2} AM1.5 illumination in $\text{H}_2(\text{g})$ -purged $0.50 \text{ M H}_2\text{SO}_4(\text{aq})$. (B) Potential versus time behavior at -10 mA cm^{-2} of an n^+ -Si(100)/Ti/CoP(800 mC cm^{-2}) electrode in $\text{H}_2(\text{g})$ -purged $0.50 \text{ M H}_2\text{SO}_4(\text{aq})$.

Measurements of the optical properties of the CoP films in 0.50 M H₂SO₄(aq) showed that transmission of visible and infrared light through the film increased during the formation of crevices within the film, and conversion of the as-deposited species to metallic Co and reduced P at negative potentials led to further increases in the optical transmission.⁶¹ The stability of photocurrents on a representative photocathode showed that the strategy of nanostructuring an otherwise opaque CoP film to achieve transmissivity does not necessarily lead to a substantial decrease in stability, because the stabilities of the electrodes observed herein were comparable to those reported previously for CoP in 0.50 M H₂SO₄(aq).^{26, 41} The performance of the transparent catalyst films in this work was compared to the performance of nominally identical n⁺p-Si(100)/Pt photocathodes (**Figure 5.5**).⁴⁴ The nanostructured CoP films in this work exhibited larger photocurrents than a n⁺p-Si(100) photocathode decorated with a 4 nm thick sputtered Pt film, indicating that the catalyst was more transmissive than the thin metal film despite being 10 times greater in thickness. However, the devices utilizing CoP as a catalyst reached a benchmark current density of -10 mA cm⁻² at potentials 150 mV more negative than the potentials required for state-of-the-art n⁺p-Si(100)/Pt photocathodes. Thus, the increased catalyst loading in the CoP devices was not sufficient to offset the increased activity of Pt towards hydrogen evolution in acid.

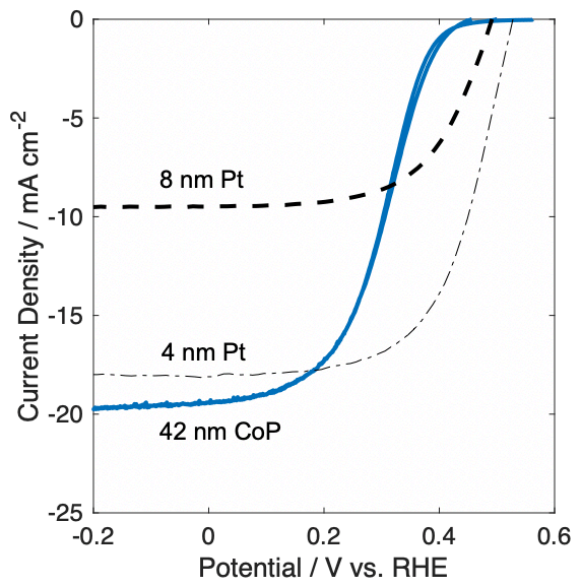


Figure 5.5: Comparison of the J - E behavior for an n^+p -Si(100)/Ti/Co/CoP(400 mC cm^{-2}) electrode under 100 mW cm^{-2} of simulated Air Mass 1.5 illumination in $0.50 \text{ M H}_2\text{SO}_4(\text{aq})$ to nominally identical n^+p -Si(100) electrodes decorated with 4 nm and 8 nm of Pt.

The effects of the dielectric properties and nanostructure of CoP films on the macroscopic optical properties were evaluated by use of spectroscopic ellipsometry. The dielectric function, $\tilde{\epsilon}$, is a complex function of wavelength that describes the average macroscopic response resulting from the individually polarizable components of the film.¹³⁶ Dielectric functions for the n^+ -Si(100)/Ti/CoP samples were calculated from the measured complex reflectance ratio using commercial software (WVASE®). The index of refraction, n , and extinction coefficient, k , of the as-deposited CoP films became increasingly insensitive to film thickness after $>800 \text{ mC cm}^{-2}$ of cathodic charge density had been passed. Relative to tabulated values for a Co film of comparable thickness,¹³⁷ the as-deposited CoP exhibited an increased n and decreased k from $\lambda = 400\text{-}1100 \text{ nm}$ (A.5.1). **Figure 5.6A** and **Figure 5.6B** present the real and imaginary components of $\tilde{\epsilon}$, ϵ_1 and ϵ_2 , respectively, for a CoP film deposited to a charge density of 800 mC cm^{-2} before and after

exposure to 0.50 M H₂SO₄(aq). Measurements of the dielectric functions for catalyst films with variable thicknesses are presented in Appendix (A.5.2).

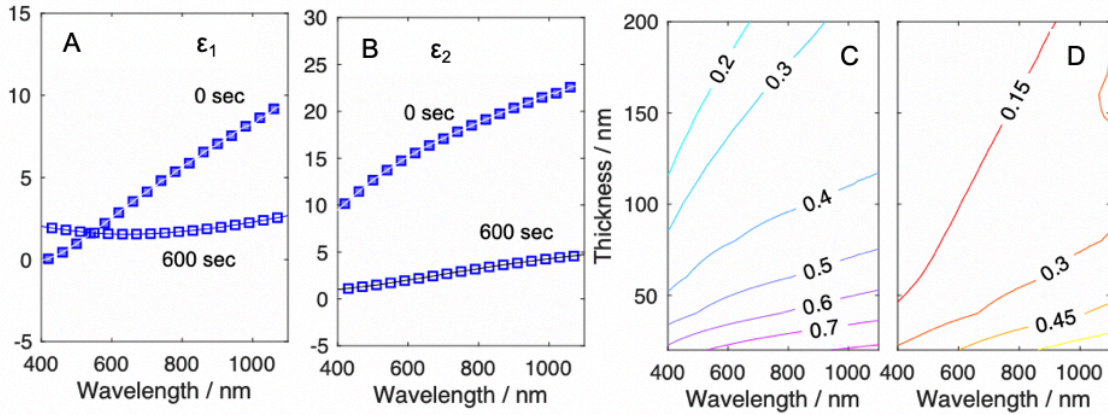


Figure 5.6: Spectroscopic ellipsometry of n⁺-Si(100)/Ti/Co/CoP deposited to a charge density of 800 mC cm⁻². Measured data points are shown as individual markers, and fits are represented as continuous lines. (A) Real and (B) imaginary components of the dielectric functions of as deposited CoP films (filled markers) and films activated after 600 seconds of activation in 0.50 M H₂SO₄(aq) (open markers). (C) Modeled transmittance isolines as a function of film thickness for an EMA layer with void inclusions, $f_m = 0.75$, and $q = 0.98$. (D) Modeled transmittance isolines as a function of film thickness for an EMA layer with metal inclusions, $f_m = 0.75$, and $q = 0.33$.

The optical properties of electrodeposited CoP films before and after activation in 0.50 M H₂SO₄(aq) were modeled using a Maxwell-Garnett effective medium approximation,¹³⁸ (Equation 5.2)

$$\tilde{\epsilon}_{eff} = \tilde{\epsilon}_m + \frac{f_v(\tilde{\epsilon}_v - \tilde{\epsilon}_m)\tilde{\epsilon}_m / [\tilde{\epsilon}_m + q(\tilde{\epsilon}_v - \tilde{\epsilon}_m)]}{1 - f_v(\tilde{\epsilon}_v - \tilde{\epsilon}_m)q / [\tilde{\epsilon}_m + q(\tilde{\epsilon}_v - \tilde{\epsilon}_m)]} \quad (5.2)$$

in which the thickness of individual layers and the tabulated dielectric constants of the metal and void domains were held constant while the void fraction, f_v , and depolarization factor, q , of the film nanostructure were allowed to vary (Figure 5.6A-B). The best fit for the series of data collected for an individual sample was obtained when the thickness of

the CoP layer was selected as a constant value. A depolarization factor > 0.9 led to fits that were in close agreement with the measured data, and the predicted void fractions and thicknesses were consistent with AFM and SEM measurements of the films both before and after 10 min of activation. At a loading of 800 mC cm^{-2} , the void fraction increased asymptotically to $24 \pm 2\%$, in close agreement with the $20 \pm 2\%$ fractional surface coverage of crevices measured by SEM (**Figure 5.7**).

Figure 5.6C-D compares the simulated spectral transmittances described by a Maxwell-Garnett effective medium approximation as a function of thickness for two different nanostructured CoP films. **Figure 5.6C** is a close approximation of the CoP films studied in this work, with a host metal layer that includes a void fraction of 0.25 with a depolarization factor of 0.98. The transmittance fraction was roughly double the void fraction at a film thickness of 50 nm, and was larger than the void fraction for thicknesses up to 150 nm. **Figure 5.6D** presents the results obtained for discontinuous matrix of metallic spheres in a void ambient, represented by a characteristic depolarization factor of 0.33 and a metal fraction of 0.75. As q approaches 1, transmittances larger than values expected from a film composed of discontinuous catalyst particles are obtained. The case where $q = 1$ is consistent with a nanostructure having inclusions described by laminar, flat plates oriented normal to the direction of the electric field of incident light, which is consistent with the observed film nanostructure in which flat mesas were separated by narrow, vertical sidewalls. **Table 5.1** compares the experimental and fitted optical parameters of films in this work with previously reported transparent metal catalysts films. CoP films in this work were represented by metal layers with disc-like void inclusions, in contrast to the void layers with spherical metal inclusions obtained for Pt, Pd, Rh, and Re;

comparable or greater transmission coefficients were obtained for CoP films with increased metal loadings at an equivalent film thickness to that of the noble metal films.^{46, 128} Collectively, the measured and simulated transmittance spectra showed that the nanostructured CoP films transmitted more light than an equivalent fractional coverage of fully opaque, microscale metal islands, and demonstrate that films of a similar nanostructure with thicknesses in excess of 100 nm can overcome a linear tradeoff between increased mass loading of catalyst and decreased optical transmittance.

Table 5.1: Comparison of optical properties of transparent metal films on planar semiconductors. The metal fraction, f_{metal} , and the depolarization factor, q , were modeled from ellipsometry data; measured and calculated transmittance, T_m and T_c , refer to the measured and calculated transmittance, respectively, under 700 nm illumination in an aqueous electrolyte.

Substrate	Material	Thickness	f_{metal}	q	T_m	T_c	Reference
InP	Rh	42 nm	0.49	0.45	0.65	0.35	(10)
InP	Pd	48 nm	0.32	0.32	0.67	0.47	(10)
InP	Re	60 nm	0.27	0.23	0.85	0.59	(10)
InP	Pt	33 nm	0.5	0.56	0.92 ^{a)}	-	(9)
Si	CoP	42 nm	0.74	0.98	0.90	0.80	This work
Si	CoP	97 nm	0.78	0.93	-	0.24	This work
Si	CoP	125 nm	0.70	0.92	-	0.17	This work

a) Data were measured for a 633 nm source.

The methods used to prepare transparent CoP films should be readily applicable to other electrodeposited metal phosphide films, containing Fe, Ni, Mo, or W.¹³⁹ Increasing

the anisotropy of material removal, thereby increasing q , could lead to higher transmittances being obtained from such films. The insensitivity of the transmittance to film thickness, for film geometries in which the depolarization factor approaches unity, allows for higher mass loadings to be implemented in practice on the light-absorbing surface(s) of a photoelectrochemical device. Nanostructured metal phosphides could be prepared via activation in 0.50 M $\text{H}_2\text{SO}_4(\text{aq})$ and then implemented in device designed for operation in basic electrolyte. Metal phosphides have been reported as HER catalysts at $\text{pH} > 13$, although detailed characterization of crystalline Co_2P in 1.0 M $\text{KOH}(\text{aq})$ revealed a surface conversion of the phosphide to $\text{Co}(\text{OH})_2$ after electrochemical cycling. Additionally, metal phosphides have been used as precursor species for efficient oxygen-evolution catalysts in 1.0 M $\text{KOH}(\text{aq})$ following conversion of the metal phosphide species to the corresponding metal oxide.¹⁴⁰⁻¹⁴¹

Nanostructuring strategies that allow for increased mass loadings of catalyst to be utilized in photoelectrochemical devices could allow for the use of kinetically stable catalysts. Steady dissolution rates on the order of $0.4 \text{ pg s}^{-1} \text{ cm}^{-2}$ would be required to stabilize a 100 nm thick catalyst film for 10 years of operation, assuming that open-circuit corrosion cannot be eliminated (details on this calculation are provided in the Appendix **A.5**). Systematic studies of the corrosion of earth-abundant Co_2P , Ni_5P_4 , and MoS_2 HER catalysts have revealed peak metal corrosion rates of $\sim 1 \text{ ng s}^{-1} \text{ cm}^{-2}$ at open circuit in $\text{H}_2(\text{g})$ -saturated 0.10 M $\text{HClO}_4(\text{aq})$.²⁷ In this work, electrodeposited CoP in 0.50 M $\text{H}_2\text{SO}_4(\text{aq})$ under cathodic bias and following an initial substantial loss in Co exhibited corrosion rates comparable to those measured for crystalline Co_2P in 0.10 M $\text{HClO}_4(\text{aq})$.²⁷ The asymptotic corrosion rate of Co on $n^+\text{-Si}(100)/\text{Ti}/\text{CoP}$, along with the gradual increase in the

overpotential required to drive -10 mA cm^{-2} towards the HER, are consistent with previously reported chronoamperometric behavior for electrodeposited CoP films on metallic Cu.²⁶ These data are incompatible with failure mechanisms involving dissolution of catalyst or continued formation of interfacial SiO_x but delamination or passivation of the catalyst layer could be responsible for the decline in device performance.

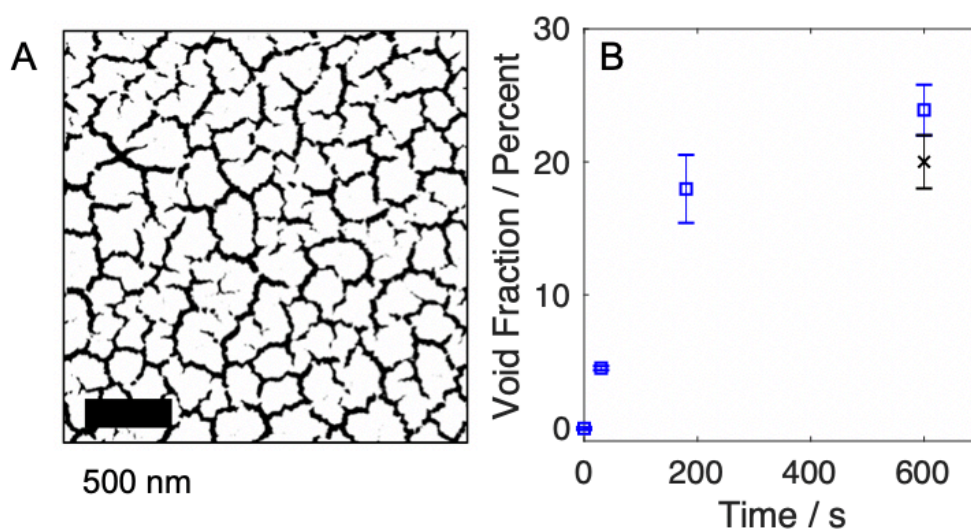


Figure 5.7: (A) Binary SEM image of a n^+ -Si(100)/Ti/CoP(800 mC cm^{-2}) electrode after 10 min of $0.50 \text{ M H}_2\text{SO}_4(\text{aq})$. The scale bar represents 500 nm. The secondary electrons collected while imaging provided elemental contrast, where lighter regions were assigned to CoP and darker regions to bare Si. The pixels were binned into catalyst and void regions so that the image could be used to estimate the void fraction. (B) Change in void fraction as a function of time for n^+ -Si(100)/Ti/CoP(800 mC cm^{-2}) electrodes, as measured by ellipsometry (blue squares) in comparison to SEM measurements (black x). Error bars represent one-standard deviation across three independent samples.

5.4 Conclusion

In summary, optically transmissive films of an earth-abundant CoP HER catalyst were prepared for use in hydrogen-evolving photocathodes. Spontaneous generation of an open nanostructure occurred in minutes in 0.50 M H₂SO₄(aq) via anisotropic removal of acid-instable catalyst precursors along pre-existing boundaries. The process led to an increase in the weighted average optical transmissivity from 0.67 to 0.89 on FTO substrates, and resulted in a three-fold increase in the light-limited photocurrent density at a representative Si photocathode effecting the HER. The nanostructure adopted by these films is suitable for the increased catalyst loadings required for practical use of metal phosphides and the technique should be readily generalizable to other electrodeposited catalyst films that are deposited as a mixed composition of acid-stable and acid-instable species. Furthermore, this strategy could be used alone or in tandem with alternate light-management strategies to facilitate the use of earth-abundant catalysts on the light-incident side of a solar fuels device.

Chapter 6

EFFECTS OF BUBBLES ON THE ELECTROCHEMICAL BEHAVIOR OF HYDROGEN-EVOLVING SI MICROWIRE ARRAYS ORIENTED AGAINST GRAVITY

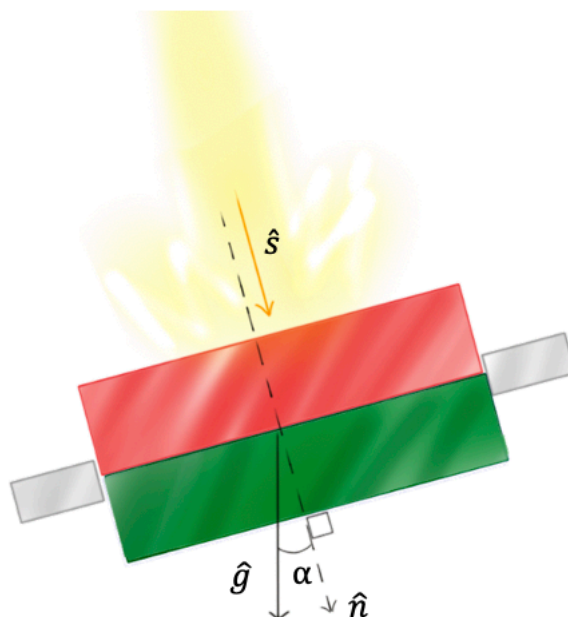
Kempler, P.A., Coridan, R.H., Lewis N.S. (2020). Effects of Bubbles on the Electrochemical Behavior of Hydrogen-Evolving Si Microwire Arrays Oriented Against Gravity. *Energy & Environmental Science*, 13, 1808-1817.

<https://doi.org/10.1039/D0EE00356E>

6.1 Introduction

Studies of the hydrogen-evolution reaction (HER) have provided a detailed understanding of the nucleation and growth behavior of individual H₂(g) bubbles.^{4, 16-18} Capillary forces at structured electrode surfaces provide a mechanism for reducing the adhesive force of gas bubbles. Moreover, “aerophobic” electrodes prepared from nanostructured metals and light absorbers effect a reduction in the diameter of departing bubbles due to increased wettability of the surface.¹⁹⁻²¹ Photoelectrochemical H₂ evolution from an InP photocathode modified with nanostructured Rh has been investigated in a microgravity environment,²² and under simulated sunlight yielded $|j_{H_2}| > 14 \text{ mA cm}^{-2}$ for 9 s in 1.0 M HClO₄ containing 1% (v/v) isopropyl alcohol. Si microwire, μW , array electrodes exhibit a low gas coverage during H₂ evolution due to the increased wettability of the surface relative to a planar Si electrode.²³ Tandem device designs evolving separate

streams of combustible gases require at least one downward-facing electrode, generating either H_2 or O_2 (**Scheme 6.1**), but the effects of electrochemical generation of gases at rates relevant to efficient solar fuels generation, while opposing gravity and without external forced convection, are not well understood. Vertically oriented Si μW arrays, having diameters approximately equal to the minority-carrier diffusion length and having heights large enough to be embedded in ion-conducting membranes, are a technologically-relevant model system for studies of gas evolution in integrated solar fuels generation systems.²⁴



Scheme 6.1: Monolithic, integrated tandem solar fuels device, with a wide band-gap semiconductor represented in red, a narrow band-gap semiconductor represented in green, embedded in a gray membrane for product separation. The orientation, α , is defined as the angle between the gravitational vector and the surface normal of the bottom side of the device. Optimal solar collection occurs when $\hat{n} \cdot \hat{s}$ approaches 1. The path of current-carrying charged species is represented as a dotted line.

We report herein the electrochemical behavior of representative planar and microwire-array cathodes prepared from n^+ -Si(100) surfaces metalized with a continuous layer of Pt, to understand how the geometry and orientation of these electrodes control the size-distribution and coverage of $H_2(g)$ bubbles. Moreover, the effects of H_2 evolution on the electrochemical behavior of the dark, downward-facing side of an integrated solar-driven water-splitting device, including effects on mass transport-limited current densities, the concentrations of dissolved H_2 near the electrode surface, and resistance drops at the cathode, have been elucidated through extensive measurements of bubble size distributions and coverages.

6.2 Experimental Methods

Fabrication of electrodes: Microstructured Si substrates were prepared as described in the Appendix (A.1). Metallization was performed in an Orion Series Sputtering system (AJA) at a base pressure of 10^{-7} torr. Ti and Pt films were sputtered sequentially in a 5 mtorr Ar plasma at a deposition rate of ~ 1 nm min^{-1} and ~ 2.6 nm min^{-1} , respectively. An ohmic back contact was made to the rear side of the Si with an In-Ga eutectic (Alfa Aesar), and the electrode was affixed to a Cu-Sn wire via conductive Ag epoxy (Ted Pella). The electrode was sealed into a piece of 6 mm diameter borosilicate glass tubing using a chemically resistant epoxy (Hysol 9460) that was cured for >12 h at room temperature. The electrode area was measured using a commercial optical scanner.

Electrochemical measurements: HER characteristics were evaluated in a 4-port electrochemical cell that contained an optical flat at the base of the cell to facilitate viewing of the electrode. Degenerately doped n^+ -Si electrodes were used to eliminate the effects of a photoactive substrate and to evaluate the performance under conditions experienced by a

downward-facing, dark electrode, where gas coverage does not affect light absorption. The electrolyte was 0.50 M H₂SO₄(aq) (TraceMetal Grade, Fisher) that was purged with H₂(g) for at least 30 min prior to testing, and was purged between experiments to maintain H₂(aq) in equilibrium with H₂(g) at 1 atm. A saturated calomel electrode served as the reference electrode and a Pt mesh electrode behind a Nafion (Dupont) membrane served as the counter electrode. A constant current or potential was obtained using a Biologic SP-200 potentiostat. The cell was mounted on a leveled surface and the electrode orientation was varied by tilting the electrochemical cell to match the angle defined by custom shims.

Macroscopic video collection and analysis: The gas coverage and the size distribution of bubbles were analyzed from video acquired at 60 frames s⁻¹, at a pixel width of 300 μm, using a commercially available high-definition camera mounted on optical posts (Thorlabs). Videos were recorded under illumination provided by a filtered Hg (Xe) lamp. Images were processed in MATLAB. Image thresholding was used to estimate the fractional gas coverage, θ , with black pixels representing the electrode and white pixels representing regions covered by gas bubbles. Bubble size distributions were measured as circles detected within individual images processed via a Hough transform of the grayscale image. Statistics were acquired after at least 2 min of continuous H₂ evolution to allow the behavior of the electrode to stabilize. Large bubbles could not be automatically detected and were therefore measured manually. Bubbles with diameters < 300 μm (~10 pixels) were omitted from macroscale measurements.

Microscopic video collection and analysis: High-speed microscopy experiments were performed in 0.50 M H₂SO₄ (aq) in an HDPE electrochemical cell with a glass cover. The imaging system consisted of a microscope (Olympus BX-53) with a 5x objective, an LED

reflectance illuminator (Prior Scientific), and a high-speed camera (Fastec Imaging). All imaging experiments were performed at 200 frames per second. Bubble radii were measured through extended image sequences using routines developed from the SciPy and Scikit-Learn libraries for the Python programming language.

6.3 Results

Figure 6.1 presents scanning-electron micrographs of n^+ -Si microwire arrays after metallization with Ti/Pt. Deep reactive-ion etching of patterned n^+ -Si(100) surfaces produced μW arrays over cm^2 areas with the microwires highly uniform in diameter, pitch, and height. Deposition of Pt by sputtering did not substantially modify the geometry or surface roughness of the array. Arrays were etched to a height of 30 μm , and three array geometries: (as defined by the photolithographic mask and etching time; 6 μm diameter and 14 μm center-to-center pitch, μW 6|14; 6 μm diameter and 28 μm pitch, μW 6|28; and 3 μm diameter and 11 μm pitch, μW 3|11) were prepared to investigate the electrochemical effects of variation in microwire spacing and diameter. The diameters and pitches of the arrays were measured via scanning electron microscopy of representative cross sections of the array and were consistent with the predicted dimensions.

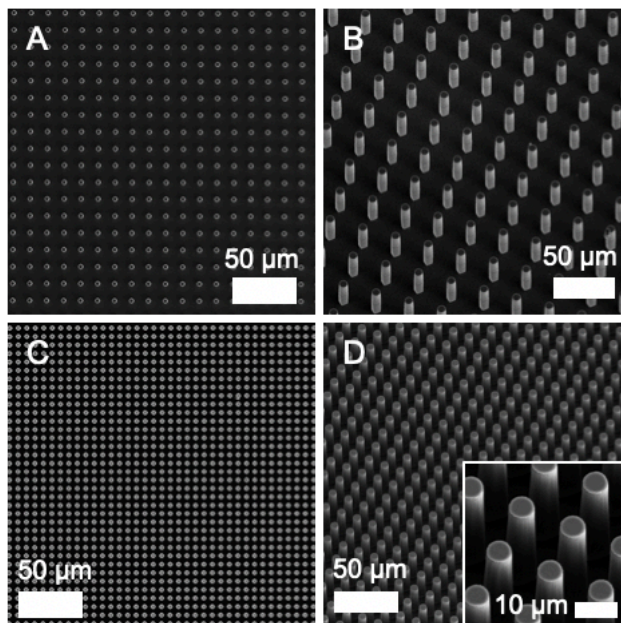


Figure 6.1: Scanning electron microscope images of platinized n^+ -Si(100) microwire arrays of nominal diameter $6\ \mu\text{m}$, height $30\ \mu\text{m}$, and pitch $28\ \mu\text{m}$ (A,B) and $14\ \mu\text{m}$ (C,D). Images acquired at normal incidence (A,C), scale bar represents $100\ \mu\text{m}$; 30 degrees of tilt (B,D) scale bar represents $50\ \mu\text{m}$, inset scale bar represents $10\ \mu\text{m}$.

6.3.1 Electrochemical behavior of inverted cathodes

The electrochemical behavior of planar and microstructured n^+ -Si/Ti/Pt cathodes were compared in a stagnant cell containing $0.50\ \text{M}\ \text{H}_2\text{SO}_4(\text{aq})$. Figure 5.2 displays the time-dependent overpotential, η_T , of planar and microstructured n^+ -Si/Ti/Pt cathodes as a function of current density, J , and orientation, α , with α representing the angle between the gravitational vector and the surface normal of the bottom side of the electrode. At acute angles of α (i.e., predominantly downward-facing electrodes) planar n^+ -Si/Ti/Pt electrodes exhibited large η_T relative to the reversible hydrogen potential, RHE, to drive a constant J for the HER, J_{H_2} . The increase in η_T was proportional to the current density, and abrupt decreases in η_T with time correlated with the periodic release of large gas bubbles from

the electrode surface (Figure 5.2B). In contrast, despite the generation of gas bubbles, n^+ -Si/Ti/Pt microwire array electrodes exhibited stable, and much lower, values of η_T under chronoamperometric control. Downward-facing ($\alpha \sim 0^\circ$) microwire array and planar electrodes at $|j_{H_2}| < 30 \text{ mA cm}^{-2}$ trapped large gas bubbles and exhibited potentials that were unstable with time, but also showed potentials that were lower on average than the potential exhibited by the same electrode when facing upwards ($\alpha = 180^\circ$).

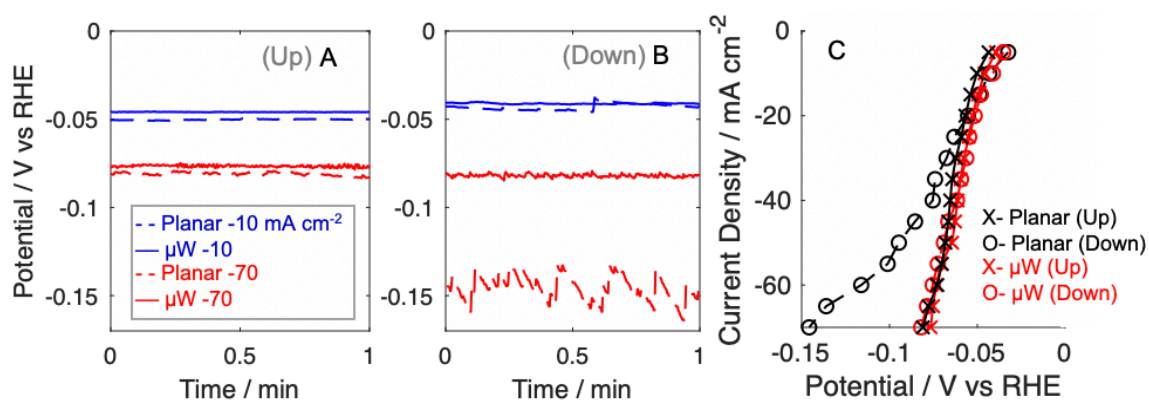


Figure 6.2: Comparison of the (A) upward-facing and (B) downward-facing electrochemical behavior of galvanostatically controlled planar and microstructured cathodes, respectively, in 0.50 M $\text{H}_2\text{SO}_4(\text{aq})$ as a function of current density. Planar Pt electrodes are represented by dashed lines and μW 6|14 electrodes are represented by continuous lines. Devices behaved mutually similarly when facing upward but at high current, inverted planar Pt exhibited increased overpotentials relative to microstructured electrodes. (C) Comparison of the average potential required to produce a constant current density at a planar Pt electrode, black, and a μW 6|14 electrode. Upward-facing behavior is represented by x's, whereas downward-facing behavior is represented by open circles.

6.3.2 Physical characterization of bubble films

To investigate the role of gas coverage on fluctuations in the overpotential, electrochemical experiments were performed in tandem with macroscopic and microscopic imaging of the electrode surface. Figure 5.3 shows changes in the fractional gas coverage,

θ , as a function of time for n^+ -Si/Ti/Pt electrodes held at $J = -30 \text{ mA cm}^{-2}$. Inverted ($\alpha = 15^\circ$) planar n^+ -Si/Ti/Pt electrodes exhibited a time-dependent value of θ that was positively correlated with the absolute overpotential relative to RHE (Figure 5.3A), with greater changes in η_T occurring at larger $|J_{H_2}|$. In contrast, regardless of orientation, microstructured n^+ -Si/Ti/Pt electrodes exhibited stable η_T and θ values over time (Figure 5.3B-D). The average value of θ at a given $|J_{H_2}|$ was a function of the geometry of the n^+ -Si/Ti/Pt microwire array. At $|J_{H_2}| = 30 \text{ mA cm}^{-2}$, $\mu\text{W } 6|14$ electrodes exhibited an average $\theta = 15\%$, whereas $\mu\text{W } 3|11$ and $\mu\text{W } 6|28$ electrodes exhibited an average $\theta = 41\%$ and 52% , respectively. Despite the variation in θ for electrodes of different microwire array geometries, values for η_T were relatively insensitive to the μW array geometry, indicating that gas coverage alone was not a strong predictor of the chronopotentiometric behavior (Figure 5.2B-D). Notably, $\mu\text{W } 6|28$ cathodes maintained low overpotentials for the HER despite having gas coverages comparable to those of planar n^+ -Si/Ti/Pt electrodes. For planar, $\mu\text{W } 3|11$, and $\mu\text{W } 6|28$ electrodes, θ increased asymptotically as $|J_{H_2}|$ increased, although the stable value of θ depended on the microstructure of the electrode.

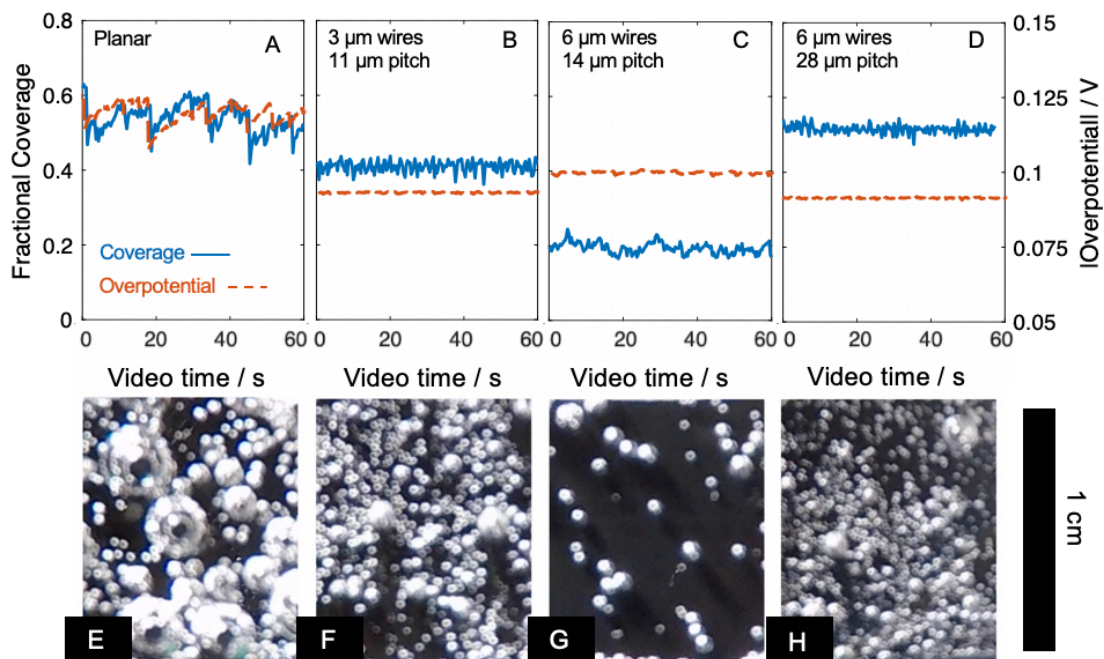


Figure 6.3: (A-D) Comparison of fractional gas coverage of downward-facing n^+ -Si/Ti/Pt cathodes, at $\alpha = 15^\circ$, at -30 mA cm^{-2} in $0.50 \text{ M H}_2\text{SO}_4(\text{aq})$, relative to the absolute overpotential for the HER in $0.50 \text{ M H}_2\text{SO}_4(\text{aq})$ as a function of time. (E-H) Representative images from videos recorded at 60 frames s^{-1} of downward-facing cathodes passing a current density of 30 mA cm^{-2} for the HER. (A,E) planar n^+ -Si(100); Si microwire arrays with a width and pitch, respectively of: (B,F) 3 and 11 μm ; (C,G) 6 and 14 μm ; and (D,H) 6 and 28 μm . Scale bar represents 1 cm.

The primary difference between the gas bubble layer that covered μW and planar n^+ -Si/Ti/Pt electrodes was the size of the bubbles (**Figure 6.3E-H**). The weighted mean diameter, \bar{d}_w , of a gas bubble film is calculated from **Equation 6.1**, where each bubble is weighted its respective projected area.

Figure 6.4 compares $\langle d_w \rangle$, for various n^+ -Si/Ti/Pt electrodes at $\alpha = 15^\circ$ as a function of $|J_{\text{H}_2}|$. At $\alpha = 15^\circ$ and $|J_{\text{H}_2}| = 30 \text{ mA cm}^{-2}$, $\langle d_w \rangle$, at planar n^+ -Si/Ti/Pt electrodes

varied between 0.5 and 3 mm, whereas $\langle d_w \rangle$, was consistently < 0.6 mm at μ W 6|14 and μ W 3|11 electrodes. The variation in θ for different microwire array geometries was caused by a difference in the number density of bubbles, N , as opposed to a difference in the size of the bubbles adhering to the surface (**Figure 6.4E-G**).

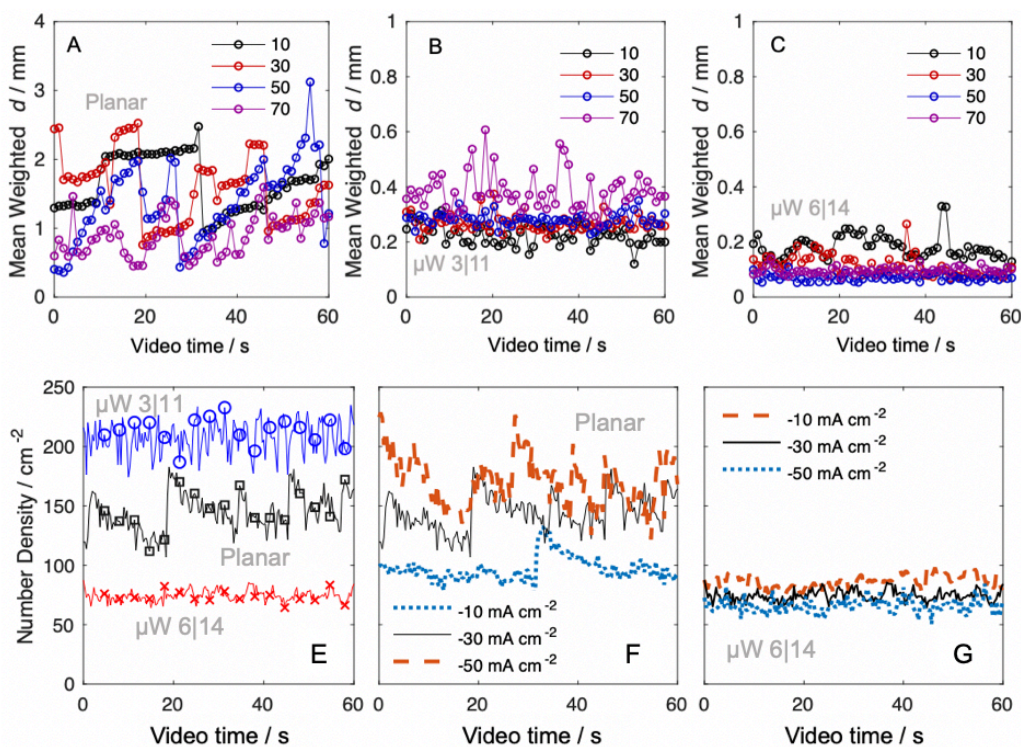


Figure 6.4: (A-C) Weighted mean bubble diameters (**Equation 6.1**) versus video time at $|J_{H_2}| = 10\text{-}70$ mA cm⁻² as measured at (A) n⁺-Si/Ti/Pt planar, (B) μ W 3|11, and (C) μ W 6|14 electrodes in 0.50 M H₂SO₄(aq) at $\alpha = 15^\circ$. (E-G) Number density, N , of bubbles on the electrode surface as a function of time for planar, μ W 6|14, and μ W 3|11 n⁺-Si/Ti/Pt electrodes passing -30 mA cm⁻² in 0.50 M H₂SO₄(aq) at $\alpha = 15^\circ$ represented by black squares, red x's and blue circles respectively. Number density of bubbles on a (F) planar and (G) μ W 6|14 n⁺-Si/Ti/Pt electrode as a function of time and absolute current density towards H₂.

Increasing $|J_{H_2}|$ at inverted, planar n⁺-Si/Ti/Pt electrodes led to lower, more stable $\langle d_w \rangle$, due to a greater N on the surface, whereas for $|J_{H_2}| \leq 50$ mA cm⁻², inverted μ W 6|14

electrodes exhibited a bubble number density that was essentially independent of the applied current density (**Figure 6.4G**). The number density and weighted mean diameter were stable for 16 h of testing at -30 mA cm^{-2} .

To investigate the mechanism behind differences in N as a function of microstructure, the detachment and growth behavior of gas bubbles were measured via high-speed microscopy on upward-facing electrodes. **Figure 6.5** presents the growth and detachment behavior for bubbles released from an upward-facing $\mu\text{W 6|14}$ and $\mu\text{W 6|28}$ electrodes during 15 s of hydrogen evolution at $|J_{\text{H}_2}| = 50 \text{ mA cm}^{-2}$. In contrast to downward-facing electrodes, upward-facing $\mu\text{W 6|28}$ electrodes exhibited low N and θ values. On upward-facing electrodes, the mean departure diameter was not a function of the spacing between microwires, with mean departure diameters at a $\mu\text{W 6|14}$ and $\mu\text{W 6|28}$ electrode having values of $370 \pm 150 \text{ }\mu\text{m}$ and $330 \pm 170 \text{ }\mu\text{m}$, respectively (**Figure 6.5**). Repetitive nucleation was frequently observed at locations on the electrode surface that also exhibited large departure diameters. For bubble growth that is limited by radial transport of $\text{H}_2(\text{aq})$ to the surface, the radius, R , of a bubble as a function of time, t , is given by $R(t) = \tilde{b}(Dt)^{1/2}$, where D is the diffusion coefficient of the gas and \tilde{b} is the dimensionless growth coefficient.¹⁶

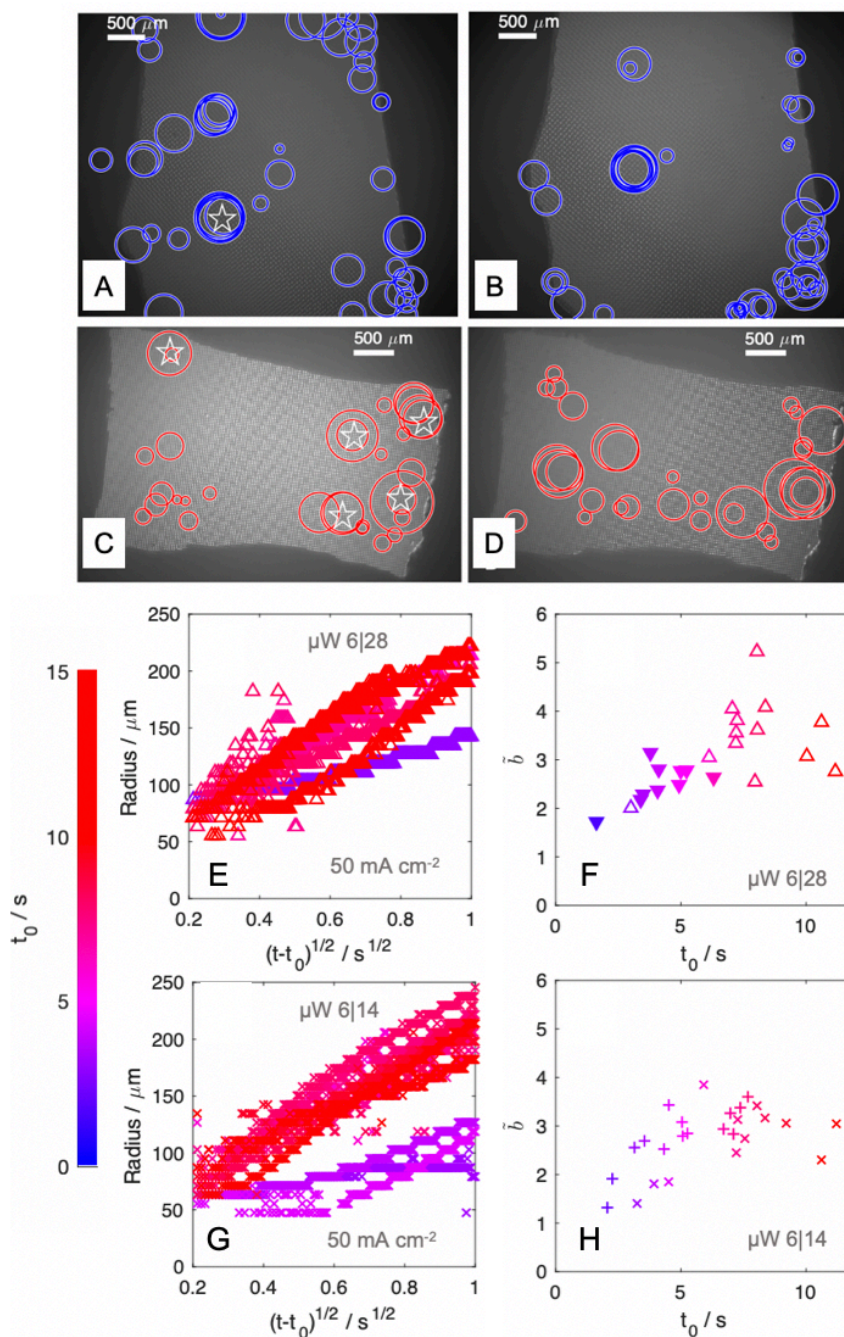


Figure 6.5: (A-D) Map of departure diameters measured during a two separate high-speed microscopy experiments at upward-facing (A-B) $\mu\text{W } 6|14$ and (C-D) $\mu\text{W } 6|28$ electrodes held at -50 mA cm^{-2} for 20 s in $0.50 \text{ M H}_2\text{SO}_4$ (aq). (A). (E, G) Representative radius versus square-root time traces measured via image processing software, with sites labeled in (A,C). (F,H) Calculated \tilde{b} for data presented in (E,G).

At $|J_{H_2}| = 50 \text{ mA cm}^{-2}$, values of \tilde{b} indicated that bubble growth velocities were controlled by diffusion and were stable at individual sites after 10 s (**Figure 6.5G-H**). New nucleation sites continued to form throughout the 20 s measurement, indicating that nucleation was adequately described by classical heterogeneous nucleation theory and the formation of bubbles was thus not limited to preexisting gas cavities.³⁰

6.3.3 *Mass transport properties of bubble films*

The effects of gas evolution on the mass-transport properties of inverted cathodes at $\alpha = 15^\circ$ were investigated by use of a redox-active species, ferric sulfate, as $\text{Fe}^{3+}(\text{aq})$, as a probe (**Figure 6.5A, A.6**). Following a 10 min bulk electrolysis at fixed total current density, the total quantity of $\text{Fe}^{3+}(\text{aq})$ that was reduced to $\text{Fe}^{2+}(\text{aq})$ was determined spectroscopically (**Figure A.6.2**). In the absence of both $|J_{H_2}|$ and external convection, $|J_{Fe}|$ decayed to $< 0.5 \text{ mA cm}^{-2}$ within 45 s (**Figure A.6.3**). At gas-evolving electrodes, the mean mass-transport-limited current density vs time for $\text{Fe}^{3+}(\text{aq})$ reduction, $|J_{Fe}|$, was proportional to $|J_{H_2}|$ but the response depended on the electrode surface (**Figure 6.6B**). Larger $|J_{Fe}|$ values were observed for $\mu\text{W n}^+\text{-Si/Ti/Pt}$ surfaces relative to planar $\text{n}^+\text{-Si/Ti/Pt}$ electrodes, regardless of the gas coverage. $\mu\text{W 6|28}$ electrodes exhibited the largest $|J_{Fe}|$ values at all current densities.

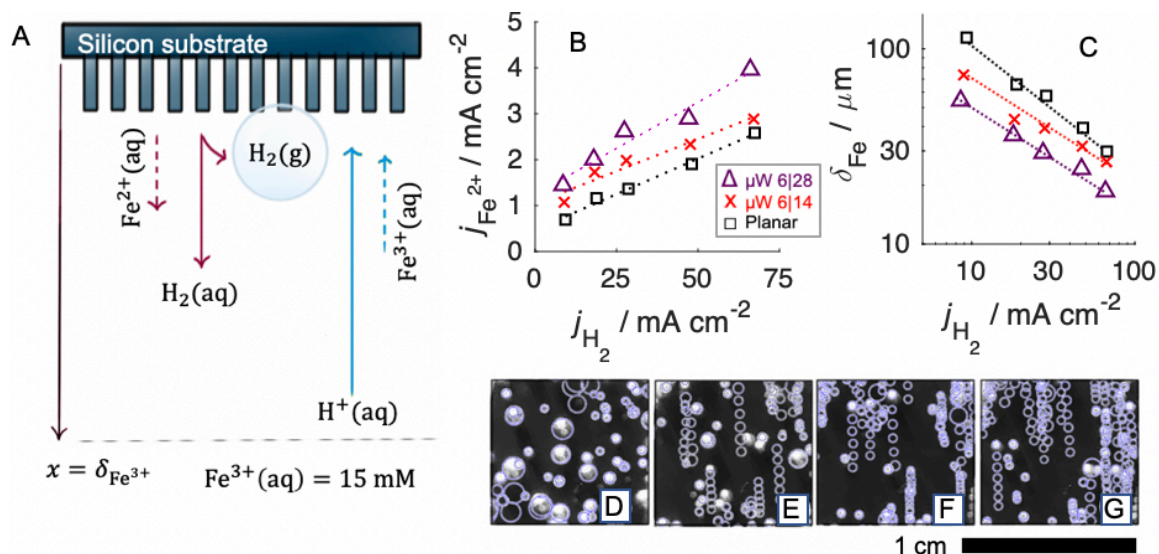


Figure 6.6: (A) Scheme of experimental procedure for diffusion-limited current experiments (B) Diffusion-limited current density measured via spectrophotometric determination of $\text{Fe}^{2+}(\text{aq})$ from 15 mM $\text{Fe}^{3+}(\text{aq})$ in 0.50 M $\text{H}_2\text{SO}_4(\text{aq})$, as a function of current density towards the HER, for various cathodes. Inverted ($\alpha = 15^\circ$) planar, $\mu\text{W 6|28}$, and $\mu\text{W 6|14}$ electrodes are represented as black squares, purple triangles, and red x's respectively, with dotted guidelines. (C) Length of the concentration boundary layer, assuming planar diffusion with the surface concentration of Fe^{2+} approaching zero. (D-G) Representative traces of gas bubbles at an inverted ($\alpha = 15^\circ$) $\mu\text{W 6|14}$ electrode passing -10 (D), -30 (E), -50 (F), and -70 mA cm^{-2} (G) sampled over 0.100 s and superimposed over a single image.

To calculate the concentration boundary layer thickness, δ_{Fe} , from J_{Fe} , the diffusion boundary layer was approximated as a continuous, stagnant layer (**Equation 6.2**):

$$\frac{J_O}{nF} = \frac{D_O}{\delta_O} [C_O^* - C_O|_{x=0}] \quad (6.2)$$

where D_O is the diffusion coefficient of the oxidized species, $n = -1$, F is Faraday's constant, C_O^* is the bulk concentration of the oxidized species and $C_O|_{x=0}$ is the concentration at the surface. Values for δ_{Fe} at inverted $n^+\text{-Si/Ti/Pt}$ microwire array electrodes, as

calculated from J_{Fe} , were inversely proportional to $|J_{H_2}|$ and were between 30 μm and 100 μm across the range of current densities relevant to a solar fuels device. (**Figure 6.5C**). For an inverted ($\alpha = 15^\circ$) μW 6|14 electrode operated at $|J_{H_2}| = 10, 30, 50, 70 \text{ mA cm}^{-2}$, representative traces of gas bubbles were sampled over 0.100 s and superimposed over a single image (**Figure 6.6D-G**). The total gas coverage was not sensitive to current density (**Figure 6.2**), but increases in current density resulted in a substantially larger fraction of bubbles that were in motion.

6.3.4 Electrochemical impedance of bubble films

The effect of the gas bubble layers on the series resistance, R_{sol} , as a function of time was probed via galvanostatic impedance measurements. The measurements were performed at a frequency for which the impedance was predominantly determined by the solution resistance. Planar electrodes at $\alpha = 15^\circ$ exhibited η and R_{sol} values that were more variable with time than the corresponding values for planar electrodes at $\alpha = 90^\circ$. For planar electrodes at $|J_{H_2}| = 30 \text{ mA cm}^{-2}$, the additional ohmic drop, ΔE_{ohm} , due to the presence of a bubble layer was $22 \pm 7 \text{ mV}$ at $\alpha = 15^\circ$ and was $6 \pm 2 \text{ mV}$ at $\alpha = 90^\circ$. Figure 5.6 presents chronopotentiometric traces obtained at planar Pt cathodes as a function of α and $|J_{H_2}|$, overlaid with an envelope representing one standard deviation in ΔE_{ohm} calculated from measurements of R_{sol} . The variance in ΔE_{ohm} accounted for the majority of the fluctuations in the electrode potential with time.

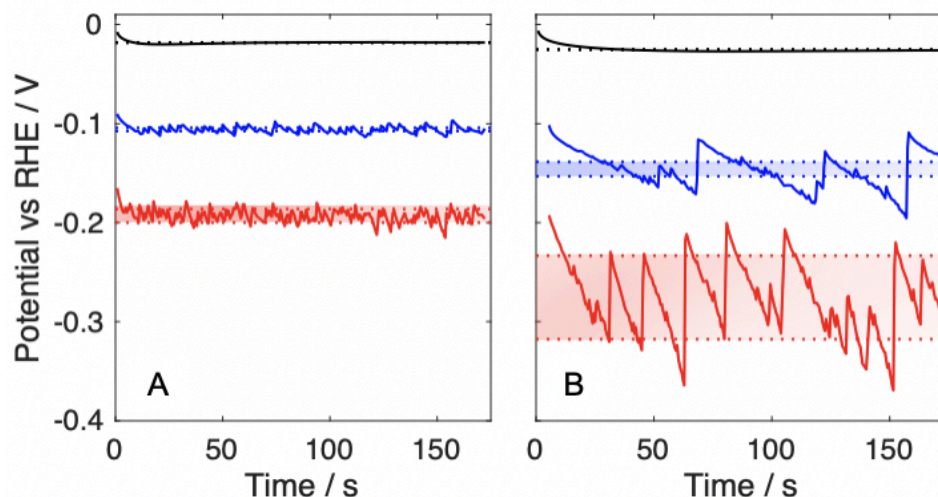


Figure 6.7: Potential versus time data for a planar Pt electrode at (A) 90° orientation and (B) 15° orientation at 10, 30, and 70 mA cm⁻², black, blue, and red lines, respectively. Shaded regions represent the average potential \pm one standard deviation in the potential, corrected for ohmic drop, measured via galvanostatic impedance.

Figure 6.8A presents the average current density vs. overpotential relationship for planar, μ W 6|14, and μ W 3|11 n⁺-Si/Ti/Pt electrodes, respectively, at $\alpha = 15^\circ$ after correcting for ΔE_{ohm} due to the R_{sol} value measured at 0.0 V versus RHE. For comparison, the ideal current vs. overpotential behavior predicted for a planar Pt surface with a Tafel slope of 29 mV dec⁻¹, in the absence of mass-transport limitations, is shown as a continuous black line (**Equation 6.3**):

$$\eta_{Tafel} = a + b \log_{10} |J| \quad (6.3)$$

where a and b are the empirical Tafel parameters. Planar n⁺-Si/Ti/Pt electrodes exhibited substantial deviations from Tafel behavior at all current densities, and the J - η relationship was linear rather than exponential. n⁺-Si/Ti/Pt μ W array electrodes exhibited decreased deviations from Tafel behavior and the J - η relationship was exponential for $|J_{H_2}| < 50$ mA cm⁻².

The relative contributions of ohmic drop, catalyst surface area, and increased concentration of $H_2(aq)$ can be separated into different classes of overpotentials. At an electrode surface covered by gas bubbles at constant current, an additional overpotential required due to an increase in effective current density at sites not covered by gas bubbles is given by **Equation 6.4**:

$$\eta_h = b \log_{10}[A/A'] \quad (6.4)$$

where η_h represents the hyperpolarization, and is dependent on the ratio of A to the remaining active area A' .⁹ In the absence of gas bubbles, accumulation of $H_2(aq)$ in the boundary layer shifts the local reversible hydrogen electrode potential as predicted by a Nernstian relationship (**Equation 6.5**):

$$\eta_c = 2.3 \frac{RT}{nF} \log[C_{H_2}|_{x=0}/C_{H_2}^*] \quad (6.5)$$

where R is the gas constant, F is Faraday's constant and n is the number of electrons involved in the reaction.

The measured ohmic drop contribution was compared to the resistance of a hypothetical layer of gas bubbles with a single thickness, L , and void fraction, f_g . The effective conductivity, K_m , of a mixed-phase layer was calculated from an equation originally proposed by Maxwell (**Equation 6.6**):

$$K_m = (1 - f_g)/(1 + \frac{f_g}{2}) \quad (6.6)$$

and used to estimate the additional ohmic drop during gas evolution (**Equation 6.7**):

$$\Delta E'_{ohm} = \frac{iL(1-K_m)}{\kappa K_m} + \left[\frac{iL}{\kappa} \right] \quad (6.7)$$

where κ is the solution conductivity,²⁵ with the ohmic drop present in the absence of gas bubbles contained within brackets, and $\Delta E'_{ohm}$ represents the remaining ohmic drop after removal of this term.^{9,26}

The total potential drop between the cathode and reference electrode, following correction for the cell resistance, can be expressed by **Equation 6.8**:⁹

$$\eta_T = \Delta E'_{ohm} + \eta_{Tafel} + \eta_h + \eta_c \quad (6.8)$$

Equation 6.8 was used to simulate the J - η relationship of H₂-evolving cathodes as a function of varied f_g , L , and $C_{H_2(aq)}$.

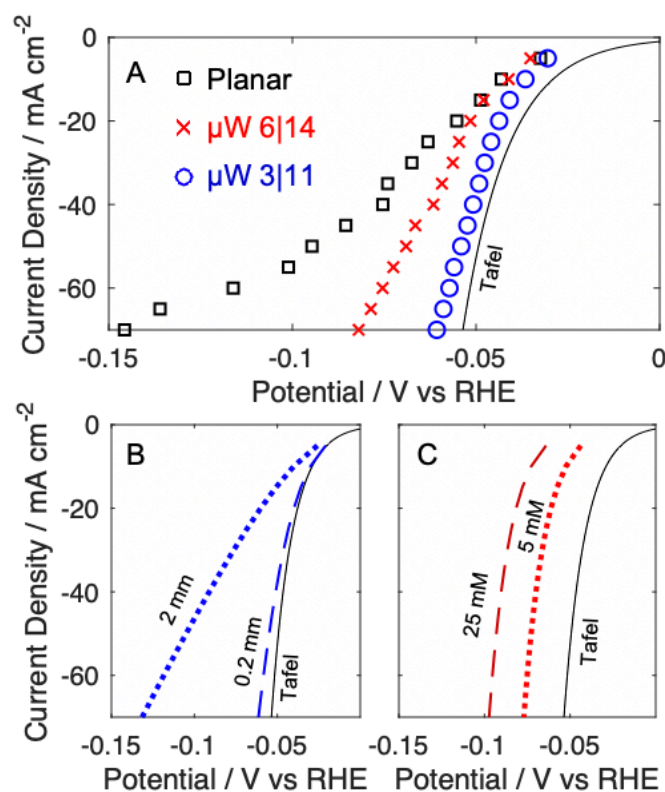


Figure 6.8: (A) Comparison of the steady-state J - E behavior for the HER for planar (black squares), μ W 6|14 (red x's), and μ W 3|11 electrodes (blue circles), in a downward configuration at $\alpha = 15^\circ$ in 0.50 M H₂SO₄(aq). (B) Comparison of the simulated J - η behavior of a Pt cathode covered by a 1 mm (dotted blue line) or a 3 mm thick (dashed blue line) close-packed bubble layer. (C) Comparison of the simulated J - η behavior of a Pt cathode in the presence of $C_{H_2(aq)} = 5$ and 25 mM, depicted as dotted and dashed red lines, respectively.

A quantitative comparison between the coverage of gas bubbles and the observed overpotentials was not performed, due to the difficulty of quantifying L at electrode surfaces that were covered by bubbles exhibiting diameters that varied with position and time. The peak weighted mean diameter of bubbles attached to planar and μW 3|11 electrodes at -30 mA cm^{-2} was 2 mm and 0.2 mm, respectively (**Figure 6.4**). Simulated J - E data for a hypothetical close packed layer of gas bubbles with these values of L are presented as **Figure 6.8B**. Increasing f_g from 0.3 to 0.6, near the limit for a single layer of hexagonally close-packed spheres, increased the overpotential at $|J_{H_2}| = 30 \text{ mA cm}^{-2}$, η_{30} , by 5%, whereas increasing the thickness of the bubble layer to 3 mm increased η_{30} by 44% (**Figure 6.8C**). Relative to a bare Pt surface, decreases of 30% and 60% in the catalyst surface area due to bubble coverage led to an increase in η_{30} of 9% and 23%, respectively. Increasing the local $C_{H_2(aq)}$ to 5 mM or 25 mM led to an increase in η_{30} of 53% and 102%, respectively, relative to a cathode with a surface $C_{H_2(aq)} = 0.78 \text{ mM}$.

6.4 Discussion

The capillary forces due to electrolyte infilling of μW arrays exceed the buoyant forces due to gravity, and thus prevent obstruction of μW electrode surfaces by bubbles, regardless of α . Microwire array electrodes exhibit smaller adhesive forces towards gas bubbles than planar electrodes, leading to more rapid release of bubbles and more stable η_T . Adhesion of individual gas bubbles could occur exclusively at the top face of microwires, known as the Cassie-Baxter state, or additionally at the sidewalls and substrate, known as the Wenzel state.²⁷ Mutually similar departure diameters were measured via high-speed microscopy for μW 6|14 and μW 6|28 electrodes, which is inconsistent with an

adhesion process that depends on the internal surface area of the microwire array but is consistent with adhesion being dominated by the top-facing area of an individual microwire or defect site. Results from this work extend a prior study that demonstrated stabilized photoelectrochemical behavior of Si μ W and nanowire array electrodes at $\alpha = 90^\circ$ due to a reduced θ relative to planar electrodes,²²⁻²³ and additionally indicate that μ W electrodes exhibit chronopotentiometric behavior that is insensitive to θ even against buoyant force vectors directed antiparallel to the surface normal.

Increases to $C_{H_2(aq)}$ and L constituted the largest relative contributions to increased values of η_T at small and large $|J_{H_2}|$, respectively. At $|J_{H_2}| = 30 \text{ mA cm}^{-2}$ the effects of θ on f_g and A^* contributed $< 10 \text{ mV}$ of added overpotential. These results are consistent with the differing chronopotentiometric behavior of μ W array and planar electrodes having mutually similar θ values. These observations suggest that the primary factor leading to stabilized potentials at μ W array electrodes is a reduced gas layer thickness due to a decreased departure diameter for H_2 bubbles. Further decreases in bubble layer thicknesses may be obtained by decreasing the tip radius of the μ W array,²⁴ for example by utilization of Si microcone arrays that have been developed to minimize optical reflection losses at photoelectrodes.²⁸⁻²⁹

Electrodes prepared from μ W 6|14 arrays had the highest areal filling fraction of microwires and exhibited the lowest θ values at all current densities. The differences in θ for inverted μ W 6|14 and μ W 6|28 electrode geometries were caused by variations in the density of nucleation sites on the surface, as opposed to differences in the departure diameters of bubbles (**Figure 6.5**). Values of θ measured at μ W 6|28 arrays were very sensitive to the orientation of the electrode, whereas μ W 6|14 arrays exhibited low values

of N and θ at $\alpha = 15^\circ$ (Figures 6.3-6.4). Due to the high free-energy barrier to forming a new gas-liquid interface, gas bubbles predominately formed at cavities located at defects or at small gas bubbles left behind during release of macroscopic bubbles (**Figures 6.5, 6.9**).³⁰ The increased filling fraction at $\mu\text{W } 6|14$ electrodes, relative to $\mu\text{W } 6|28$ and $\mu\text{W } 3|11$ electrodes, prevented isolated bubbles from propagating new nucleation sites upon detachment, and resulted in lower values of N and θ . Studies on isolated Pt nanoelectrodes have shown that $C_{\text{H}_2(\text{aq})} > 0.1 \text{ M}$ are required to form new heterogeneous nuclei.⁴ The behavior of the $\mu\text{W } 6|14$ electrodes at macroscale electrode areas in this work demonstrates that only a few such nuclei are needed across the surface to generate sufficient convection to prevent further nucleation. Differences in θ between inverted $\mu\text{W } 6|14$ and $\mu\text{W } 6|28$ electrodes are caused by emergent properties of the microwire arrays that are specific to testing conditions relevant to operation of a solar fuels device, and moreover would not be readily predicted from the characteristics of bubble formation on individual, isolated Si microwires.

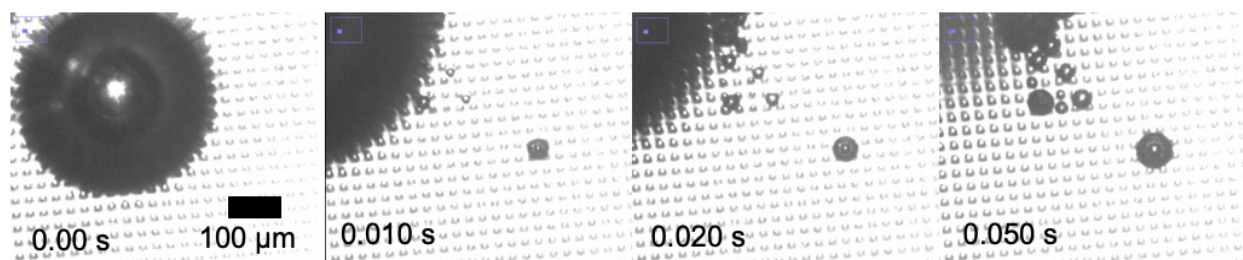


Figure 6.9: High speed microscope images recorded at an upward-facing $\mu\text{W } 6|28$ electrode evolving H_2 in $0.50 \text{ M } \text{H}_2\text{SO}_4(\text{aq})$. The departing gas bubble at 0.010 s left multiple nucleation sites within the microwire array.

In the absence of bubbles, accumulation of $\text{H}_2(\text{aq})$ at the surface leads to a substantial η_C , which shifts the J - η characteristic towards more negative potentials while

maintaining an exponential relationship between J and η . Such behavior is consistent with the comparison of steady-state overpotentials at downward-facing μW -array electrodes (**Figure 6.3B-D**) suggesting that a decrease in θ led to an increase in $C_{\text{H}_2(\text{aq})}$ at the surface due to the absence of liquid-gas interfaces available to collect $\text{H}_2(\text{aq})$. This result is consistent with the observation of increased overpotentials at -10 mA cm^{-2} for upward-facing electrodes (**Figure 6.2A-B**), which readily detached bubbles, in comparison to downward-facing electrodes. At low $|J_{\text{H}_2}|$ the voltage loss due to $\Delta E'_{ohm}$ is small in comparison to η_C so the presence of bubbles consequently led to a lower $C_{\text{H}_2(\text{aq})}$ and lower η_T at downward-facing electrodes. The linear relationship between R and $t^{1/2}$ for bubbles on upward-facing microwire arrays demonstrated that bubble growth was controlled by transport of dissolved H_2 to the gas-liquid interface from a fluid volume comparable to the volume of gas bubbles,¹⁴² which displayed diameters greater by a factor of 10 than the length of individual microwires. In this respect, the growth behavior of bubbles on microwire arrays is physically similar to the growth behavior at a planar surface. Large dimensionless-growth coefficients were observed at upward-facing microwire array electrodes, which have been used to determine $C_{\text{H}_2(\text{aq})}$ (**Figure 6.5**),³¹ however \tilde{b} values measured at $|J_{\text{H}_2}| > 10 \text{ mA cm}^{-2}$ were too large to ignore the effects of advection (**A.6**).³² Because η_C is inversely proportional to n , concentration overpotentials incurred during the oxygen-evolution reaction ($n = 4$) will be reduced relative to overpotentials during the HER ($n = 2$). Assuming that O_2 and H_2 exhibit similar degrees of supersaturation prior to nucleation,⁴⁻⁵ evolving O_2 on the top side of a solar-fuels device will lead to reduced total concentration overpotentials because low gas coverages on the top side of a device are

likely to lead to an increase in supersaturation of the electrochemical reaction product in the electrolyte.

Despite the physical obstruction of electrolyte responsible for mass transport of reactants and products, the generation of gas bubbles led to an increased $|J_O|$ in comparison to $|J_O|$ in a stagnant electrolyte (**Figure 6.6**). Assuming that the Faradaic efficiency for $H_2(g)$ evolution is not a strong function of J_{H_2} , over the range of 10-70 mA cm⁻²,³³ transport of $Fe^{3+}(aq)$ to the electrode surface was driven by volumetric displacement of electrolyte due to H_2 evolution (Figure 5.5B). Platinized Si μ W arrays consistently exhibited larger $|J_{Fe}|$ values than planar n⁺-Si/Ti/Pt electrodes, regardless of gas bubble coverage, however the largest $|J_{Fe}|$ values were observed at the arrays that had the largest θ values. The relationship between δ and J_{H_2} is consistent with theoretical relationships for mass transport driven by microconvection or fluid penetration during individual bubble detachment, for which $\delta \sim J_{H_2}^{-1/2}$, as opposed to macroconvection driven by rising bubble films, for which $\delta \sim J_{H_2}^{-1/3}$.³⁴ Comparable values for δ have been measured via $Ce^{3+/4+}$ potentiometric titration for Pt foils at $\alpha = 90^\circ$ and 180° evolving $O_2(g)$ or $H_2(g)$ in 1.0 M $H_2SO_4(aq)$.³⁵ Previous investigations have inferred that surface roughness did not have substantial effects on δ or that the decreased δ was a function of the increased nucleation density.³⁶⁻³⁷ The results in this work, for electrodes with explicitly controlled microstructure, at $\alpha = 15^\circ$, and at current densities relevant to solar-fuels devices, demonstrate that surface adhesion and microconvection are the dominant independent variables controlling the mass transport properties of bubble films, as opposed to nucleation density or buoyancy-driven convection. For electrodes oriented against \hat{g} in a stagnant

electrolyte, the generation of bubbles increases reactant influx and product efflux such that mass transport will not limit device performance.

6.5 Conclusion

Collectively, the results obtained for inverted cathodes suggest that efficient and stable electrochemical generation of gases can be obtained via control of the electrode microstructure. When oriented against gravity, the low adhesive force and high number density of bubbles at μW 3|11 and μW 6|28 electrodes leads to thin layers of gas bubbles that exhibit a low resistance, yielding electrochemical behavior that is insensitive to θ . Notably, μW electrodes that maintained a high N and θ exhibited the largest mass transport coefficients and lowest η . In contrast, at J_{H_2} values relevant to solar-fuel device operation in unconcentrated sunlight, the absence of bubbles is not desirable, and produced deleterious increases in η that were comparable to the kinetic overpotential exhibited by a Pt catalyst. Moreover, planar n^+ -Si/Ti/Pt electrodes exhibited the worst performance of all of the electrodes studied herein, because they produced large, stationary bubbles that generated the least convection and consequently contributed to a large ΔE_{ohm} . Optimal electrode morphologies and geometries will therefore nucleate bubbles across the surface, keeping $C_{H_2(aq)}$ in near-equilibrium with $H_2(g)$ at the operating pressure, and will moreover be structured to quickly detach bubbles from the surface, thereby minimizing the thickness of the gas layer and maximizing local convection. Microcavities and surface functionalization can facilitate nucleation to maintain low $C_{H_2(aq)}$ values at the surface.³⁸⁻

³⁹ Further studies should assess whether electrodes that include membranes containing hydrophobic polymer chains also result in sufficient capillary forces to prevent infilling of

gas bubbles, and/or whether further surface modification of the microstructure can prevent such infilling. Although the gas coverage of Pt catalysts was not a substantial contributor to the total η , additional studies should investigate the electrochemical behavior of microstructured electrodes covered by catalysts with increased Tafel slopes, relative to Pt catalyzing the HER, to determine how gas coverage affects less active but earth-abundant catalysts for the HER and OER. The electrodes in this work were degenerately doped and therefore insensitive to the optical effects of gas coverage. Experiments on upward-facing, photoactive microwire electrodes are needed to determine whether high coverages of small gas bubbles are suitable for efficient collection of sunlight.

Chapter 7

OPTICAL AND ELECTROCHEMICAL EFFECTS OF H₂ AND O₂ BUBBLES AT UPWARD-FACING SI PHOTOELECTRODES

Kempler, P. A., Ifkovits, Z.P., Yu. W., Carim, A.I., & Lewis, N.S. (2020). Optical and electrochemical effects of H₂ and O₂ bubbles at upward-facing Si photoelectrodes. *In preparation*

7.1 Introduction

Bubbles are generally regarded as deleterious to the performance of photoelectrochemical cells, and have been reported to act as concentrating “miniature lenses” that result in increased photocorrosion.^{21, 126, 143} Bubbles are not optically absorbing, with a refractive index lower than their surrounding medium, and therefore primarily lead to the forward scattering of light.¹⁴⁴ In research laboratories, photoelectrochemical efficiency measurements are often performed on electrodes that are 0.1–1 cm² in area, which magnifies the scattering effects of mm-scale bubbles.¹⁸ A few studies have directly quantified the optical effects of gas evolution.¹⁴⁵⁻¹⁴⁷ H₂ bubbles led to > 20% reductions in the light-limited photocurrent density at small area upward-facing, platinized, planar p-Si photocathodes under simulated Air Mass (AM) 1.5 illumination.¹⁴⁵ Rising layers of O₂ bubbles with 40–50 μm radii have been reported to reflect 1–5 % of the incident illumination on a side-facing fluorine-doped tin oxide surface held at 1–8 mA

cm⁻² of current density.¹⁴⁷ However, the optical and electrochemical effects of surface-attached O₂ bubbles on upward-facing photoanodes have yet to be quantified, especially on large area electrodes that will be necessary in practical implementations of such devices.

Crystalline Si is well suited for studies of the nucleation and growth of gas bubbles during photoelectrochemical H₂(g) or O₂(g) evolution. Wet-chemical methods for preparing polished Si surfaces that have minimal densities of particles and organic contaminants have been well established by the microelectronics industry.¹⁴⁸ Si photocathodes are thermodynamically stable while evolving H₂ under cathodic conditions in 0.50 M H₂SO₄(aq).¹⁴⁹ When protected with conformal, thin films of TiO₂/Ni, Si photoanodes are stable for >100 h while evolving O₂ under anodic conditions in 1.0 M KOH(aq).¹⁵⁰ Si μW arrays have previously been shown in **Chapter 6** to influence the number density and radius of gas bubbles at downward-facing cathodes evolving H₂(g).¹⁵¹

Herein, ray-tracing simulations were combined with experimental measurements on cm-scale n-Si/TiO₂/Ni photoanodes and p-Si photocathodes to characterize the effects of H₂ and O₂ evolution on the optical and electrochemical performance of upward-facing photoelectrodes. Steady-state photoelectrochemical experiments at upward-facing planar and μW n-Si/TiO₂/Ni photoanodes have facilitated comparison of the influence of surface microstructure on the coverage and contact angle of gas-layers as well as resulting effects on the optical losses and ohmic resistance during device operation while evolving O₂(g). A dilute, redox-active tracer species was used to evaluate unassisted microconvection at upward-facing photoanode surfaces during O₂(g) evolution. Moreover, the nucleation rates and coverages of gas bubble layers were compared as a function of surface free energy at upward-facing hydrogen-evolving Si photocathodes. Ray-tracing simulations allowed the

photocurrent density at upward-facing crystalline Si photoelectrodes to be predicted as a function of gas coverage, bubble radius, and contact-angle. Experiments at downward-facing p-Si photocathodes and downward-facing n-Si/TiO₂/Ni photoanodes allowed additional quantification of the coverage of surface-attached gas bubbles while concomitantly measuring their effect on the photocurrent behavior of such systems.

7.2 Experimental Methods

Detailed descriptions of materials, sample preparation methods, mass-transport measurements, and image analysis are provided in the Appendix.

Sample fabrication: N-type Si microwire arrays were fabricated via a deep reactive-ion etching process described previously, starting from a (100)-oriented P-doped Si wafers with a resistivity of 0.4 Ω -cm.¹⁵¹ The wire diameter and pitch were defined by the photolithographically patterned etch mask. The holes in the masks had a nominal diameter of 6 μ m; a center-to-center pitch of 14 μ m or 28 μ m; and the wires were etched to a height of 30 μ m. All samples were cleaned via the “Standard Clean 1” and “Standard Clean 2” procedures developed by the Radio Corporation of America (RCA) to remove organics and metal contaminants, respectively (details on the cleaning procedures are provided in the Appendix, A.1).¹⁴⁸ 1000 cycles of of amorphous TiO₂ were deposited by atomic-layer deposition from a tetrakis(dimethylamido)titanium (TDMAT) precursor at a table temperature of 150 °C at a nominal deposition rate of 5.5 Å cycle⁻¹. Planar photoanodes were sputtered with 5 nm of Ni whereas Si microwire array photoanodes were sputtered with 10 nm of Ni, to ensure uniform coverage of the sidewalls of the microwires. Planar Si photocathodes were prepared from (100)-oriented B-doped Si wafers having a nominal resistivity of 10–20 Ω -cm. Hydroxyl-terminated p-Si surfaces were prepared via

immersion in an RCA Standard Clean 1 bath for > 5 min, followed by rinsing in copious deionized water immediately prior to photoelectrochemical characterization. H-terminated p-Si surfaces were prepared via immersion in buffered oxide etchant (Transene) for > 10 s followed by rinsing in deionized water and drying in a stream of N₂(g) immediately prior to photoelectrochemical characterization.

Upward-facing gas-evolution: Broad-spectrum illumination was provided by a 300 W ELH-type tungsten-halogen lamp with a dichroic rear reflector. The power supplied to the lamp was constant and the illumination intensity at the photoelectrode was controlled by the use of neutral density filters. The intensity of the lamp was measured by a NIST-traceable Si photodiode (Thorlabs, FDS100-Cal) mounted at the same position as the photoelectrodes but outside the electrolyte. Narrow-band illumination was provided by a light-emitting diode, LED, with an intensity-weighted average intensity at 630 nm (Thorlabs, M625L2). The emission intensity of the LED was modulated to set the light-limited photocurrent density, J_{ph} , at the photoelectrode. In alkaline electrolytes [1.0 M KOH(aq)], a Hg/HgO electrode in a Teflon casing was used as the reference electrode and a nickel wire behind a Fumasep FAAM-15 membrane (Fuel Cell Store) was used as a counter electrode. In acidic electrolytes [0.50 M H₂SO₄(aq)], a saturated calomel electrode behind a glass frit was used as the reference electrode and a Pt mesh behind a Nafion-117 membrane (Fuel Cell Store) was used as a counter electrode. The potential of the reference electrode in both cells was referenced to the reversible hydrogen electrode, RHE, as measured under 1 atm of H₂(g) using a Pt wire coated with Pt black. The cell was open to the atmosphere and was filled with 0.100 L of electrolyte.

Downward-facing gas-evolution: The illumination sources, reference electrodes, counter electrodes, and separators were identical to those used in the upward-facing electrode experiments. Illumination provided by an LED was reflected into the cell using a Ag-coated mirror. The cell was open to the atmosphere and was filled with 0.050 L of electrolyte. Gas coverages were quantified by image processing in MATLAB (Appendix A.7).

Ray-tracing simulations: Simulations were performed using a ray-tracing program written in Python. The simulation was performed for a 2D slice of a 1 cm wide electrode covered by bubbles that were uniform in R_b and θ_b and distributed evenly across the surface. To approximate unpolarized light, the parent ray was initially weighted with equal field intensity in the in-plane and out-of-plane directions. Reflections obeyed the Fresnel equations and parent rays were resolved to 50 ray children, or until an individual ray contained 1% of the original ray power. An infinite absorber layer with an internal quantum yield of unity was assumed, so all rays entering the absorber produced electron-hole pairs that generated photocurrent.

7.3 Results

7.3.1 *N-Si/TiO₂/Ni Photoanodes in 1.0 M KOH(aq)*

The role of electrode microstructure on the behavior of gas bubbles was investigated over cm^2 areas using microfabricated electrodes having regular, micron-scale features. N-type Si microwires with uniform coatings of TiO_2 and Ni, n-Si/ TiO_2 /Ni, were prepared by atomic-layer deposition and RF-sputtering (**Figure 7.1A**). The TiO_2 provided a transparent, conducting protection layer against the corrosive electrolyte and the Ni served as a catalytic layer for the oxygen-evolution reaction.¹⁵⁰ The thickness of the TiO_2

and Ni at a planar substrate was 46 nm and 10 nm, respectively, as measured via ellipsometry. Planar n-Si/TiO₂/Ni photoanodes were prepared in the same fashion but were sputtered with 5 nm Ni. **Figure 7.1B-C** depict plan-view and cross-section scanning-electron micrographs (SEMs) of a microwire array with 6 μm diameter and 14 μm pitch, μW 6|14. SEMs of a μW 6|28 n-Si/TiO₂/Ni sample are provided as **Figure 7.1E-F**. The continuous etching process in the SF₆ and O₂ led to smooth sidewalls with a small amount of nanoscale roughness at the base of the array. The diameter at the tips and base of the wires was $6.1 \pm 0.2 \mu\text{m}$ and $7.4 \pm 0.2 \mu\text{m}$, respectively, for the μW 6|14 array and was $6.1 \pm 0.1 \mu\text{m}$ and $4.8 \pm 0.2 \mu\text{m}$, respectively for the μW 6|28 array.

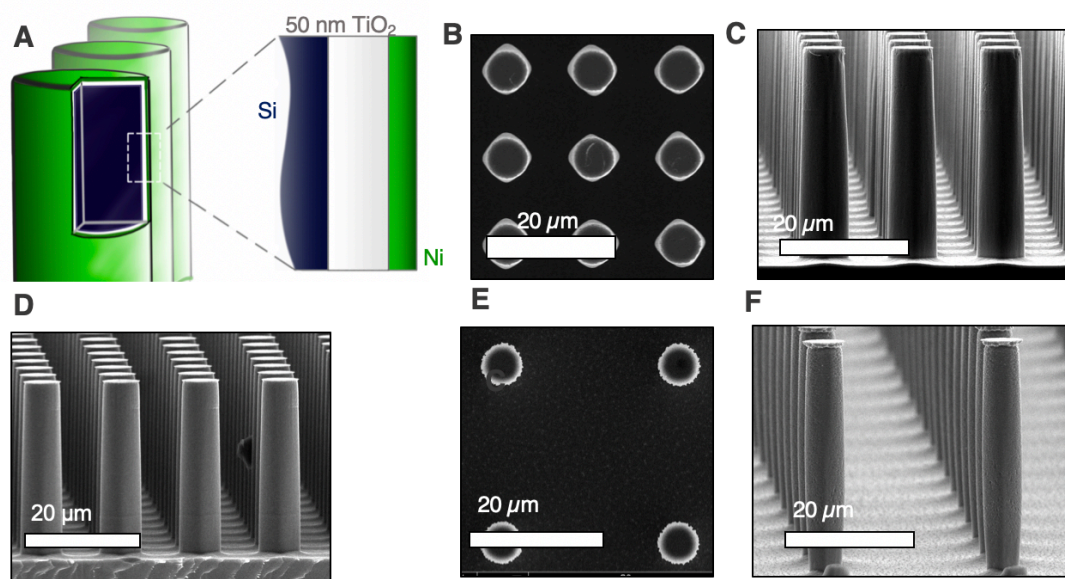


Figure 7.1: (A) Scheme of n-Si μW/TiO₂/Ni electrodes. Silicon (dark blue) was radially coated with TiO₂ (white) via ALD and Ni (green) via sputtering. (B,E) Plan-view scanning electron micrographs of (B) μW 6|14 and (E) μW 6|28 n-Si/TiO₂/Ni (C,F) Cross-section scanning electron micrographs of (C) μW 6|14 and (F) μW 6|28 n-Si/TiO₂/Ni. (D) Cross-section scanning electron micrograph of μW 6|14 p-Si.

The optical effects of O₂ bubbles on upward-facing electrodes were investigated for electrodes in 1.0 M KOH(aq). **Figure 7.2A** presents the current density vs potential, J - E , behavior of n-Si/TiO₂/Ni photoanodes under simulated 1-Sun conditions, as measured via linear-sweep voltammetry at a scan rate of 200 mV s⁻¹, before and after extended potentiostatic holds at 1.6 V vs RHE (**Figure 7.2B**). Data were not corrected for the substantial iR drop between the working and the reference electrode. Electrodes were poised at a potential at which J was light-limited, J_{ph} , producing conditions under which efficient charge separation produced by the potential drop across the space-charge region minimized effects due to changes in the exposed catalyst area, concentration overpotential, and/or electrolyte resistance. The thickness of the Ni layer on the planar n-Si/TiO₂/Ni was controlled so that microstructured and planar photoanodes yielded similar J_{ph} under nominally identical illumination conditions. Gas layers at oxygen-evolving n-Si/TiO₂/Ni photoanodes were characterized by large numbers of bubbles that released frequently at small radii. Under simulated 1-Sun illumination, J_{ph} was 20 mA cm⁻² at either planar or μW 6|14 n-Si/TiO₂/Ni photoanodes, which produced streams of bubbles due to nucleation of bubbles predominantly at a small number of sites across the surface (**Figure 7.2C-D**). The number of nucleation sites increased as the illumination intensity increased, leading to a more uniform coverage of bubbles across the photoanode surface. The bubbles at the planar n-Si/TiO₂/Ni photoanode were larger in radius than the bubbles produced by μW 6|14 n-Si/TiO₂/Ni photoanodes.

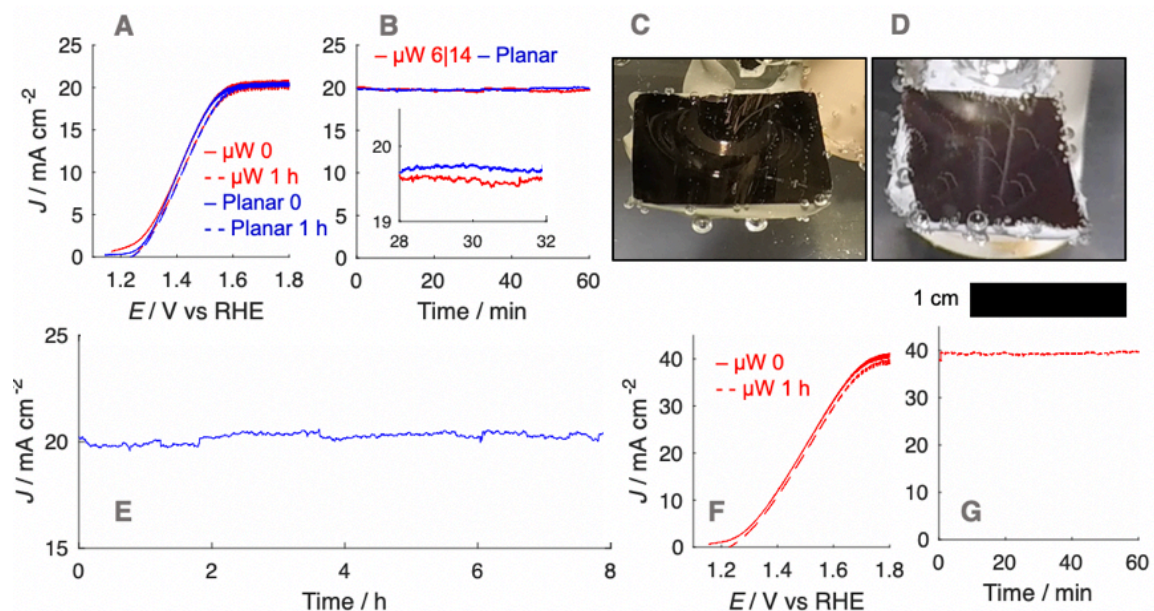


Figure 7.2: (A) J - E behavior for upward-facing planar (blue) and μ W 6|14 (red) n-Si/TiO₂/Ni photoanodes in stagnant 1.0 M KOH(aq) recorded at 200 mV s⁻¹ under illumination from an ELH type W-halogen lamp. Forward scans were recorded before (continuous) and reverse scans were recorded after (dashed) 1 h of continuous O₂ evolution at 1.6 V vs RHE. (B) $J_{\text{ph}}-t$ behavior for photoanodes in (A), held at 1.6 V vs RHE. (C,D) Photographs of a (C) planar and (D) μ W 6|14 n-Si/TiO₂/Ni electrode at $J_{\text{ph}}=20$ mA cm⁻². (E) Extended stability test of a planar n-Si/TiO₂/Ni electrode at 1.6 V vs RHE under illumination from an ELH-type W-halogen lamp in stagnant 1.0 M KOH(aq). (F) J - E behavior for an upward-facing μ W 6|14 n-Si/TiO₂/Ni photoanode as in (A) following a doubling of the light intensity. (G) $J_{\text{ph}}-t$ behavior of the photoanode in (F) at 1.8 V vs RHE.

The production of O₂ bubbles during gas evolution did not lead to a substantial change in J_{ph} , which remained stable and close to the measured maximum during voltammetry (**Figure 7.2A**). This $J_{\text{ph}}-t$ behavior did not change during extended testing at 1.6 V vs RHE (**Figure 7.2E**). Linear-sweep voltammograms after 1 h of continuous photoanodic operation showed that the J - E behavior was not substantially affected by the presence of a sparse gas bubble film. Illumination with 2-Suns of intensity yielded similarly

stable $J_{\text{ph}}-t$ behavior, consistent with the $J-E$ behavior before and immediately after chronoamperometry (**Figure 7.2F-G**).

The effect of gas evolution on the Nernst diffusion layer was quantified for n-Si/TiO₂/Ni photoanodes in the presence of a dilute, redox-active tracer, Fe(CN)₆⁴⁻, whose oxidation product, Fe(CN)₆³⁻ strongly absorbs visible light (**Figure 7.3A**). Measurements were performed on both downward-facing and upward-facing electrodes. During photoanodic operation at 2.1 V vs RHE, J_{ph} was set by the illumination intensity from the LED. The average partial photocurrent passed towards Fe(CN)₆⁴⁻ oxidation was calculated from the concentration of Fe(CN)₆³⁻ measured in the cell after electrolysis. During the forward scan, two anodic peaks were observed, corresponding to surface oxidation of Ni and oxidation of Fe(CN)₆⁴⁻. After electrolysis, these peaks were not present during the reverse scan (**Figure 7.3B**), indicating that the Fe(CN)₆⁴⁻ concentration at the surface approached zero and that the electrochemically addressable nickel was fully oxidized. Measurements of the electrochemical behavior of Fe(CN)₆⁴⁻ in 1.0 M KOH(aq) at a Ni wire and at Au wire are presented as **Figure A.7.1**. The Ni electrode was measured for comparison to the surface behavior of the n-Si/TiO₂/Ni photoanodes whereas the Au electrode measured the electrochemical behavior of Fe(CN)₆⁴⁻ in the absence of surface redox waves.

Equation 7.1 relates the diffusion-limited current density for Fe(CN)₆³⁻ production, $j_{\text{Fe(III)}}$, to the bulk concentration of Fe(CN)₆⁴⁻, $C_{\text{Fe(II)}}$, and the mass-transport velocity, $m_{\text{Fe(II)}}$, across the diffusion layer.

$$j_{\text{Fe(III)}} = nFm_{\text{Fe(II)}} [C_{\text{Fe(II)}}^* - C_{\text{Fe(II)}}^0] \quad (7.1)$$

where $C_{\text{Fe(II)}}^0$, the concentration at the electrode surface, is assumed to be zero at sufficiently positive potentials. A detailed description of the mass-transport velocity measurements is provided in the Appendix (A.7). The mass-transport velocity at 1.3 V vs RHE, in the absence of oxygen evolution, was $4.17 \pm 0.06 \times 10^{-4} \text{ cm s}^{-1}$. The $\langle j_{\text{Fe(III)}} \rangle$ measured spectroscopically was within 3% of $\langle j_{\text{Fe(III)}} \rangle$ measured using chronoamperometry at 1.3 V vs RHE. Calculated values of $m_{\text{Fe(II)}}$ were slightly larger for planar n-Si/TiO₂/Ni electrodes than for μW n-Si/TiO₂/Ni electrodes, and $m_{\text{Fe(II)}}$ at upward-facing photoelectrodes was consistently larger than $m_{\text{Fe(II)}}$ for downward-facing photoelectrodes (**Figures 7.3C**). The value of $m_{\text{Fe(II)}}$ for downward-facing or upward-facing electrodes grew at an increasing rate when $J_{\text{O}_2} > 20 \text{ mA cm}^{-2}$, but for $J_{\text{O}_2} < 20 \text{ mA cm}^{-2}$, few bubbles were observed at the electrode surface and $m_{\text{Fe(II)}}$ was only slightly larger than $m_{\text{Fe(II)}}$ in a stagnant cell (**Figure 7.3C**).

Side-view, false colored photographs of illuminated gas streams emanating from upward-facing photoanodes (**Figure 7.3D-F**) revealed small streams of bubbles that were difficult to observe in top-down images. Fewer, larger bubbles were released on planar n-Si/TiO₂/Ni photoanodes (**Figure 7.3D**) than on μW 6|14 or μW 6|28 n-Si/TiO₂/Ni photoanodes (**Figure 7.3E,F**). The vertical gas streams at μW 6|14 and μW 6|28 n-Si/TiO₂/Ni electrodes generated a horizontal flow of electrolyte at the electrode and at the electrolyte surface. Near the electrode surface, this flow was directed towards the center of the electrode, but at the electrolyte surface the flow was directed towards the edges of the electrode. $J_{\text{ph}}/J_{\text{ph}}^{\text{bare}}$ was nearly constant with time, and for $J_{\text{ph}} \leq 30 \text{ mA cm}^{-2}$ the optical losses did not exceed 2% of J_{ph} at a bare Si surface, despite substantial differences in the distribution of gas bubbles in the $\sim 1 \text{ cm}$ thick, illuminated layer of electrolyte.

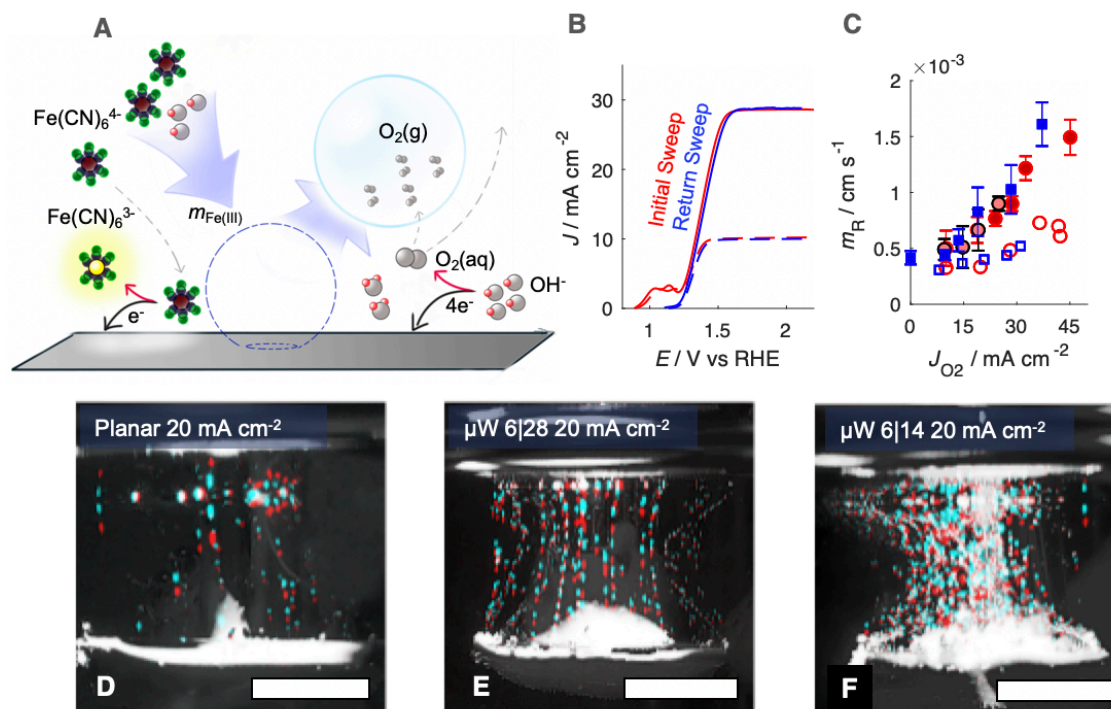


Figure 7.3: (A) Scheme of diffusion tracer experiments using $\text{Fe}(\text{CN})_6^{4-}$ as a probe. OH^- and $\text{Fe}(\text{CN})_6^{4-}$ are brought to the surface via diffusion and bubble-generated microconvection and contributed to Faradaic current. (B) J - E behavior of planar n-Si/TiO₂/Ni photoanode in 10 mM $\text{Fe}(\text{CN})_6^{4-}(\text{aq})$, 1.0 M KOH(aq) before (red) and after (blue) a 5 min potential hold at 2.1 V vs RHE. (C) Mass-transport velocity as a function of anodic current density towards O₂ for planar, blue squares, $\mu\text{W } 6|14$ n-Si/TiO₂/Ni, dark-red circles, and $\mu\text{W } 6|28$ n-Si/TiO₂/Ni, light-red circles, photoanodes in 10 mM $\text{Fe}(\text{CN})_6^{4-}(\text{aq})$, 1.0 M KOH(aq). Upward-facing measurements are shown by filled markers whereas downward-facing measurements are shown as open markers. Error bars on upward-facing measurements represent one standard deviation across three independent potential holds. (D-F) False-colored photographs of planar (D), $\mu\text{W } 6|28$ (E), and $\mu\text{W } 6|14$ (E) n-Si/TiO₂/Ni photoanodes during O₂ evolution in 10 mM $\text{Fe}(\text{CN})_6^{4-}(\text{aq})$, 1.0 M KOH(aq) at $J_{\text{ph}} = 20 \text{ mA cm}^{-2}$. Two frames separated by 50 ms were overlaid with changes highlighted in red and cyan, with red pixels representing the first frame and cyan pixels representing the second frame. All scale bars represent 5 mm.

Upward-facing planar or μW n-Si/TiO₂/Ni electrodes produced small coverages of gas bubbles that did not contribute to substantial increases in the ohmic resistance or concentration overpotential. (**Figure 7.2A,F**). Moreover, bubbles did not significantly reflect photons away from the semiconductor (**Figure 7.2B,E,G**). The observation of gas bubble streams seen in this work has previously been reported at Pt microelectrodes in 1.2 M H₂SO₄(aq).¹⁵² Gas evolution at upward-facing electrodes consistently led to increased $m_{\text{Fe(II)}}$ relative to a stagnant electrolyte. Such behavior is consistent with previous measurements of the oxygen-evolving behavior of polished Ni foils.¹⁵³ The redox-active tracer used herein was present in concentrations that were 100-times more dilute than the concentration of OH⁻ in the cell, but yielded mass-transport-limited $j_{\text{Fe(III)}}$ values only 10-times less than J_{ph} required for a 10% efficient solar fuels device.¹¹⁵ This behavior suggests that the formation and departure of O₂ bubbles on upward-facing photoanodes generates sufficient convection to sustain device operation in unstirred electrolytes.

Mutually similar $m_{\text{Fe(II)}}$ values were observed at upward-facing planar, μW 6|14, and μW 6|28 photoanodes (**Figure 7.3D-F**), despite the variation in the number density and radii of bubbles in the gas-layers. The dependence of mass-transport velocities only on the volumetric flow rate of gas, and not the size or distribution of gas bubbles. This is consistent with a fluid replacement model for bubble-generated microconvection.¹⁵³⁻¹⁵⁴ Mass-transport velocities were lower at downward-facing electrodes relative to upward-facing electrodes (**Figure 7.3C**), suggesting that the departure rate of gas bubbles from the surface is a controlling variable on the microconvection process. A consequence of this microconvection model is that electrodes that produce isolated streams of gas bubbles (**Figure 7.3D,E**) will poorly mix the solution, with a spatially nonuniform distribution of

reactants and products, potentially leading to undesirable pH gradients and efficiency losses. Increases in the density of microwires, from planar to $\mu\text{W } 6|28$ to $\mu\text{W } 6|14$, led to decreases in the radii of bubbles and an increased number of gas streams, which would be expected to lead to more uniform mass transport. Preexisting gas nuclei can also be added to the surface to ensure a more even distribution of passive microconvection.¹⁵⁵ To minimize concentration overpotentials and maximize the mass-transport velocity at the surface, solar fuels devices should maximize production of gas bubbles. In CO_2 reduction cells under nonconcentrated sunlight, the generation of highly reduced products such as C_2H_4 (12 e^- per mole) may not produce sufficient gas flow rates to eliminate the need for external convection at that electrode surface.

The low gas coverages and minimal decreases in J_{ph} in stagnant electrolytes observed for upward-facing Si photoanodes in 1.0 M $\text{KOH}(\text{aq})$ contrast with the previously reported behavior of side-facing or upward-facing planar Si photocathodes in $\text{H}_2\text{SO}_4(\text{aq})$, which exhibited higher coverages of larger bubbles than observed herein.^{143, 145} The surface chemistry of planar photoelectrodes influences the gas coverage and consequently affects J_{ph} . The shape and departure diameter of a bubble is controlled by the adhesive forces at the solid/gas interface. The differences in R_b and θ_b between upward-facing photocathodes and photoanodes observed herein are not explained by differences in the surface free energy; both the hydrated $\text{Ni}(\text{OH})_2/\text{NiOOH}$, which forms during photoanodic operation in 1.0 M $\text{KOH}(\text{aq})$, and clean noble metal surfaces, are expected to act as wettable, high-energy surfaces.¹⁵⁶⁻¹⁵⁷ However, a monolayer of carbon contamination is sufficient to increase the hydrophobicity of a metal surface, and non-wetting behaviors have been reported at Au and Pt.¹⁵⁸ Rigorous cleaning may be required to observe similar nucleation

rates at Si coated with a uniform layer of Pt. Hydroxyl terminated Si, Si/OH, is wettable and thus is expected to exhibit bubble contact angles approaching 180°.

7.3.2 Upward facing p-Si Photocathodes in 0.50 M H₂SO₄(aq)

To evaluate the gas-evolving behavior in the absence of the Ni catalyst and TiO₂ protection layers, upward-facing photocathodes prepared from planar p-Si that was either cleaned to a SiO_x/OH surface or to a Si-H surface were used as hydrogen-evolving photocathodes in 0.50 M H₂SO₄(aq). Photoanodes prepared from bare Si rapidly formed passivating SiO_x under anodic conditions. The *J*-*E* behaviors of upward-facing planar p-Si/OH and p-Si/H photocathodes in 0.50 M H₂SO₄(aq) were recorded using linear sweep voltammetry at 200 mV s⁻¹ (**Figure 7.4A**). **Figure 7.4B** presents the time-dependent behavior of *J*_{ph} at upward-facing p-Si photocathodes maintained at *E* = -2.2 V vs RHE, which produced light-limited cathodic current densities. *J*_{ph} at upward-facing planar p-Si/OH electrodes was nearly identical to *J*_{ph}^{bare}, consistent with the absence of surface-attached gas bubbles (**Figure 7.4C**). In contrast, an upward-facing p-Si/H photocathode exhibited up to a 10% reduction to *J*_{ph} concurrent with a substantial coverage of gas bubbles on the electrode surface. The radius and coverage of gas bubbles at p-Si/H photocathodes decreased with time, and was accompanied by a gradual increase in *J*_{ph}.

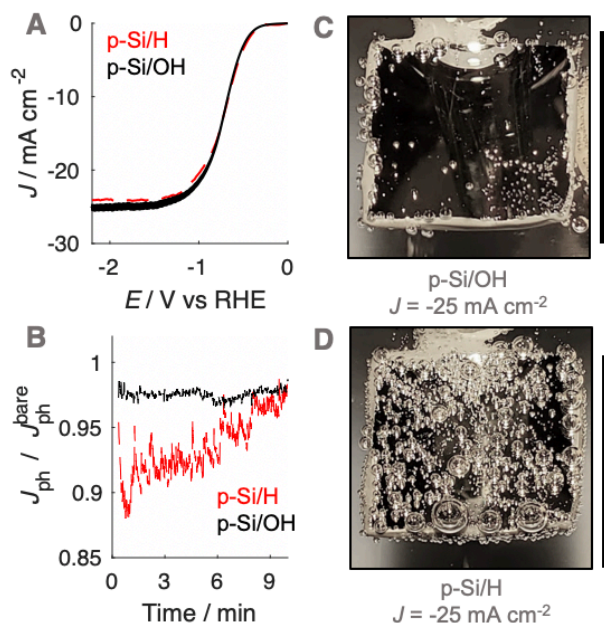


Figure 7.4: (A) J - E behavior for upward-facing p-Si photocathodes in stagnant 0.50 M $H_2SO_4(aq)$ recorded at 200 mV-s under illumination from an ELH lamp. (B) J - t behavior for photoanodes in (A) at -2.2V vs RHE in 0.50 M $H_2SO_4(aq)$. Top-down photographs of the (C) RCA-cleaned and (D) HF-cleaned planar p-Si photocathode shown in (B). Scale bars represent 1 cm.

A substantial reduction in the gas coverage was observed for hydroxyl-terminated upward-facing p-Si surfaces in 0.50 M $H_2SO_4(aq)$ relative to hydride-terminated surfaces. This observation is consistent with heterogeneous nucleation rate models that include a dependence on the contact angle of the initial nuclei, because surfaces with $\theta_b \sim 180^\circ$ are not catalytic for heterogeneous nucleation.¹⁵⁹ (100)-oriented Si surfaces terminated with Si-H bonds, following exposure to HF(aq), exhibit an advancing contact angle of $> 70^\circ$,¹⁶⁰ and p-Si photocathodes dipped in HF exhibited gas coverages and J_{ph} losses in 0.50 M $H_2SO_4(aq)$ that were comparable to those of Si coated with Ti/Pt.¹⁴⁵ For planar solar fuels devices that utilize a noble metal catalyst layer such Au or Pt, small R_b and θ_b values, approaching 180° , may be obtained after careful cleaning of such electrodes. Upward-

facing polished Pt foils primarily produced bubbles $< 100 \mu\text{m}$ in diameter after three days of continuous cathodic current flow in $1.0 \text{ M H}_2\text{SO}_4(\text{aq})$. Microstructuring or micropatterning can alleviate the deleterious effects of gas bubbles produced by non-optimal surface chemistry. Hence the results described herein are consistent with prior reports that the capillary forces within Si μW arrays, attributed to the more frequent release of small bubbles, lead to stable (photo)electrochemical performance in the absence of external convection.^{151, 161} Patterned catalyst islands surrounded by a hydrophilic, passivating metal oxide layer could also result in increased wettability and decreased departure diameters for gas bubbles on upward-facing electrodes.

7.3.3 Ray-Tracing Simulations of Surface Attached Bubbles

Figure 7.5 summarizes the results of ray-tracing simulations of the optical characteristics of bubbles attached to crystalline-Si electrodes under 630 nm , unpolarized light. **Figure 7.5A** presents the theoretically predicted (*) light-limited photocurrent density, $J_{\text{ph}}^*(r)$ as a function of the radial position, r , for a ray of infinitesimal thickness normalized to $J_{\text{ph}}^*(r)$ predicted at a solid/liquid interface at normal incidence, $J_{\text{ph}}^{\text{bare}}$. A global minimum in $J_{\text{ph}}(r)$ should occur in a narrow ring at which total internal reflection at the liquid/gas interface directs rays away from the absorber. In contrast, a wider, local minimum in $J_{\text{ph}}(r)$ should occur for rays incident on the region above the solid/gas interface (**Figure 7.6**). Bubbles with a large contact angle, θ_b , (**Figure 7.6**) minimize the area of the solid/gas interface and should consequently reduce the magnitude of optical losses resulting from gas coverage. The simulations indicated a global maximum in $J_{\text{ph}}^*(r)$ observed for bubbles with $\theta_b = 160^\circ$, but not with $\theta_b = 120^\circ$, due to a large number of reflections in the water layer adjacent to the solid/gas interface. Reductions in J_{ph} primarily

result from reflections at the solid/gas interface, because reflected and refracted rays at the liquid/gas interface are predominately directed downwards towards the absorber.

The simulations also revealed that gas bubbles should produce a substantial redistribution of photogenerated carriers in the electrode (**Figure 7.5B**). Bubbles act as diverging lenses that should reduce the local J_{ph} but increase J_{ph} at locations removed from the bubble radius (**Figure 7.6A**). The highest regions of increased photocurrent were directly beyond the projected radius of a surface-attached bubble, with complementary effects for neighboring bubbles (**Figure 7.6B**). The sum total effect of gas films that contained multiple bubbles was simulated by line-scans over a 1 cm wide absorber, while varying the total coverage by bubbles having a uniform size and shape. Bubbles with larger values of θ_b minimized the area of the solid/gas interface for an equivalent projected surface coverage, producing values of $J_{\text{ph}}^*(r)$ close to $J_{\text{ph}}^{\text{bare}}$ (**Figure 7.5C**). Larger bubbles scattered light from a greater distance from the absorber surface and thus led to increased optical losses relative to an equivalent surface coverage of smaller bubbles (**Figure 7.5D**). However, gas coverages ≤ 0.5 produced a $< 10\%$ reduction in simulated J_{ph} values.

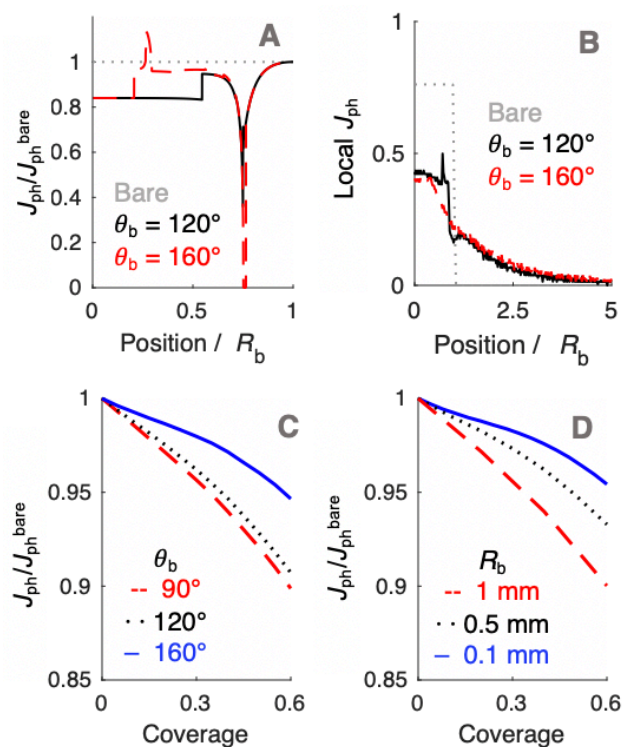


Figure 7.5: (A) Simulated $J_{ph}^*(r)$ profile at a single bubble, for varied θ_b , normalized to the simulated J_{ph}^{bare} at the bare solid/liquid interface. (B) Distribution of $J_{ph}^*(r)$ as measured via binned light absorption during ray-tracing simulations. The absorption is recorded as a function of position and the signal at individual bins was normalized to the total power incident on each bin in the absence of reflections or refractions. (C) Total J_{ph}^* at a 1 cm wide electrode as a function of gas coverage for bubbles with $R_b = 250 \mu\text{m}$ and various values of θ_b . (D) Total J_{ph}^* at a 1 cm wide electrode as a function of gas coverage of bubbles with $\theta_b = 160^\circ$ and various values of R_b .

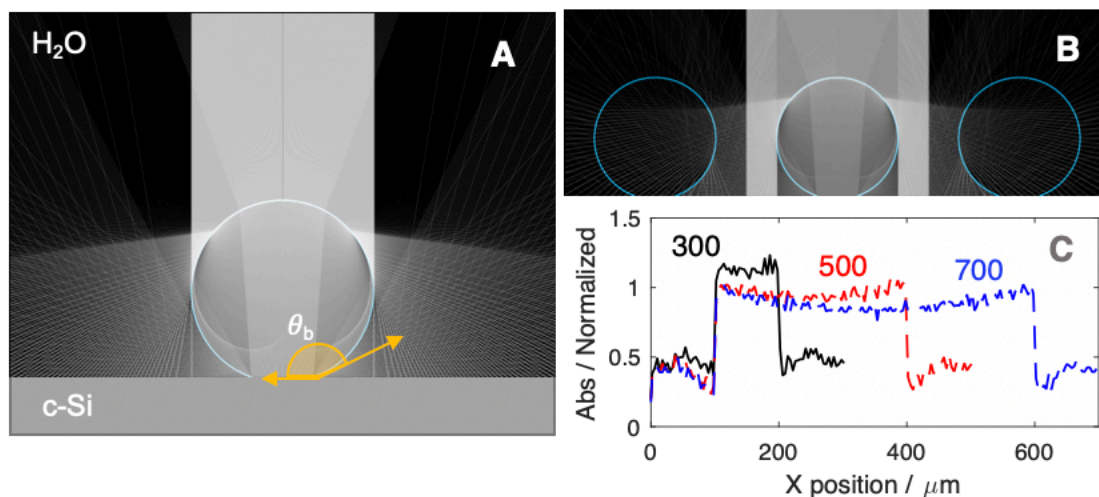


Figure 7.6: (A) Results of a ray-tracing simulation at a single surface-attached gas bubble, with $\theta_b = 160^\circ$, on crystalline silicon, illuminated by 630 nm unpolarized light, with liquid water as the surrounding medium. (B) Ray-tracing simulation for multiple, surface-attached gas bubbles with $\theta_b = 160^\circ$. (C) Absorption distribution at a surface containing bubbles with $R_b = 100 \mu\text{m}$ and $\theta_b = 160^\circ$ for varied center to center distances, recorded as a function of position. The absorption at individual positions, as bins, was normalized to the total power incident on each bin in the absence of reflections or refractions.

The close agreement between line scans of $J_{\text{ph}}^*(r)$ simulated in this work and previously reported $J_{\text{ph}}(r)$ line scans measured experimentally using scanning-photocurrent microscopy demonstrates that ray-tracing simulations are an accurate method for simulating the optical properties of bubbles that have diameters substantially larger than a wavelength of light.¹⁴⁵ Although the shape of surface-attached bubbles can be expected to affect the spatial propagation of off-incident illumination (**Figure 7.5B**), J_{ph} should be close to $J_{\text{ph}}^{\text{bare}}$ if R_b is small with respect to the electrode width (**Figure 7.5D**). Refracted rays are not scattered far from a bubble and can moreover produce an increase in collection efficiency relative to the absorption at a bare-Si/liquid interface (**Figure 7.5A**). **Equation**

7.2 gives the scattering distance, s , for a ray at position r undergoing total internal reflection as a function of the bubble radius, R_b , and θ_b :

$$s = R_b \left[\frac{2r\sqrt{1-r^2}}{2r^2-1} (\sqrt{1-r^2} - \cos \theta_b) \right] \quad (7.2)$$

where r has been normalized to represent the non-dimensional distance from the bubble center (**Figure 7.7A**). For a bubble with $\theta_b = 160^\circ$, the maximum scattered distance exceeds $10 R_b$ for the ring of light incident on $r \leq 0.76$ (**Figure 7.7B**). This region constitutes the global minimum observed in **Figure 7.5A**. The formation of gas bubbles with small radii on the surface serves two purposes in minimizing optical losses: (i) the maximum scattering distance is maintained within the width of the electrode and (ii) the projected area of the reflective ring on the solar flux plane is kept small. Anti-reflective layers and surface texturing could further minimize the optical losses at the gas/solid interface.¹⁶²

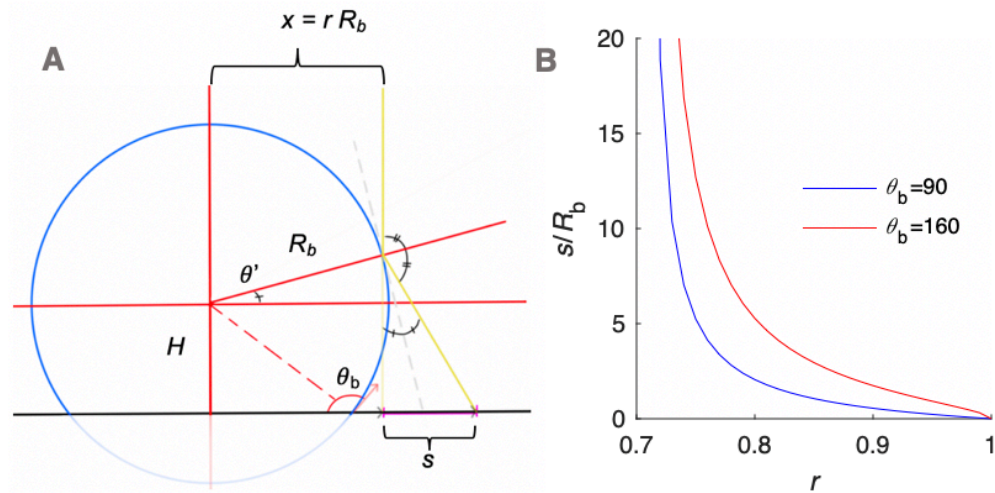


Figure 7.7: (A) Graphical representation of **Equation 7.2**. (B) Non-dimensionalized plot of the scattering distance (s/R) versus the ray position ($r = x/R$) for bubbles with $\theta_b = 90^\circ$ and 160° .

7.2.4 Downward-Facing Photoelectrodes

To quantitatively evaluate the optical effects of static gas bubble films at the photoelectrode surface while controlling for the effect of departing gas bubbles in the electrolyte layer, the photoelectrochemical characteristics of downward-facing electrodes were investigated using 630 nm illumination (**Figure 7.8**). The gas coverage was measured from photographs and was compared against the instantaneous J_{ph} value determined directly before the gas coverage measurement (**Figure 7.8F-G**). Mutually equivalent rates of gas production were obtained by maintaining $J_{\text{ph}}^{\text{bare}}$ at -5 mA cm^{-2} for photocathodes (2 e- H_2 production) and at 10 mA cm^{-2} for photoanodes (4 e- O_2 production). Downward-facing planar and μW p-Si photocathodes exhibited larger bubble coverages than downward-facing n-Si/TiO₂/Ni photoanodes (**Figure 7.8A-B**). A maximum coverage of 0.57 was observed at downward-facing electrodes in 0.50 M H₂SO₄ with a minimum $J_{\text{ph}}/J_{\text{ph}}^{\text{bare}}$ of 0.80 and 0.81 observed at p-Si and n⁺p-Si/Ti/Pt electrodes, respectively (**Figure 7.8A**). The minimum $J_{\text{ph}}/J_{\text{ph}}^{\text{bare}}$ value at downward-facing planar and μW 6|14 n-Si/TiO₂/Ni photoanodes was 0.96 and 0.94, respectively (**Figure 7.8B**).

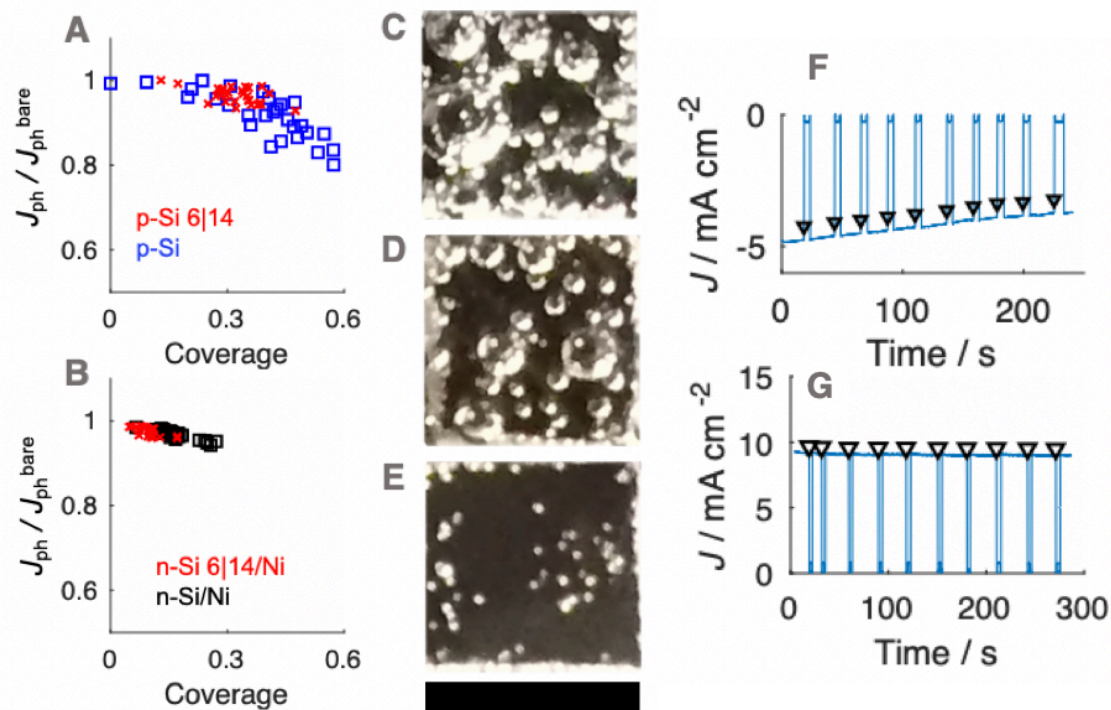


Figure 7.8: Coverage vs $J_{\text{ph}}/J_{\text{ph}}^{\text{bare}}$ for downward-facing hydrogen-evolving photocathodes in 0.50 M $\text{H}_2\text{SO}_4(\text{aq})$ (A) and oxygen-evolving photoanodes in 1.0 M $\text{KOH}(\text{aq})$ (B). (C-E) Representative images of planar p-Si (C), μW 6|14 p-Si (D), and n-Si/Ni (E). Scale bars represents 5 mm. (F) J - t behavior of an inverted p-Si/H electrode under chopped illumination. The light source was turned off and an image was recorded under diffuse light at times marked with arrows. (G) J - t behavior of an inverted n-Si 6|14 electrode under chopped illumination.

The dependence of $J_{\text{ph}}/J_{\text{ph}}^{\text{bare}}$ on the gas coverage (**Figure 7.8A-B**) was in agreement with simulated $J_{\text{ph}}/J_{\text{ph}}^{\text{bare}}$ data vs coverage data for 2D line scans at coverages < 0.4 (**Figure 7.5C-D**). At the highest gas coverages, the experimentally measured $J_{\text{ph}}/J_{\text{ph}}^{\text{bare}}$ values were lower than the $J_{\text{ph}}/J_{\text{ph}}^{\text{bare}}$ values predicted by simulation, concurrent with the presence of the largest gas bubbles. The simulated gas coverages, however, assumed an even distribution of gas bubbles across the surface, whereas in practice gas bubbles tended

to aggregate and were more often found near the edges of the electrode, which could increase the amount of light scattered away from the absorber. Differences in the shape of larger bubbles due to hydrostatic pressure could also influence the measured optical effects, but such effects are not expected to be relevant to the optical properties of bubbles at upward-facing electrodes.

The simulations described herein assumed that only bubbles that are large with respect to the wavelength of light contributed substantially to optical losses in photoelectrochemical cells, such that ray-optical treatment was sufficient to describe their optical properties. This assumption is justified by the $R \sim t^{1/2}$ dependence of bubble growth, such that bubbles spend a short time as small nuclei but spend a relatively long time close to the R_b at which the bubbles leave the surface.¹⁶³ The simulations in this work do not treat interference effects and will underestimate the effective scattering radius of small bubbles.¹⁶⁴ These effects could be important for solar fuels devices that generate a large number of small gas nuclei due to operation under concentrated sunlight.

The dominant optical effect of gas bubbles is the spatial redistribution of photogenerated carriers across the semiconductor surface. The deleterious effects of bubbles on the efficiency of small-scale photoelectrochemical solar fuels devices suitable for research-scale measurements cells are not present on larger-scale electrodes.¹²⁶ Solar fuels devices using a conductive emitter layer will redistribute carriers across the equipotential top surface such that bubbles will not affect the local J_{ph} .¹⁶⁵ Gas bubbles that are much smaller than the carrier-collection length of a semiconductor are unlikely to influence the spatial distribution of J_{ph} because photogenerated carriers will redistribute to minimize the overpotential at individual catalyst sites. Large gas bubbles on membrane-

embedded, electrically isolated microcells will have more substantial effects on the device efficiency if cells operating under less than 1-Sun illumination do not generate sufficient photovoltage to drive the full-cell reaction. Gas bubbles that adhere to micropatterned catalyst sites will direct light away from the catalyst, which could lead to beneficial increases in the total J_{ph} .

7.4 Conclusions

Simulations and experimental data confirm that forward-scattering optical effects of bubbles do not affect the total J_{ph} of a photoelectrochemical cell if R_b of the bubbles are kept small prior to departure from the surface. Careful preparation of metal and semiconductor surfaces could lead to θ_b approaching 180° , which will also minimize R_b . Solar fuels device designs should thus seek to maximize the wettability of the top-facing photoelectrode surface via control of the surface chemistry and/or microstructure, to obviate the need for surfactants such as Triton X-100 in the electrolyte.²¹ Planar and microstructured n-Si/TiO₂/Ni photoanodes, $\sim 1 \text{ cm}^2$ in area, exhibit gas coverages characterized by small R_b and large θ_b , and such devices exhibited minimal changes to J_{ph} during operation under 1 Sun equivalent illumination. Although the gas coverage increased substantially as the illumination intensity increased, J_{ph} remained stable with time. Gas evolution at upward-facing photoanodes in 1.0 M KOH(aq) led to increased mass-transport velocities compared to a stagnant electrolyte, and produces minimal concentration overpotentials adequate to facilitate efficient solar fuels device operation under non-concentrated sunlight, thereby eliminating the need for external convection

APPENDIX

A.1 General Experimental Methods

Materials: All solutions were diluted with water obtained from a Millipore deionized (DI) water system, having a resistivity of 18.2 M Ω ·cm. Fumasep FAAM-15 and Nafion™ 117 were obtained from Fuel Cell Store. Sulfuric Acid (TraceMetal Grade) and potassium hydroxide (99.99%, semiconductor grade) were purchased from Fisher. Ammonium hydroxide (28 – 30 %) was purchased from JT Baker and hydrogen peroxide (ACS reagent, 30%) was obtained from Macron. Buffered oxide etchant (6:1 (v/v) 40% NH₄F to 49% HF) was obtained from Transene. Cobalt(II) chloride hexahydrate (CoCl₂, >99.9%) and gallium-indium eutectic (GaIn, 99.99%, metals basis) were obtained from Alfa Aesar.

Cleaning: In general Si samples were cleaned in a Radio Corporation of America, RCA, “Standard Clean 1” SC1 bath (5:1:1 H₂O/NH₄OH/H₂O₂, 80 °C for >10 min), buffered oxide etchant (10 s for planar samples and 5 min for wire samples at 20 °C), and an RCA “Standard Clean 2” SC2 bath (6:1:1 H₂O/HCl/H₂O₂, 70 °C for >10 min) to remove SiO₂, Al₂O₃ and trace metal impurities.

Homojunction preparation: Immediately after cleaning of the samples followed by oxide removal in HF(aq), n⁺ doping of silicon chips was performed in a quartz tube under 10 liters per minute N₂ flow at 850°C with two PH-900 PDS wafers (Saint Gobain) serving as the P source. The P₂O₅ glass formed during the doping procedure was removed from the Si surface via buffered oxide etchant for > 60 s.

Preparation of Si Microwire Arrays: Si was degreased with acetone and isopropyl alcohol and was then spin coated at 4000 rpm for 30 s with Shipley 1813 photoresist. A square array of circles was defined using UV exposure through a chrome mask. The pattern

was developed with MF-319 developer, and the resist was hard-baked at 115 °C for 10 min. Al₂O₃ masks, 125 nm in thickness, were deposited via e-beam evaporation at 1 Å·s⁻¹ into the exposed hole array and the resist was removed via sonication in Remover-PG (MicroChem) at 50 °C. Si was structured into 30 μm tall microwire arrays via deep reactive ion etching (RIE) in a SF₆/O₂ plasma controlled by an Oxford Plasmalab System 100 at -130 °C. An inductively coupled plasma power of 900 W produced etching rates of 1 μm min⁻¹, while a low capacitively coupled plasma power of 3-7 W minimized sidewall damage and mask removal.

Physical Characterization: Scanning-electron micrographs (SEMs) were obtained with a FEI Nova NanoSEM 450 at an accelerating voltage of 5.0-15.0 kV and a working distance of 5.0 mm using an Everhart-Thornley secondary electron detector.

A.2 Supporting Information for Chapter 2

Materials: 100mm P-type Si <100> wafers with a thickness of 525 μm and resistivity of 10-20 Ω-cm were obtained from Addison Engineering. All chemicals were commercially available and used as received. Sodium hypophosphite monohydrate (NaPO₂H₂), boric acid (H₃BO₃, >99.5%), concentrated ammonium hydroxide (NH₄OH, ACS reagent 28%-30%) and potassium hydroxide (KOH, 99.99%) were obtained from Sigma-Aldrich. Buffered oxide etchant (6:1 (v/v) 40% NH₄F to 49% HF) was obtained from Transene Inc. Sodium chloride (NaCl, 99%) was obtained from Macron Chemicals.

A.3 Supporting Information for Chapter 3

Materials: Isopropyl alcohol, acetone, hydrochloric acid (36.5 - 38.0 %), and nitric acid (67 - 70 %, TraceMetal Grade) were purchased from Millipore, and CuSO₄ was purchased from Flinn Scientific. K₂SO₄ (99 %), and potassium bicarbonate (99.995 %) were

purchased from Sigma-Aldrich. Methanol was purchased from VWR Chemical. Buffered oxide etchant (6:1 $\text{NH}_4\text{F}/\text{HF}$) was purchased from Transene. Boron doped, P-type silicon wafers with a resistivity of 10 - 20 $\Omega\cdot\text{cm}$ were purchased from Addison Engineering. Platinum foil (99.99 %) was purchased from Alfa Aesar, and copper foil (99.999 %) was obtained from Sigma Aldrich. CO_2 (99.999 %, <1.0 ppm $\text{Ar}+\text{O}_2+\text{CO}$, <1.0 ppm THC, <3.0 ppm H_2O , <5.0 ppm N_2) was purchased from Airgas.

(Photo)electrodepositions of Catalyst: Prior to electrodeposition of Cu, electrodes were rinsed sequentially with acetone, isopropyl alcohol, methanol, and deionized water and then dipped into buffered oxide etchant for 60 s. Electrodepositions were controlled with a BioLogic SP-200 potentiostat. The Cu-plating bath was continuously purged with $\text{Ar}(\text{g})$ and contained 0.10 M $\text{CuSO}_4(\text{aq})$, 5.0 mM $\text{H}_2\text{SO}_4(\text{aq})$, and 0.10 M $\text{K}_2\text{SO}_4(\text{aq})$, at a pH of ~ 3 . A saturated calomel electrode (SCE, CH Instruments) was used as a reference and the counter electrode was a high-purity graphite rod (Alfa Aesar, 5N) (**Figure 3.1A**). The illumination source was an array of narrowband light-emitting diodes (Luxeon Rebel Blue SMD, FWHM 22 nm) with a peak intensity at 465 nm. The illumination wavelength was selected to maximize transmission of light through the colored electrolyte. Cu was deposited potentiostatically at 0.0 V vs. SCE until the desired charge density had passed, normalized to the projected area of the electrode.

Photoelectrochemical CO_2 Reduction Testing: The electrochemical setup was operated in a continuous flow mode. Carbon dioxide was provided to the electrochemical cell at a flow rate of 5 sccm as controlled by an Alicat flow controller. The carbon dioxide stream was supplied as humidified CO_2 with a gas bubbler placed between the cell and flow controller. The exhaust gases went through a liquid trap, then an Alicat flow meter, and

finally to a gas chromatograph (SRI-8610) using a Hayesep D column and a Molsieve 5A column with N₂ as the carrier gas. The gaseous products were detected using a thermal conductivity detector (TCD) and a flame ionization detector (FID) equipped with a methanizer. Quantitative analysis of gaseous products was based on calibrations with several gas standards over many orders of magnitude in concentration. The calibrations were used to calculate the partial current density, j , towards products of the CO₂R and hydrogen evolution reaction. To measure liquid products, the electrolyte on the anode and cathode sides of the cell was sampled at the end of the run and was analyzed by high-performance liquid chromatography (HPLC, Thermo Scientific Ultimate 3000). Products were not quantified in Faradaic efficiency calculations because continuous purging of the catholyte with CO₂ expelled accumulated products. Moreover, crossover of products to the anolyte was observed and oxidation at the anode could potentially occur. An Oriel Instruments 75 W Solar Simulator supplied 100 mW·cm⁻² of AM 1.5 illumination. The light intensity was calibrated using the measured photocurrent at a calibrated (350 to 1100 nm, 1 cm²) NIST traceable Si photodiode (Thorlabs FDS1010-CAL) mounted within the testing cell prior to the addition of the electrolyte.

Electrochemical measurements of photoelectrochemical CO₂R: A PEEK compression cell was used as the vessel for the measurement with an anode chamber volume of 2 mL and a cathode chamber volume of 4 mL. The anode, cathode electrode and membrane area were each 1 cm² as constrained by the design of the compression cell. CO₂ saturated 0.10 M potassium bicarbonate (KHCO₃, pH 6.8) was used as the electrolyte. A Pt foil anode was used behind a Selemion anion exchange membrane. A leakless Ag/AgCl electrode was used as a reference. All electrochemical measurements were performed using

a Biologic VSP-300 potentiostat. Scan rates were set to $50 \text{ mV}\cdot\text{s}^{-1}$. Cu foil (99.999 %, Sigma Aldrich) was mechanically polished (Struers LabPol-5) using $0.050 \text{ }\mu\text{m}$ alumina suspension (MasterPrep) and then was electropolished for 5 min in 85% H_3PO_4 at +2.1 V vs. a carbon counter electrode.

Comparison of Catalyst Loadings: The mass loadings of catalyst were compared assuming a Faradaic efficiency of $\sim 100 \%$ towards metal plating. Equation S1 can be used to calculate the mass loading density, M_{cat} ($\text{mg}\cdot\text{cm}^{-2}$), from the cathodic charge density, $-Q$ ($\text{C}\cdot\text{cm}^{-2}$) and molar mass of the catalyst. For Cu ($m_a = 63.55 \text{ g}\cdot\text{cm}^{-2}$), M_{cat} was 0.329 and $0.0487 \text{ mg}\cdot\text{cm}^{-2}$ for $-Q = 1$ and $0.148 \text{ C}\cdot\text{cm}^{-2}$, respectively.

$$M_{cat} = \frac{-Qm_a}{nF} \quad (\text{S1})$$

Explanation of Resistance Measurement and iR_s Correction: The resistance (R_s) was determined by electrochemical impedance spectroscopy (EIS) at the open-circuit potential. During the experiment, iR_s was corrected by 85% and the remaining 15 % was corrected for after the experiment.

Measurements of Pt Crossover during Stability Testing The rate of Pt dissolution in $0.10 \text{ M KHCO}_3(\text{aq})$ and crossover through Selemion were measured via a galvanostatic experiment at 10 mA using a Pt anode and a graphite cathode. The volumes of the anolyte and catholyte were each 13 mL . ICP-MS measurements confirmed the presence of dissolved Pt in both the anolyte and catholyte.

Predicted j - E behavior: Illuminated j - E behavior was predicted by shifting the fitted Tafel behavior of the polished Cu foil towards positive potentials by $V_{\text{ph}} + b \log_{10}(R_{\mu})$. This calculation assumes a comparable microstructured area of Cu islands and Si and similar $[\text{H}^+(\text{aq})]$ and $[\text{CO}_2(\text{aq})]$ at the surface of the two electrodes. Simulated j - E behaviors in

Figure 4b were produced by summing the implicit values for η and V_{ph} , calculated from Equations 1 and 2, as a function of R_μ and b . Arbitrary values for $J_0 = 1 \times 10^{-10} \text{ A cm}^{-2}$ and $a = 1 \times 10^{-7} \text{ A cm}^{-2}$ were selected; these parameters do not affect the potential shift resulting from a change in R_μ but affect the total V_{ph} and η observed.

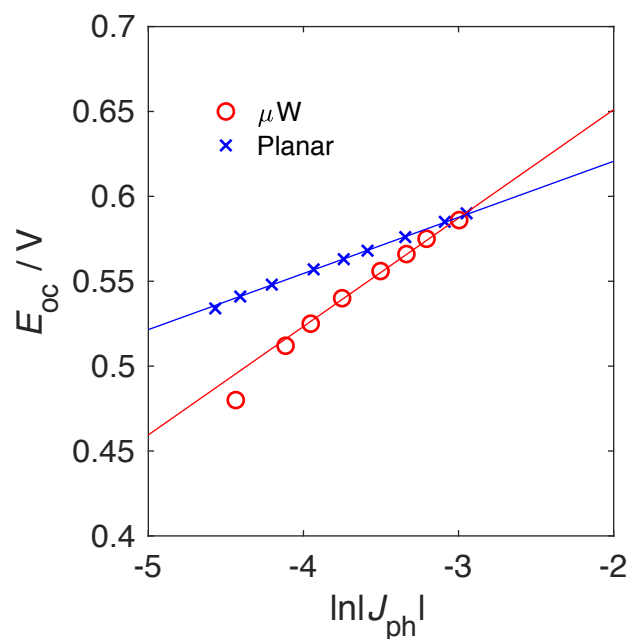


Figure A.3.1: Plot of E_{oc} vs. the \ln of the light-limited photocurrent density ($\text{A}\cdot\text{cm}^{-2}$) in a Cu plating bath for planar and μW n^+p -Si. The illumination source was a narrow band LED with a peak intensity at 630 nm. The illumination wavelength was selected to maximize transmission through the Cu film. The ideality factor was calculated from the slope of the linear fit in range of photocurrent densities relevant to operation under $100 \text{ mW}\cdot\text{cm}^{-2}$ of simulated sunlight.

A.4 Supporting Information for Chapter 4

Fabrication of n^+p -Si μ -cone photocathodes with Pt: Czochralski-grown p-type Si wafers with a $\langle 100 \rangle$ orientation and a resistivity of 0.60-0.80 $\text{ohm}\cdot\text{cm}$ (Addison Engineering, Inc.) were photolithographically patterned with a square grid of Al_2O_3 circles

that were 3 μm in diameter with a 7 μm pitch. The Al_2O_3 was deposited to a thickness of 200 nm via electron-beam evaporation. The μ -cones were etched from the masked p-Si wafer using an Oxford Dielectric System 100 ICP/RIE following a procedure described previously.¹¹⁹ A capacitively coupled power of 7 W, and an inductively coupled power of 900 W, was used for etching. Etching was performed in three steps, in which the ratio of SF_6 to O_2 gas was varied stepwise from 70 sccm : 6 sccm to 70 sccm : 7 sccm by increasing the rate of O_2 flow by 0.5 sccm every 30 min. The chamber temperature and pressure were maintained at -130°C and 10 mTorr, respectively. After etching, samples were cleaned via a modified RCA standard clean 1 (5:1:1 (vol) $\text{H}_2\text{O}:\text{NH}_4\text{OH}:\text{H}_2\text{O}_2$ at 70°C) followed by an RCA standard clean 2 (6:1:1 (vol) $\text{H}_2\text{O}:\text{HCl}:\text{H}_2\text{O}_2$ at 70°C). The samples were dipped in HF between the cleaning steps, which also resulted in removal of the Al_2O_3 etch mask. After cleaning, the samples were dipped in ~ 6.5 M HF(aq) for 1 min before thermal P diffusion using a Saint-Gobain PH-900 PDS diffusion-doping source at 850°C for 15 min under a $\text{N}_2(\text{g})$ ambient, to yield an n^+p homojunction. To reduce thermal stresses, the samples were inserted into, and removed from, the doping furnace over the course of 1 min. The Si μ -cones were then heated to 150°C on a hot plate, and mounting wax (Quickstick 135, South Bay Tech) was melted into the array as a mask. Excess wax was removed by reactive-ion etching using an O_2 plasma at a forward power of 400 W and 300 mTorr operating pressure. The wax was etched until 6-9 μm of the tips of the μ -cones were exposed. The samples were then dipped in ~ 6.5 M HF for ~ 1 min to remove the native oxide over the Si μ -cones, and Ti and/or Pt were sputtered onto the samples. The reproducible sputtering rate of the system allowed for the thickness to be controlled by the sputtering time and was referenced to a planar control wafer. Metal thicknesses on planar

samples were measured with a DektakXT Profilometer. The samples were then immersed in acetone and sonicated for 15 min to completely remove the wax, resulting in Si μ -cones with metal selectively deposited over the tips of the μ -cones. Samples were cleaved with a carbide scribe into ~ 10 mm² chips and electrodes were fabricated as described above (A.1)

Fabrication of p-Si μ -cone photocathodes with Co-P: p-Si μ -cone arrays were fabricated via the above etching and cleaning procedures but were not doped with an n⁺ emitter layer. Bottom-facing electrodes were made from the p-Si μ -cones as described in the previous section, and Co/Co-P was photoelectrochemically deposited onto the surface of the p-Si μ -cones using illumination from a narrowband light-emitting diode (LED) (Thorlabs) with an intensity-averaged wavelength of 625 nm. The light intensity at the surface of the sample was ~ 200 mW cm⁻². The Co/Co-P plating bath has been described elsewhere,²⁶ and was purged vigorously with Ar(g) prior to and during the deposition, with a gas stream in close proximity to the sample to drive local convection.

Fabrication of membrane-embedded p-Si μ -cone photocathodes with Co-P: p-Si μ -cones were embedded in PDMS by spin coating a 10:10:1 (vol) solution of toluene, PDMS elastomer, and curing agent (Dow SylgardTM 184) at 3000 rpm, leaving the top ~ 15 μ m of the μ -cones exposed. The samples were cured on a hot plate at 150 °C for ~ 30 min. The μ -cones were peeled off of the substrate using a razor blade. The flexible polymer membrane was held on its edges sandwiched between Kapton tape and a glass slide, with the back side of the μ -cones facing up. The thickness of the tape ensured that the tips of the μ -cones were not damaged. 500 nm of Au was deposited via electron-beam evaporation onto the backs of the μ -cones. Electrodes were made using these flexible substrates with

Ag ink connecting the Au back contact to a Cu-Sn wire that was fed through 6 mm outer diameter borosilicate glass tubing which was 1 mm thick. Electrodes were fabricated as described above (A.1)

Stability testing: Extended stability testing of n⁺p-Si/Ti/Pt and p-Si/Co-P μ -cone arrays was performed under nominally identical conditions as those used for photoelectrochemical testing, but with a Pt mesh electrode counter electrode behind a Nafion membrane (Fuel Cell Store). H₂ was bubbled through the electrolyte for the duration of the stability tests to maintain a dissolved concentration of H₂ in equilibrium with 1 atmosphere of H₂(g).

A.5 Supporting Information for Chapter 5

Materials: All chemicals were commercially available and used as received. Sodium hypophosphite monohydrate (NaPO₂H₂), boric acid (H₃BO₃, >99.5%), concentrated ammonium hydroxide (NH₄OH, ACS reagent 28%-30%), potassium hydroxide (KOH, 99.99%), and TraceCERT® standards for phosphorus (P 1000 mg/mL) and cobalt (Co 10 mg/mL) were obtained from Sigma-Aldrich. Hydrochloric acid (HCl, ACS grade 36.5-38%) was obtained from Millipore. P-type Si wafers with a resistivity of 10-20 Ω -cm and n-type Si wafers with a resistivity of <0.005 Ω -cm, both with diameters of 100 mm, thicknesses of 525 μ m, and <100> orientation, were obtained from Addison Engineering. Fluorine-doped tin oxide (FTO, NSG TEC™ 15) with dimensions of 25 x 100 x 2 mm and a sheet resistance of 14 Ω /□ was obtained from Pilkington. PH-900 PDS diffusion dopant source wafers were purchased from Saint-Gobain.

Metallization: Metallization occurred in an AJA high-vacuum magnetron sputtering unit under a constant flow of Ar at 20 standard cubic centimeters per minute, with the chamber

pressure maintained at 5 mtorr. Ti was deposited via radio-frequency (RF) sputtering at 130 W for 90 s whereas Co was deposited via RF sputtering for 90 s at 150 W.

Fabrication of Electrodes: Silicon electrodes were prepared from individual 5-20 mm² chips of metallized n⁺-Si and n⁺p-Si samples. Ohmic contacts were formed via scratching In-Ga into the backside of the chips. FTO electrodes were prepared from 20-30 mm² chips of metallized FTO samples. An adhesive Ag paint having a grain size < 1.0 μm (PELCO, Ted Pella) was used to affix the chips to a Cu-Sn wire that had been fed through 6 mm outer diameter borosilicate glass tubing that was 1 mm thick. Photoactive n⁺p-Si chips and FTO samples were sealed onto the end of the glass tubing using an opaque, insulating epoxy (Hysol 9460), whereas n⁺-Si samples used for ellipsometry were fixed to the tubing using clear nail polish, which facilitated removal of the samples from the electrode assembly prior to ellipsometric measurements.

(Photo)electrochemical Measurements: (Photo)electrochemical depositions and hydrogen-evolution testing were performed using a Biologic SP-200 potentiostat. Single-compartment glass cells were used for both deposition and testing, with a saturated calomel electrode serving as the reference electrode and a high-purity graphite rod (Alfa Aesar) serving as the counter electrode. The illumination source for depositions was a Thorlabs narrow-band light-emitting diode with a nominal wavelength of 625 nm. The performance of photocathodes for photoelectrochemical hydrogen evolution was measured in H₂-purged 0.50 M H₂SO₄(aq) under 100 mW cm⁻² of simulated AM1.5 illumination produced by a filtered Hg (Xe) lamp powered at 290 W. *In-situ* transmittance spectra of CoP were recorded using a Biologic VMP3 Multichannel potentiostat connected to a calibrated reference diode (Thorlabs FDS100-CAL) and lock-in amplifier. The illumination source

was a Xe lamp powered at 150 W. The illumination was passed through a monochromator controlled via LabView, and chopped at 10-15 Hz. Light was passed through catalyst films deposited on FTO and collected at the reference diode during electrochemical characterization. Transmittance data were calculated relative to the signal collected through a bare FTO electrode in the cell.

Activation of Electrodeposited CoP: As deposited CoP films were activated via exposure to 10 mL 0.50 M H₂SO₄ (aq) at room temperature under a standard atmosphere. after a specified exposure time. Samples were rinsed with deionized water and dried under a N₂(g) stream to prevent further etching of the film.

Physical characterization: Atomic-force micrographs were recorded with a Bruker Dimension Icon using Peak Force Tapping mode. The Peak Force amplitude and frequency were set to 150 nm and 2 kHz, respectively. For each tapping cycle, a force versus distance curve was recorded by the instrument and a feedback signal was based on the maximum force between the probe and sample. ScanAsyst-Air probes (Bruker) had a nominal tip radius of 2 nm.

Optical characterization: Optical constants were investigated by use of a variable-angle spectroscopic ellipsometer with a rotating analyzer (J.A. Woolam Co., Inc.). Measurements were recorded at an angle of incidence of 70° in 5 nm increments in wavelength over a range from 300 to 1100 nm. A model consisting of a Si substrate, a 1 nm Ti interlayer, and a user-defined “effective medium approximation”, EMA, layer composed of CoP and void regions was used to analyze the optical properties of the films as a function of thickness and time immersed in 0.50 M H₂SO₄(aq). A fixed set of optical constants was assumed for the metal fraction of the film, based on the average set of n and k values measured for CoP

films characterized prior to exposure to 0.50 M H₂SO₄(aq). Only the void fraction and depolarization factor were allowed to vary within an individual set of measurements, whereas the thickness was selected as a constant value that produced the lowest mean-square error (MSE) value across the individual measurements. Allowing for a graded index of refraction within the EMA layer improved the fit (lowered the MSE) but could not be independently verified and was therefore excluded from the model. Allowing the optical properties of the metal fractions to vary would have similarly improved the fit by providing additional degrees of freedom, but no independent measurements could be performed on continuous CoP films after exposure to acid. Hence, in the absence of direct physical data, the optical properties were assumed to be best approximated by those of the “as-deposited” film composition.

Measurement of corrosion products: Dissolved Co and P in 0.50 M H₂SO₄(aq) were quantified via inductively coupled plasma mass spectrometry, ICP-MS, as a function of time spent in acid under galvanostatic control at -10 mA cm⁻². The volume of the electrolyte was 50 mL. Samples were recorded by withdrawing 0.500 mL of electrolyte at specified time intervals, which were diluted to a volume of 5.00 mL with deionized water for analysis. To avoid interference from sulfur in the electrolyte, phosphorus was quantified in mass-shift mode by forming a PO⁺ species detected at a mass to charge ratio of 47. Concentrations were calculated by comparing ion counts to calibration curves prepared from certified standard solutions.

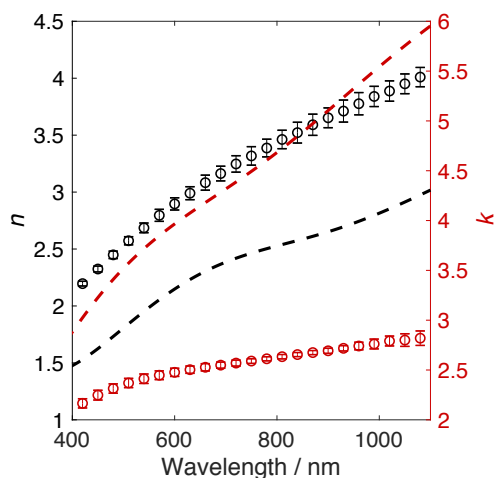


Figure A.5.1: Real (n) and imaginary (k) components of the complex index of refraction, measured via spectroscopic ellipsometry in air, for as-deposited CoP films deposited to a thickness of 87 ± 12 nm, represented as open circles. Error bars represent one standard deviation between three independent samples. For comparison, n and k values for an 80 nm Co film are plotted as dashed lines.¹³⁷

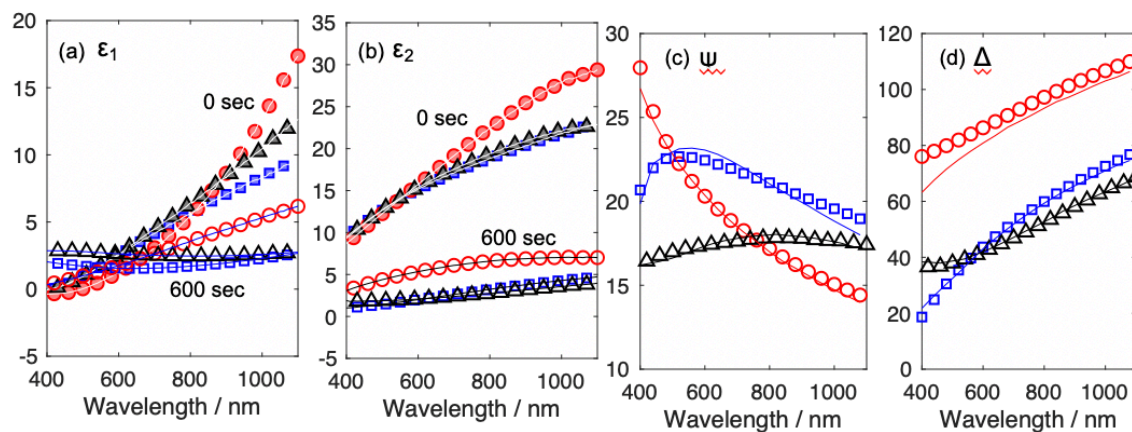


Figure A.5.2: Spectroscopic ellipsometry of n^+ -Si/Ti/Co/CoP samples at metal loadings of 400 (red circles), 800 (blue squares) and 1200 (black triangles) mC cm^{-2} . Measured data points are shown as individual markers, simulated data are represented as continuous lines (a) Real components and (b) Imaginary components of the dielectric functions of as deposited CoP films (filled markers) and films activated after 10 minutes of activation in 0.50 M $\text{H}_2\text{SO}_4(\text{aq})$ (open markers). (c) Comparison of simulated and measured values for parameter Psi. (d) Comparison of simulated and measured values for parameter Delta.

A.6 Supporting Information for Chapter 6

Materials: All chemicals were commercially available and used as received. Fe(II) sulfate heptahydrate (ACS Reagent, >99%), Fe(III) sulfate hydrate (97%) and 1,10-phenanthroline (>99%) were obtained from Sigma-Aldrich, gallium-indium eutectic (GaIn, 99.99%, metals basis) was obtained from Alfa Aesar, and concentrated ammonium hydroxide (NH₄OH, 28%-30%) was obtained from JT Baker. Hydrochloric acid (HCl, ACS grade 36.5-38%), acetone, and isopropyl alcohol were obtained from Millipore. Hydroxylamine sulfate (>98%) was obtained from TCI America. N-type Si wafers with a resistivity < 0.005 Ω-cm and diameters of 100 mm, thicknesses of 525 μm, and <100> orientation, were obtained from Addison Engineering.

Mass transport measurements: The thickness of the diffusion layer was measured via spectrophotometric determination of Fe²⁺ in a Shimadzu Solid Spec 3700 ultraviolet-visible spectrometer, following complexation with 1,10-phenanthroline in 0.50 M H₂SO₄(aq) and mixing the solution with 2.3 mL of 0.2 M sodium acetate (aq) to bring the pH to 4-4.5.¹⁶⁶ The testing cell was set up in a nominally identical manner to the cell used for HER testing, with the addition of 8.80 mL of 0.100 M Fe³⁺(aq), as Fe(III) sulfate, in 0.50 M H₂SO₄(aq) to the 50 mL electrolyte prior to testing to an initial $C_{Fe^{3+}}^* = 0.0150$ M. The precise concentration of the ferric sulfate stock solution was determined via spectrophotometry, following reduction with hydroxylamine, and assuming a molar extinction for tris(1,10-phenanthroline)iron(II) of 1.10×10^4 M⁻¹ cm⁻¹.^{1,2} A diffusion coefficient of Fe³⁺(aq) of 5.5×10^{-6} cm² s⁻¹ was assumed in calculating boundary layer thicknesses, assuming planar diffusion (Equation 5.1). The value of $C_{Fe^{3+}}^*$ was adjusted to

be the last recorded concentration of $\text{Fe}^{2+}(\text{aq})$, with the concentration of $\text{Fe}^{2+}(\text{aq})$ not changing by more than 4% during an individual electrolysis.

Calculations of Growth Coefficients: Radius versus time data for individual bubbles measured via high-speed microscopy were fit to a model for diffusive growth of a gas bubble in a supersaturated medium (**Equation A.6.1**).

$$R(t) = \tilde{b}(D_{\text{H}_2}t)^{1/2} \quad (\text{A.6.1})$$

where $D_{\text{H}_2} = 4.5 \times 10^{-5} \text{ cm}^2 \text{ s}^{-1}$ is the diffusivity of H_2 in solution and \tilde{b} is the dimensionless growth coefficient. When the driving force for bubble growth is small, the effects of advection at the growing surface can be ignored, such that analytical expressions can be derived relating \tilde{b} to $C_{\text{H}_2(\text{aq})}$. A self-consistent requirement for neglecting the effects of advection is that the Péclet number, which expresses the ratio of advective and diffusive growth, is < 1 . For $\tilde{b} > 1$ this condition does not hold and growth coefficients were thus not directly related to $C_{\text{H}_2(\text{aq})}$.

Calculation of Weighted Mean Bubble Diameter: The thickness of the gas bubble layer was variable in time and with position on the electrode surface. The mean bubble diameter, d , weighted by the fraction of surface obscured by an individual bubble, was calculated as an approximation of the instantaneous gas bubble layer thickness (**Equation A.6.2**).

$$\langle d_w \rangle = \frac{\pi}{A} \sum_i^n d_i \times \frac{d_i^2}{4} \quad (\text{A.6.2})$$

Where A is the geometric surface area of the electrode, the surface is assumed to be obscured by the projected area of the bubble, and the contact angle is assumed to be large such that the height of the bubble is approximately equal to the diameter.

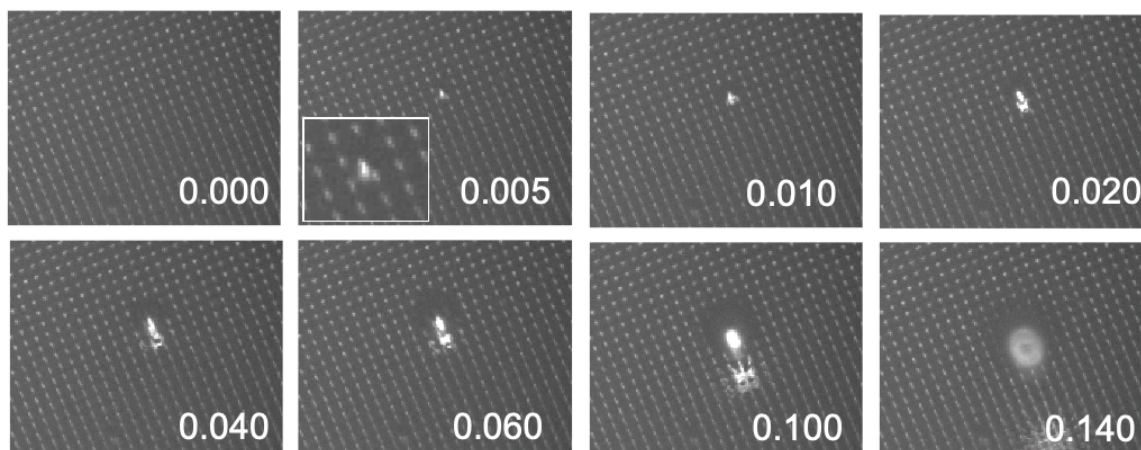


Figure A.6.1: Image sequence at 200 frames s^{-1} and 5-times magnification of an upward-facing μW 6|28 electrode passing 25 $mA\ cm^{-2}$ of current density for hydrogen evolution. Time stamps are referenced to the first frame and are in seconds. Inset image shows a $\sim 30\ \mu m$ bubble nucleus forming between microwires. Loss of focus at the bubble surface occurred due to the release from the electrode.

A.7 Supporting Information for Chapter 7

Materials: All chemicals were commercially available and used as received. Conductive Ni and Ag paint were obtained from Ted Pella. Hydrochloric acid (HCl, ACS grade 36.5-38%), acetone, and isopropyl alcohol were obtained from Millipore. Buffered oxide etchant (6:1 (v/v) 40% NH_4F to 49% HF) was obtained from Transene Inc and hydrogen peroxide (H_2O_2 , ACS grade 30%) was obtained from Macron Chemicals. Sulfuric acid (H_2SO_4 , TraceMetal grade) and potassium hydroxide (KOH, Semiconductor Grade) were obtained from Fisher Scientific. Concentrated ammonium hydroxide (NH_4OH , 28%-30%) was obtained from JT Baker. N-type Si wafers with a resistivity of 0.4 $\Omega\text{-cm}$ and p-type Si wafers with a resistivity of 10–20 $\Omega\text{-cm}$, having diameters of 100 mm, thicknesses of 525 μm , and $\langle 100 \rangle$ orientation, were obtained from Addison Engineering. Potassium

hexacyanoferrate(II) trihydrate ($\text{K}_4[\text{Fe}(\text{CN})_6] \cdot 3\text{H}_2\text{O}$, >99%) cyanide was obtained from Sigma-Aldrich.

Mass-transport velocity measurements: The current derived from oxidation of $\text{Fe}(\text{CN})_6^{4-}$ was calculated based on the change in absorptivity of the electrolyte in the cell before vs after a bulk electrolysis. The electrolyte was not stirred during testing but was vigorously stirred by a magnetically-powered Teflon stir bar prior to sampling the electrolyte. A calibration was performed at a large area Ni coil held potentiostatically at 1.3 V vs RHE. At this potential, the current associated with oxygen evolution was negligible and the current derived from $\text{Fe}(\text{CN})_6^{4-}$ oxidation was limited by mass transport. **Figure A.7.2** presents the change in absorptivity at 420 nm as a function of charge passed for a series of such experiments. The concentration of $\text{Fe}(\text{CN})_6^{3-}$ in the cell was calculated as Q / nFV where Q is the total charge passed at 1.3 V vs. RHE, n is the number of electrons required for the oxidation (1), F is Faraday's constant (96485 C mol^{-1}) and V is the volume of electrolyte in the cell during oxidation (0.097 L or 0.047 L for cells incorporating the upward-facing and downward-facing electrodes, respectively). The extinction coefficient of $1059 \text{ M}^{-1} \text{ cm}^{-1}$ was calculated from a linear regression of the measured absorbances and calculated concentrations.

Image processing: Images of downward-facing photoelectrodes were processed in MATLAB. The manually defined electrode area restricted the pixel area for data collection, and was used to calibrate the pixels per mm^2 scale at the electrode surface. The location and diameter of bubbles were recorded for each image, and the fractional coverage was calculated relative to the geometric electrode area. Manual quantification of bubbles was supplemented by automatic detection of similarly sized bubbles using a Hough transform.

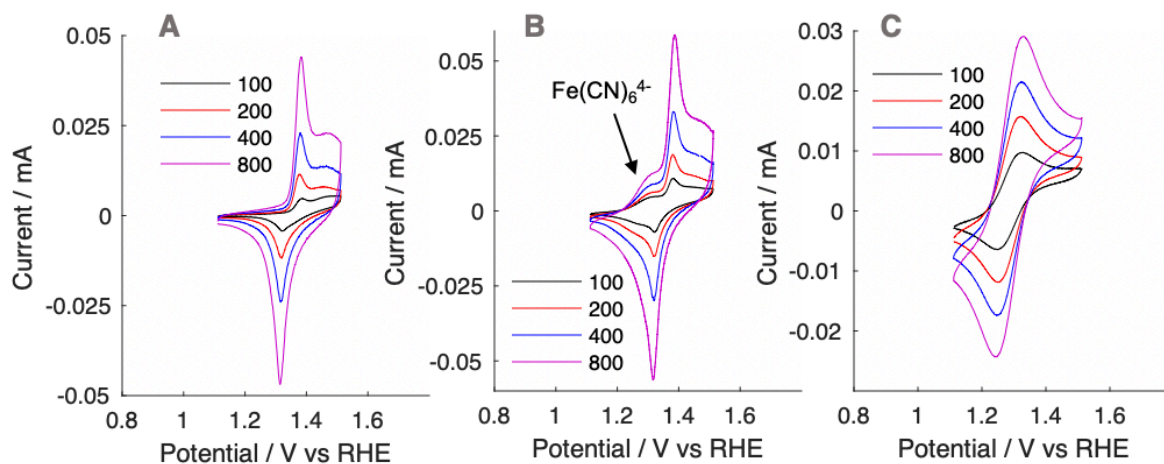


Figure A.7.1: (A) Cyclic voltammogram of a polished, 0.5 mm diameter Ni wire embedded in epoxy in 1.0 M KOH(aq). The scan rate is specified in mV s⁻¹. (B) Cyclic voltammogram of 10 mM Fe(CN)₆⁴⁻ in 1.0 M KOH(aq) at a polished, 0.5 mm diameter Ni wire embedded in epoxy. (C) Cyclic voltammogram of 10 mM Fe(CN)₆⁴⁻ in 1.0 M KOH(aq) at a Au wire embedded in borosilicate glass tubing.

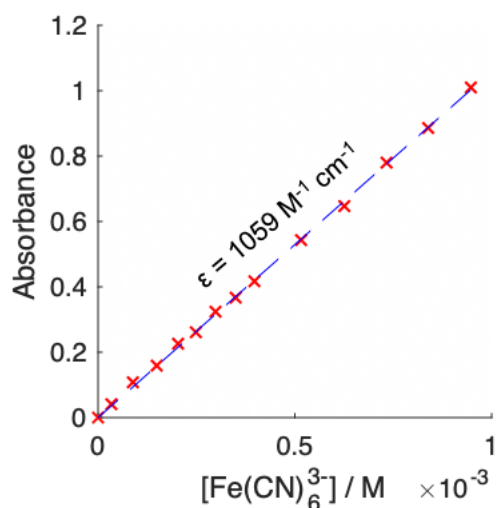


Figure A.7.2: Electrolyte absorbance at 420 nm versus [Fe(CN)₆³⁻] as measured via the anodic charge passed at a Ni wire in a solution of 10 mM Fe(CN)₆⁴⁻ in 1.0 M KOH(aq).

REFERENCES

1. Nations, U., Paris Agreement. Change, C., Ed. <https://unfccc.int/process-and-meetings/the-paris-agreement/the-paris-agreement>, 2015.
2. Sachs, J. D.; Schmidt-Traub, G.; Williams, J., Pathways to Zero Emissions. *Nature Geoscience* **2016**, *9* (11), 799-801.
3. Jenkins, J. D.; Luke, M.; Thernstrom, S., Getting to Zero Carbon Emissions in the Electric Power Sector. *Joule* **2018**, *2* (12), 2498-2510.
4. Lewis, N. S.; Nocera, D. G., Powering the Planet: Chemical Challenges in Solar Energy Utilization. *Proceedings of the National Academy of Sciences* **2006**, *103* (43), 15729-15735.
5. Smits, F. M., History of Silicon Solar Cells. *IEEE Transactions on Electron Devices* **1976**, *23* (7), 640-643.
6. Green, M. A., How Did Solar Cells Get So Cheap? *Joule* **2019**, *3* (3), 631-633.
7. Phillips, S. *Photovoltaics Report*; Fraunhofer Institute for Solar Energy Systems, ISE: 2020.
8. Vartiainen, E.; Masson, G.; Breyer, C.; Moser, D.; Román Medina, E., Impact of Weighted Average Cost of Capital, Capital Expenditure, and Other Parameters on Future Utility-Scale Pv Levelised Cost of Electricity. *Progress in Photovoltaics: Research and Applications* **2020**, *28* (6), 439-453.
9. Davis, S. J.; Lewis, N. S.; Shaner, M.; Aggarwal, S.; Arent, D.; Azevedo, I. L.; Benson, S. M.; Bradley, T.; Brouwer, J.; Chiang, Y.-M., Net-Zero Emissions Energy Systems. *Science* **2018**, *360* (6396).
10. Shaner, M. R.; Davis, S. J.; Lewis, N. S.; Caldeira, K., Geophysical Constraints on the Reliability of Solar and Wind Power in the United States. *Energy & Environmental Science* **2018**, *11* (4), 914-925.
11. Agency, I. E. Countries and Regions. <https://www.iea.org/countries>.
12. Clack, C. T.; Qvist, S. A.; Apt, J.; Bazilian, M.; Brandt, A. R.; Caldeira, K.; Davis, S. J.; Diakov, V.; Handschy, M. A.; Hines, P. D., Evaluation of a Proposal for Reliable Low-Cost Grid Power with 100% Wind, Water, and Solar. *Proceedings of the National Academy of Sciences* **2017**, *114* (26), 6722-6727.
13. Dowling, J. A.; Rinaldi, K. Z.; Ruggles, T. H.; Davis, S. J.; Yuan, M.; Tong, F.; Lewis, N. S.; Caldeira, K., Role of Long-Duration Energy Storage in Variable Renewable Electricity Systems. *Joule* **2020**.
14. McKone, J. R.; Lewis, N. S.; Gray, H. B., Will Solar-Driven Water-Splitting Devices See the Light of Day? *Chemistry of Materials* **2013**, *26* (1), 407-414.
15. Staffell, I.; Scamman, D.; Abad, A. V.; Balcombe, P.; Dodds, P. E.; Ekins, P.; Shah, N.; Ward, K. R., The Role of Hydrogen and Fuel Cells in the Global Energy System. *Energy & Environmental Science* **2019**, *12* (2), 463-491.
16. Shaner, M. R.; Atwater, H. A.; Lewis, N. S.; McFarland, E. W., A Comparative Technoeconomic Analysis of Renewable Hydrogen Production Using Solar Energy. *Energy & Environmental Science* **2016**, *9*, 2354-2371.
17. Nielander, A. C.; Shaner, M. R.; Papadantonakis, K. M.; Francis, S. A.; Lewis, N. S., A Taxonomy for Solar Fuels Generators. *Energy & Environmental Science* **2015**, *8* (1), 16-25.

18. Ager, J. W.; Shaner, M. R.; Walczak, K. A.; Sharp, I. D.; Ardo, S., Experimental Demonstrations of Spontaneous, Solar-Driven Photoelectrochemical Water Splitting. *Energy & Environmental Science* **2015**, *8* (10), 2811-2824.
19. Lewis, N. S., Developing a Scalable Artificial Photosynthesis Technology through Nanomaterials by Design. *Nature Nanotechnology* **2016**, *11* (12), 1010-1019.
20. Singh, M. R.; Clark, E. L.; Bell, A. T., Effects of Electrolyte, Catalyst, and Membrane Composition and Operating Conditions on the Performance of Solar-Driven Electrochemical Reduction of Carbon Dioxide. *Physical Chemistry Chemical Physics* **2015**, *17* (29), 18924-18936.
21. Khaselev, O.; Turner, J. A., A Monolithic Photovoltaic-Photoelectrochemical Device for Hydrogen Production Via Water Splitting. *Science* **1998**, *280* (5362), 425-427.
22. Vijselaar, W. J.; Perez-Rodriguez, P.; Westerik, P. J.; Tiggelaar, R. M.; Smets, A. H.; Gardeniers, H.; Huskens, J., A Stand-Alone Si-Based Porous Photoelectrochemical Cell. *Advanced Energy Materials* **2019**, *9* (19), 1803548.
23. Shinde, A.; Suram, S. K.; Yan, Q.; Zhou, L.; Singh, A. K.; Yu, J.; Persson, K. A.; Neaton, J. B.; Gregoire, J. M., Discovery of Manganese-Based Solar Fuel Photoanodes Via Integration of Electronic Structure Calculations, Pourbaix Stability Modeling, and High-Throughput Experiments. *ACS Energy Letters* **2017**, *2* (10), 2307-2312.
24. McCrory, C. C.; Jung, S.; Ferrer, I. M.; Chatman, S. M.; Peters, J. C.; Jaramillo, T. F., Benchmarking Hydrogen Evolving Reaction and Oxygen Evolving Reaction Electrocatalysts for Solar Water Splitting Devices. *Journal of the American Chemical Society* **2015**, *137* (13), 4347-57.
25. Bae, D.; Seger, B.; Vesborg, P. C.; Hansen, O.; Chorkendorff, I., Strategies for Stable Water Splitting Via Protected Photoelectrodes. *Chemical Society Reviews* **2017**, *46* (7), 1933-1954.
26. Saadi, F. H.; Carim, A. I.; Verlage, E.; Hemminger, J. C.; Lewis, N. S.; Soriaga, M. P., CoP as an Acid-Stable Active Electrocatalyst for the Hydrogen-Evolution Reaction: Electrochemical Synthesis, Interfacial Characterization and Performance Evaluation. *J. Phys. Chem. C* **2014**, *118* (50), 29294-29300.
27. Ledendecker, M.; Mondschein, J. S.; Kasian, O.; Geiger, S.; Göhl, D.; Schalenbach, M.; Zeradjanin, A.; Cherevko, S.; Schaak, R. E.; Mayrhofer, K., Stability and Activity of Non-Noble-Metal-Based Catalysts toward the Hydrogen Evolution Reaction. *Angewandte Chemie International Edition* **2017**, *56* (33), 9767-9771.
28. Seh, Z. W.; Kibsgaard, J.; Dickens, C. F.; Chorkendorff, I.; Nørskov, J. K.; Jaramillo, T. F., Combining Theory and Experiment in Electrocatalysis: Insights into Materials Design. *Science* **2017**, *355* (6321).
29. Boettcher, S. W.; Warren, E. L.; Putnam, M. C.; Santori, E. A.; Turner-Evans, D.; Kelzenberg, M. D.; Walter, M. G.; McKone, J. R.; Brunschwig, B. S.; Atwater, H. A., Photoelectrochemical Hydrogen Evolution Using Si Microwire Arrays. *Journal of the American Chemical Society* **2011**, *133* (5), 1216-1219.
30. Kelzenberg, M. D.; Boettcher, S. W.; Petykiewicz, J. A.; Turner-Evans, D. B.; Putnam, M. C.; Warren, E. L.; Spurgeon, J. M.; Briggs, R. M.; Lewis, N. S.; Atwater, H. A., Enhanced Absorption and Carrier Collection in Si Wire Arrays for Photovoltaic Applications. *Nature Materials* **2010**, *9*, 239.

31. Ardo, S.; Park, S. H.; Warren, E. L.; Lewis, N. S., Unassisted Solar-Driven Photoelectrosynthetic H₂ Splitting Using Membrane-Embedded Si Microwire Arrays. *Energy & Environmental Science* **2015**, *8* (5), 1484-1492.
32. Chen, Y.; Sun, K.; Audesirk, H.; Xiang, C.; Lewis, N. S., A Quantitative Analysis of the Efficiency of Solar-Driven Water-Splitting Device Designs Based on Tandem Photoabsorbers Patterned with Islands of Metallic Electrocatalysts. *Energy & Environmental Science* **2015**, *8* (6), 1736-1747.
33. Sun, K.; Moreno-Hernandez, I. A.; Schmidt, W. C.; Zhou, X.; Crompton, J. C.; Liu, R.; Saadi, F. H.; Chen, Y.; Papadantonakis, K. M.; Lewis, N. S., A Comparison of the Chemical, Optical and Electrocatalytic Properties of Water-Oxidation Catalysts for Use in Integrated Solar-Fuel Generators. *Energy & Environmental Science* **2017**, *10* (4), 987-1002.
34. Trotochaud, L.; Mills, T. J.; Boettcher, S. W., An Optocatalytic Model for Semiconductor-Catalyst Water-Splitting Photoelectrodes Based on in Situ Optical Measurements on Operational Catalysts. *The Journal of Physical Chemistry Letters* **2013**, *4* (6), 931-935.
35. Sun, K.; Saadi, F. H.; Lichterman, M. F.; Hale, W. G.; Wang, H.-P.; Zhou, X.; Plymale, N. T.; Omelchenko, S. T.; He, J.-H.; Papadantonakis, K. M., Stable Solar-Driven Oxidation of Water by Semiconducting Photoanodes Protected by Transparent Catalytic Nickel Oxide Films. *Proceedings of the National Academy of Sciences* **2015**, *112* (12), 3612-3617.
36. Zhou, X.; Liu, R.; Sun, K.; Papadantonakis, K. M.; Brunenschwig, B. S.; Lewis, N. S., 570 Mv Photovoltage, Stabilized N-Si/CoO_x Heterojunction Photoanodes Fabricated Using Atomic Layer Deposition. *Energy & Environmental Science* **2016**, *9* (3), 892-897.
37. Kayes, B. M.; Atwater, H. A.; Lewis, N. S., Comparison of the Device Physics Principles of Planar and Radial P-N Junction Nanorod Solar Cells. *Journal of Applied Physics* **2005**, *97* (11), 114302.
38. Hochbaum, A. I.; Fan, R.; He, R.; Yang, P., Controlled Growth of Si Nanowire Arrays for Device Integration. *Nano Letters* **2005**, *5* (3), 457-460.
39. Warren, E. L.; McKone, J. R.; Atwater, H. A.; Gray, H. B.; Lewis, N. S., Hydrogen-Evolution Characteristics of Ni-Mo-Coated, Radial Junction, n⁺p-Silicon Microwire Array Photocathodes. *Energy & Environmental Science* **2012**, *5* (11), 9653.
40. Shaner, M. R.; McKone, J. R.; Gray, H. B.; Lewis, N. S., Functional Integration of Ni-Mo Electrocatalysts with Si Microwire Array Photocathodes to Simultaneously Achieve High Fill Factors and Light-Limited Photocurrent Densities for Solar-Driven Hydrogen Evolution. *Energy & Environmental Science* **2015**, *8* (10), 2977-2984.
41. Hellstern, T. R.; Benck, J. D.; Kibsgaard, J.; Hahn, C.; Jaramillo, T. F., Engineering Cobalt Phosphide (CoP) Thin Film Catalysts for Enhanced Hydrogen Evolution Activity on Silicon Photocathodes. *Advanced Energy Materials* **2016**, *6* (4).
42. Kempler, P. A.; Gonzalez, M. A.; Papadantonakis, K. M.; Lewis, N. S., Hydrogen Evolution with Minimal Parasitic Light Absorption by Dense Co-P Catalyst Films on Structured P-Si Photocathodes. *ACS Energy Letters* **2018**, *3* (3), 612-617.
43. Yalamanchili, S.; Emmer, H. S.; Fontaine, K. T.; Chen, C. T.; Lewis, N. S.; Atwater, H. A., Enhanced Absorption and <1% Spectrum-and-Angle-Averaged Reflection in Tapered Microwire Arrays. *ACS Photonics* **2016**, *3* (10), 1854-1861.

44. Yalamanchili, S.; Kempler, P. A.; Papadantonakis, K. M.; Atwater, H. A.; Lewis, N. S., Integration of Electrocatalysts with Silicon Microcone Arrays for Minimization of Optical and Overpotential Losses During Sunlight-Driven Hydrogen Evolution. *Sustainable Energy & Fuels* **2019**, *3*, 2227-2236.
45. Saive, R.; Borsuk, A. M.; Emmer, H. S.; Bukowsky, C. R.; Lloyd, J. V.; Yalamanchili, S.; Atwater, H. A., Effectively Transparent Front Contacts for Optoelectronic Devices. *Advanced Optical Materials* **2016**, *4* (10), 1470-1474.
46. Heller, A.; Aspnes, D.; Porter, J.; Sheng, T.; Vadimsky, R., Transparent Metals Preparation and Characterization of Light-Transmitting Platinum Films. *Journal of Physical Chemistry* **1985**, *89* (21), 4444-4452.
47. Bard, A. J.; Faulkner, L. R.; Leddy, J.; Zoski, C. G., *Electrochemical Methods: Fundamentals and Applications*. Wiley New York: 1980; Vol. 2.
48. Cheng, W.-H.; Richter, M. H.; May, M. M.; Ohlmann, J.; Lackner, D.; Dimroth, F.; Hannappel, T.; Atwater, H. A.; Lewerenz, H.-J., Monolithic Photoelectrochemical Device for Direct Water Splitting with 19% Efficiency. *ACS Energy Letters* **2018**, *3* (8), 1795-1800.
49. Zhang, X.; Meng, F.; Mao, S.; Ding, Q.; Shearer, M. J.; Faber, M. S.; Chen, J.; Hamers, R. J.; Jin, S., Amorphous Mo_xCl_y Electrocatalyst Supported by Vertical Graphene for Efficient Electrochemical and Photoelectrochemical Hydrogen Generation. *Energy & Environmental Science* **2015**, *8* (3), 862-868.
50. Zhang, H.; Ding, Q.; He, D.; Liu, H.; Liu, W.; Li, Z.; Yang, B.; Zhang, X.; Lei, L.; Jin, S., A P-Si/NiCoSe_x Core/Shell Nanopillar Array Photocathode for Enhanced Photoelectrochemical Hydrogen Production. *Energy & Environmental Science* **2016**, *9* (10), 3113-3119.
51. Ding, Q.; Zhai, J.; Cabán-Acevedo, M.; Shearer, M. J.; Li, L.; Chang, H. C.; Tsai, M. L.; Ma, D.; Zhang, X.; Hamers, R. J., Designing Efficient Solar-Driven Hydrogen Evolution Photocathodes Using Semitransparent MoQ_xCl_y (Q= S, Se) Catalysts on Si Micropyramids. *Advanced Materials* **2015**, *27* (41), 6511-6518.
52. Ding, Q.; Song, B.; Xu, P.; Jin, S., Efficient Electrocatalytic and Photoelectrochemical Hydrogen Generation Using MoS₂ and Related Compounds. *Chem* **2016**, *1* (5), 699-726.
53. Kempler, P. A.; Richter, M. H.; Cheng, W.-H.; Brunshwig, B. S.; Lewis, N. S., Si Microwire-Array Photocathodes Decorated with Cu Allow CO₂ Reduction with Minimal Parasitic Absorption of Sunlight. *ACS Energy Letters* **2020**.
54. Vijselaar, W.; Westerik, P.; Veerbeek, J.; Tiggelaar, R. M.; Berenschot, E.; Tas, N. R.; Gardeniers, H.; Huskens, J., Spatial Decoupling of Light Absorption and Catalytic Activity of Ni–Mo-Loaded High-Aspect-Ratio Silicon Microwire Photocathodes. *Nature Energy* **2018**, *3* (3), 185-192.
55. Sun, K.; Ritzert, N. L.; John, J.; Tan, H.; Hale, W. G.; Jiang, J.; Moreno-Hernandez, I.; Papadantonakis, K. M.; Moffat, T. P.; Brunshwig, B. S., Performance and Failure Modes of Si Anodes Patterned with Thin-Film Ni Catalyst Islands for Water Oxidation. *Sustainable Energy & Fuels* **2018**, *2* (5), 983-998.
56. Rossi, R. C.; Lewis, N. S., Investigation of the Size-Scaling Behavior of Spatially Nonuniform Barrier Height Contacts to Semiconductor Surfaces Using Ordered Nanometer-Scale Nickel Arrays on Silicon Electrodes. *J. Phys. Chem. B* **2001**, *105* (49), 12303-12318.

57. Bao, X.-Q.; Cerqueira, M. F.; Alpuim, P.; Liu, L., Silicon Nanowire Arrays Coupled with Cobalt Phosphide Spheres as Low-Cost Photocathodes for Efficient Solar Hydrogen Evolution. *Chemical Communications* **2015**, *51* (53), 10742-10745.
58. Vijselaar, W.; Westerik, P.; Veerbeek, J.; Tiggelaar, R. M.; Berenschot, E.; Tas, N. R.; Gardeniers, H.; Huskens, J., Spatial Decoupling of Light Absorption and Catalytic Activity of Ni–Mo-Loaded High-Aspect-Ratio Silicon Microwire Photocathodes. *Nature Energy* **2018**, *1*.
59. Roske, C. W.; Popczun, E. J.; Seger, B.; Read, C. G.; Pedersen, T.; Hansen, O.; Vesborg, P. C. K.; Brunschwig, B. S.; Schaak, R. E.; Chorkendorff, I., et al., Comparison of the Performance of CoP-Coated and Pt-Coated Radial Junction n⁺p-Silicon Microwire-Array Photocathodes for the Sunlight-Driven Reduction of Water to H₂(g). *Journal of Physical Chemistry Letters* **2015**, *6* (9), 1679-1683.
60. Shaner, M. R.; McKone, J. R.; Gray, H. B.; Lewis, N. S., Functional Integration of Ni-Mo Electrocatalysts with Si Microwire Array Photocathodes to Simultaneously Achieve High Fill Factors and Light-Limited Photocurrent Densities for Solar-Driven Hydrogen Evolution. *Energy & Environmental Science* **2015**, *8* (10), 2977-2984.
61. Saadi, F. H.; Carim, A. I.; Drisdell, W. S.; Gul, S.; Baricuatro, J. H.; Yano, J.; Soriaga, M. P.; Lewis, N. S., Operando Spectroscopic Analysis of CoP Films Electrocatalyzing the Hydrogen-Evolution Reaction. *Journal of the American Chemical Society* **2017**, *139* (37), 12927-12930.
62. Döscher, H.; Geisz, J. F.; Deutsch, T. G.; Turner, J. A., Sunlight Absorption in Water – Efficiency and Design Implications for Photoelectrochemical Devices. *Energy & Environmental Science* **2014**, *7* (9), 2951-2956.
63. McIntosh, K. R.; Baker-Finch, S. C. In *Opal 2: Rapid Optical Simulation of Silicon Solar Cells*, Photovoltaic Specialists Conference (PVSC), 2012 38th IEEE, IEEE: 2012; pp 000265-000271.
64. Walter, M. G.; Warren, E. L.; McKone, J. R.; Boettcher, S. W.; Mi, Q.; Santori, E. A.; Lewis, N. S., Solar Water Splitting Cells. *Chemical Reviews*. **2010**, *110*, 6446-6473.
65. Coridan, R. H.; Nielander, A. C.; Francis, S. A.; McDowell, M. T.; Dix, V.; Chatman, S. M.; Lewis, N. S., Methods for Comparing the Performance of Energy-Conversion Systems for Use in Solar Fuels and Solar Electricity Generation. *Energy & Environmental Science* **2015**, *8*, 2886-2901.
66. Zhang, H.; Li, A.; Wang, Z.; Ma, W.; Li, D.; Zong, X.; Li, C., Decorating Mesoporous Silicon with Amorphous Metal–Phosphorous-Derived Nanocatalysts Towards Enhanced Photoelectrochemical Water Reduction. *Journal of Materials Chemistry A* **2016**, *4* (39), 14960-14967.
67. Fukami, K.; Kobayashi, K.; Matsumoto, T.; Kawamura, Y. L.; Sakka, T.; Ogata, Y. H., Electrodeposition of Noble Metals into Ordered Macropores in P-Type Silicon. *Journal of The Electrochemical Society* **2008**, *155* (6), D443.
68. Dasog, M.; Carim, A. I.; Yalamanchili, S.; Atwater, H. A.; Lewis, N. S., Profiling Photoinduced Carrier Generation in Semiconductor Microwire Arrays Via Photoelectrochemical Metal Deposition. *Nano Lett.* **2016**, *16*, 5015-5021.
69. Oh, J.; Deutsch, T. G.; Yuan, H.-C.; Branz, H. M., Nanoporous Black Silicon Photocathode for H₂ Production by Photoelectrochemical Water Splitting. *Energy & Environmental Science* **2011**, *4* (5), 1690.

70. Hori, Y.; Murata, A.; Kikuchi, K.; Suzuki, S., Electrochemical Reduction of Carbon Dioxides to Carbon Monoxide at a Gold Electrode in Aqueous Potassium Hydrogen Carbonate. *Journal of the Chemical Society, Chemical Communications* **1987**, (10), 728-729.
71. Saberi Safaei, T.; Mephram, A.; Zheng, X.; Pang, Y.; Dinh, C.-T.; Liu, M.; Sinton, D.; Kelley, S. O.; Sargent, E. H., High-Density Nanosharp Microstructures Enable Efficient CO₂ Electroreduction. *Nano Letters* **2016**, *16* (11), 7224-7228.
72. Hori, Y.; Murata, A.; Takahashi, R., Formation of Hydrocarbons in the Electrochemical Reduction of Carbon Dioxide at a Copper Electrode in Aqueous Solution. *Journal of the Chemical Society, Faraday Transactions 1: Physical Chemistry in Condensed Phases* **1989**, *85* (8), 2309-2326.
73. Kuhl, K. P.; Cave, E. R.; Abram, D. N.; Jaramillo, T. F., New Insights into the Electrochemical Reduction of Carbon Dioxide on Metallic Copper Surfaces. *Energy & Environmental Science* **2012**, *5* (5), 7050-7059.
74. Kumaravel, V.; Bartlett, J.; Pillai, S. C., Photoelectrochemical Conversion of Carbon Dioxide (CO₂) into Fuels and Value-Added Products. *ACS Energy Letters* **2020**.
75. Karamad, M.; Tripkovic, V.; Rossmeisl, J., Intermetallic Alloys as CO Electroreduction Catalysts—Role of Isolated Active Sites. *ACS Catalysis* **2014**, *4* (7), 2268-2273.
76. Kortlever, R.; Peters, I.; Balemans, C.; Kas, R.; Kwon, Y.; Mul, G.; Koper, M. T., Palladium-Gold Catalyst for the Electrochemical Reduction of CO₂ to C1-C5 Hydrocarbons. *Chemical Communications* **2016**, *52* (67), 10229-32.
77. Torelli, D. A.; Francis, S. A.; Crompton, J. C.; Javier, A.; Thompson, J. R.; Brunshwig, B. S.; Soriaga, M. P.; Lewis, N. S., Nickel-Gallium-Catalyzed Electrochemical Reduction of CO₂ to Highly Reduced Products at Low Overpotentials. *ACS Catalysis* **2016**, *6* (3), 2100-2104.
78. Wang, L.; Nitopi, S.; Wong, A. B.; Snider, J. L.; Nielander, A. C.; Morales-Guio, C. G.; Orazov, M.; Higgins, D. C.; Hahn, C.; Jaramillo, T. F., Electrochemically Converting Carbon Monoxide to Liquid Fuels by Directing Selectivity with Electrode Surface Area. *Nature Catalysis* **2019**, *2* (8), 702-708.
79. Kumar, B.; Atla, V.; Brian, J. P.; Kumari, S.; Nguyen, T. Q.; Sunkara, M.; Spurgeon, J. M., Reduced SnO₂ Porous Nanowires with a High Density of Grain Boundaries as Catalysts for Efficient Electrochemical CO₂-into-HCOOH Conversion. *Angewandte Chemie International Edition* **2017**, *56* (13), 3645-3649.
80. Hu, Y.; Chen, F.; Ding, P.; Yang, H.; Chen, J.; Zha, C.; Li, Y., Designing Effective Si/Ag Interface Via Controlled Chemical Etching for Photoelectrochemical CO₂ Reduction. *Journal of Materials Chemistry A* **2018**, *6* (44), 21906-21912.
81. Kong, Q.; Kim, D.; Liu, C.; Yu, Y.; Su, Y.; Li, Y.; Yang, P., Directed Assembly of Nanoparticle Catalysts on Nanowire Photoelectrodes for Photoelectrochemical CO₂ Reduction. *Nano Letters* **2016**, *16* (9), 5675-5680.
82. Hinogami, R.; Mori, T.; Yae, S.; Nakato, Y., Efficient Photoelectrochemical Reduction of Carbon Dioxide on a P-Type Silicon (P-Si) Electrode Modified with Very Small Copper Particles. *Chemistry letters* **1994**, *23* (9), 1725-1728.
83. Cottineau, T.; Morin, M.; Bélanger, D., Modification of P-Type Silicon for the Photoelectrochemical Reduction of CO₂. *ECS Transactions* **2009**, *19* (35), 1-7.

84. Gurudayal, G.; Beeman, J. W.; Bullock, J.; Wang, H.; Eichhorn, J.; Towle, C.; Javey, A.; Toma, F. M.; Mathews, N.; Ager, J. W., Si Photocathode with Ag-Supported Dendritic Cu Catalyst for CO₂ Reduction. *Energy & Environmental Science* **2019**, *12* (3), 1068-1077.
85. Kim, J.; Summers, D.; Frese Jr, K., Reduction of CO₂ and CO to Methane on Cu Foil Electrodes. *Journal of Electroanalytical Chemistry and Interfacial Electrochemistry* **1988**, *245* (1-2), 223-244.
86. Valkonen, E.; Karlsson, B.; Ribbing, C., Solar Optical Properties of Thin Films of Cu, Ag, Au, Cr, Fe, Co, Ni and Al. *Solar Energy* **1984**, *32* (2), 211-222.
87. Hellstern, T. R.; Nielander, A. C.; Chakthranont, P.; King, L. A.; Willis, J. J.; Xu, S.; MacIsaac, C.; Hahn, C.; Bent, S. F.; Prinz, F. B., Nanostructuring Strategies to Increase the Photoelectrochemical Water Splitting Activity of Silicon Photocathodes. *ACS Applied Nano Materials* **2019**, *2* (1), 6-11.
88. Kuhl, K. P.; Hatsukade, T.; Cave, E. R.; Abram, D. N.; Kibsgaard, J.; Jaramillo, T. F., Electrocatalytic Conversion of Carbon Dioxide to Methane and Methanol on Transition Metal Surfaces. *Journal of the American Chemical Society* **2014**, *136* (40), 14107-14113.
89. Dinh, C.-T.; García de Arquer, F. P.; Sinton, D.; Sargent, E. H., High Rate, Selective, and Stable Electroreduction of CO₂ to CO in Basic and Neutral Media. *ACS Energy Letters* **2018**, *3* (11), 2835-2840.
90. Dinh, C.-T.; Burdyny, T.; Kibria, M. G.; Seifitokaldani, A.; Gabardo, C. M.; de Arquer, F. P. G.; Kiani, A.; Edwards, J. P.; De Luna, P.; Bushuyev, O. S., CO₂ Electroreduction to Ethylene Via Hydroxide-Mediated Copper Catalysis at an Abrupt Interface. *Science* **2018**, *360* (6390), 783-787.
91. Schreier, M.; Héroguel, F.; Steier, L.; Ahmad, S.; Luterbacher, J. S.; Mayer, M. T.; Luo, J.; Grätzel, M., Solar Conversion of CO₂ to CO Using Earth-Abundant Electrocatalysts Prepared by Atomic Layer Modification of CuO. *Nature Energy* **2017**, *2* (7), 17087.
92. Gurudayal, G.; Bullock, J.; Srankó, D. F.; Towle, C. M.; Lum, Y.; Hettick, M.; Scott, M. C.; Javey, A.; Ager, J., Efficient Solar-Driven Electrochemical CO₂ Reduction to Hydrocarbons and Oxygenates. *Energy & Environmental Science* **2017**, *10* (10), 2222-2230.
93. Vijselaar, W.; Tiggelaar, R. M.; Gardeniers, H.; Huskens, J., Efficient and Stable Silicon Microwire Photocathodes with a Nickel Silicide Interlayer for Operation in Strongly Alkaline Solutions. *ACS Energy Letters* **2018**, *3* (5), 1086-1092.
94. Hall, A. S.; Yoon, Y.; Wuttig, A.; Surendranath, Y., Mesostructure-Induced Selectivity in CO₂ Reduction Catalysis. *Journal of the American Chemical Society* **2015**, *137* (47), 14834-14837.
95. Welch, A. J.; DuChene, J. S.; Tagliabue, G.; Davoyan, A.; Cheng, W.-H.; Atwater, H. A., Nanoporous Gold as a Highly Selective and Active Carbon Dioxide Reduction Catalyst. *ACS Applied Energy Materials* **2018**, *2* (1), 164-170.
96. Chen, Y.; Lewis, N. S.; Xiang, C., Operational Constraints and Strategies for Systems to Effect the Sustainable, Solar-Driven Reduction of Atmospheric CO₂. *Energy & Environmental Science* **2015**, *8* (12), 3663-3674.
97. McIntosh, K. R.; Baker-Finch, S. C. In *Opal 2: Rapid Optical Simulation of Silicon Solar Cells*, 2012 38th IEEE Photovoltaic Specialists Conference, 3-8 June 2012; 2012; pp 000265-000271.

98. Rühle, S., Tabulated Values of the Shockley–Queisser Limit for Single Junction Solar Cells. *Solar Energy* **2016**, *130*, 139-147.
99. Cho, S. J.; An, T.; Lim, G., Three-Dimensionally Designed Anti-Reflective Silicon Surfaces for Perfect Absorption of Light. *Chemical Communications* **2014**, *50* (99), 15710-15713.
100. Liu, X.; Coxon, P. R.; Peters, M.; Hoex, B.; Cole, J. M.; Fray, D. J., Black Silicon: Fabrication Methods, Properties and Solar Energy Applications. *Energy & Environmental Science* **2014**, *7* (10), 3223-3263.
101. Yalamanchili, S.; Emmer, H. S.; Lewis, N. S.; Atwater, H. A. In *Highly Absorbing and High Lifetime Tapered Silicon Microwire Arrays as an Alternative for Thin Film Crystalline Silicon Solar Cells*, 2016 IEEE 43rd Photovoltaic Specialists Conference (PVSC), 5-10 June 2016; 2016; pp 2999-3003.
102. Vázquez-Guardado, A.; Boroumand, J.; Franklin, D.; Chanda, D., Broadband Angle-Independent Antireflection Coatings on Nanostructured Light Trapping Solar Cells. *Physical Review Materials* **2018**, *2* (3), 035201.
103. Wang, H.-P.; Sun, K.; Noh, S. Y.; Kargar, A.; Tsai, M.-L.; Huang, M.-Y.; Wang, D.; He, J.-H., High-Performance a-Si/C-Si Heterojunction Photoelectrodes for Photoelectrochemical Oxygen and Hydrogen Evolution. *Nano Letters* **2015**, *15* (5), 2817-2824.
104. Roske, C. W.; Popczun, E. J.; Seger, B.; Read, C. G.; Pedersen, T.; Hansen, O.; Vesborg, P. C. K.; Brunschwig, B. S.; Schaak, R. E.; Chorkendorff, I., et al., Comparison of the Performance of CoP-Coated and Pt-Coated Radial Junction n⁺p-Silicon Microwire-Array Photocathodes for the Sunlight-Driven Reduction of Water to H₂(g). *Journal of Physical Chemistry Letters* **2015**, *6* (9), 1679-1683.
105. Chen, Z.; Ye, S.; Wilson, A. R.; Ha, Y.-C.; Wiley, B. J., Optically Transparent Hydrogen Evolution Catalysts Made from Networks of Copper–Platinum Core–Shell Nanowires. *Energy & Environmental Science* **2014**, *7* (4), 1461-1467.
106. Chen, Y.; Sun, K.; Audesirk, H.; Xiang, C.; Lewis, N. S., A Quantitative Analysis of the Efficiency of Solar-Driven Water-Splitting Device Designs Based on Tandem Photoabsorbers Patterned with Islands of Metallic Electrocatalysts. *Energy & Environmental Science*. **2015**, *8*, 1736-1747.
107. Cabán-Acevedo, M.; Stone, M. L.; Schmidt, J. R.; Thomas, J. G.; Ding, Q.; Chang, H.-C.; Tsai, M.-L.; He, J.-H.; Jin, S., Efficient Hydrogen Evolution Catalysis Using Ternary Pyrite-Type Cobalt Phosphosulphide. *Nature Materials* **2015**, *14*, 1245.
108. Bao, X.-Q.; Fatima Cerqueira, M.; Alpuim, P.; Liu, L., Silicon Nanowire Arrays Coupled with Cobalt Phosphide Spheres as Low-Cost Photocathodes for Efficient Solar Hydrogen Evolution. *Chemical Communications* **2015**, *51* (53), 10742-10745.
109. Dai, P.; Xie, J.; Mayer, M. T.; Yang, X.; Zhan, J.; Wang, D., Solar Hydrogen Generation by Silicon Nanowires Modified with Platinum Nanoparticle Catalysts by Atomic Layer Deposition. *Angewandte Chemie International Edition* **2013**, *52* (42), 11119-11123.
110. Oh, I.; Kye, J.; Hwang, S., Enhanced Photoelectrochemical Hydrogen Production from Silicon Nanowire Array Photocathode. *Nano Letters* **2012**, *12* (1), 298-302.
111. Yablonoitch, E., Statistical Ray Optics. *J. Opt. Soc. Am.* **1982**, *72* (7), 899-907.

112. Sainiemi, L.; Jokinen, V.; Shah, A.; Shpak, M.; Aura, S.; Suvanto, P.; Franssila, S., Non-Reflecting Silicon and Polymer Surfaces by Plasma Etching and Replication. *Advanced Materials* **2011**, *23* (1), 122-126.
113. Fountaine, K. T.; Kendall, C. G.; Atwater, H. A., Near-Unity Broadband Absorption Designs for Semiconducting Nanowire Arrays Via Localized Radial Mode Excitation. *Opt. Express* **2014**, *22* (S3), A930-A940.
114. Fountaine, K. T.; Cheng, W.-H.; Bukowsky, C. R.; Atwater, H. A., Near-Unity Unselective Absorption in Sparse Inp Nanowire Arrays. *ACS Photonics* **2016**, *3* (10), 1826-1832.
115. Coridan, R. H.; Nielander, A. C.; Francis, S. A.; McDowell, M. T.; Dix, V.; Chatman, S. M.; Lewis, N. S., Methods for Comparing the Performance of Energy-Conversion Systems for Use in Solar Fuels and Solar Electricity Generation. *Energy & Environmental Science* **2015**, *8* (10), 2886-2901.
116. Mialhe, P.; Charles, J. P.; Khoury, A.; Bordure, G., The Diode Quality Factor of Solar Cells under Illumination. *Journal of Physics D: Applied Physics* **1986**, *19* (3), 483.
117. Yalamanchili, S.; Lewis, N. S.; Atwater, H. A. In *Role of Doping Dependent Radiative and Non-Radiative Recombination in Determining the Limiting Efficiencies of Silicon Solar Cells*, 2018 IEEE 7th World Conference on Photovoltaic Energy Conversion (WCPEC) (A Joint Conference of 45th IEEE PVSC, 28th PVSEC & 34th EU PVSEC), 10-15 June 2018; 2018; pp 3223-3226.
118. Min, B.; Wagner, H.; Dastgheib-Shirazi, A.; Kimmerle, A.; Kurz, H.; Altermatt, P. P., Heavily Doped Si:P Emitters of Crystalline Si Solar Cells: Recombination Due to Phosphorus Precipitation. *Physica Status Solidi RRL: Rapid Research Letters* **2014**, *8* (8), 680-684.
119. Saive, R.; Bukowsky, C. R.; Yalamanchili, S.; Boccard, M.; Saenz, T.; Borsuk, A. M.; Holman, Z.; Atwater, H. A. In *Effectively Transparent Contacts (Etc) for Solar Cells*, 2016 IEEE 43rd Photovoltaic Specialists Conference (PVSC), 5-10 June 2016; 2016; pp 3612-3615.
120. Saive, R.; Boccard, M.; Saenz, T.; Yalamanchili, S.; Bukowsky, C. R.; Jahelka, P.; Yu, Z. J.; Shi, J.; Holman, Z.; Atwater, H. A., Silicon Heterojunction Solar Cells with Effectively Transparent Front Contacts. *Sustainable Energy & Fuels* **2017**, *1* (3), 593-598.
121. Turner-Evans, D. B.; Emmer, H.; Chen, C. T.; Atwater, H. A., Flexible, Transparent Contacts for Inorganic Nanostructures and Thin Films. *Advanced Materials* **2013**, *25* (29), 4018-4022.
122. Dasog, M.; Carim, A. I.; Yalamanchili, S.; Atwater, H. A.; Lewis, N. S., Profiling Photoinduced Carrier Generation in Semiconductor Microwire Arrays Via Photoelectrochemical Metal Deposition. *Nano Lett.* **2016**, *16* (8), 5015-5021.
123. Spurgeon, J. M.; Plass, K. E.; Kayes, B. M.; Brunshwig, B. S.; Atwater, H. A.; Lewis, N. S., Repeated Epitaxial Growth and Transfer of Arrays of Patterned, Vertically Aligned, Crystalline Si Wires from a Single Si (111) Substrate. *Applied Physics Letters* **2008**, *93* (3), 032112.
124. Shaner, M. R.; Fountaine, K. T.; Ardo, S.; Coridan, R. H.; Atwater, H. A.; Lewis, N. S., Photoelectrochemistry of Core-Shell Tandem Junction N-P⁺-Si/N-WO₃ Microwire Array Photoelectrodes. *Energy & Environmental Science* **2014**, *7* (2), 779-790.

125. Shaner, M. R.; McDowell, M. T.; Pien, A.; Atwater, H. A.; Lewis, N. S., Si/TiO₂ Tandem-Junction Microwire Arrays for Unassisted Solar-Driven Water Splitting. *Journal of The Electrochemical Society* **2016**, *163* (5), H261-H264.
126. Verlage, E.; Hu, S.; Liu, R.; Jones, R. J.; Sun, K.; Xiang, C.; Lewis, N. S.; Atwater, H. A., A Monolithically Integrated, Intrinsically Safe, 10% Efficient, Solar-Driven Water-Splitting System Based on Active, Stable Earth-Abundant Electrocatalysts in Conjunction with Tandem III–V Light Absorbers Protected by Amorphous TiO₂ Films. *Energy & Environmental Science* **2015**, *8* (11), 3166-3172.
127. Kang, D.; Young, J. L.; Lim, H.; Klein, W. E.; Chen, H.; Xi, Y.; Gai, B.; Deutsch, T. G.; Yoon, J., Printed Assemblies of GaAs Photoelectrodes with Decoupled Optical and Reactive Interfaces for Unassisted Solar Water Splitting. *Nature Energy* **2017**, *2* (5), 17043.
128. Degani, Y.; Sheng, T.; Heller, A.; Aspnes, D.; Studna, A.; Porter, J., “Transparent” Metals: Preparation and Characterization of Light-Transmitting Palladium, Rhodium, and Rhenium Films. *Journal of Electroanalytical Chemistry and Interfacial Electrochemistry* **1987**, *228* (1-2), 167-178.
129. Heller, A.; Aharon-Shalom, E.; Bonner, W.; Miller, B., Hydrogen-Evolving Semiconductor Photocathodes: Nature of the Junction and Function of the Platinum Group Metal Catalyst. *Journal of the American Chemical Society* **1982**, *104* (25), 6942-6948.
130. Aspnes, D.; Heller, A.; Porter, J., Microstructurally Engineered, Optically Transmissive, Electrically Conductive Metal Films. *Journal of Applied Physics* **1986**, *60* (9), 3028-3034.
131. McEnaney, J. M.; Crompton, J. C.; Callejas, J. F.; Popczun, E. J.; Read, C. G.; Lewis, N. S.; Schaak, R. E., Electrocatalytic Hydrogen Evolution Using Amorphous Tungsten Phosphide Nanoparticles. *Chemical Communications* **2014**, *50* (75), 11026-11028.
132. Popczun, E. J.; McKone, J. R.; Read, C. G.; Biacchi, A. J.; Wiltrout, A. M.; Lewis, N. S.; Schaak, R. E., Nanostructured Nickel Phosphide as an Electrocatalyst for the Hydrogen Evolution Reaction. *Journal of the American Chemical Society* **2013**, *135* (25), 9267-9270.
133. Popczun, E. J.; Read, C. G.; Roske, C. W.; Lewis, N. S.; Schaak, R. E., Highly Active Electrocatalysis of the Hydrogen Evolution Reaction by Cobalt Phosphide Nanoparticles. *Angew. Chem. Int. Ed.* **2014**, *53* (21), 5427-5430.
134. Kibsgaard, J.; Tsai, C.; Chan, K.; Benck, J. D.; Nørskov, J. K.; Abild-Pedersen, F.; Jaramillo, T. F., Designing an Improved Transition Metal Phosphide Catalyst for Hydrogen Evolution Using Experimental and Theoretical Trends. *Energy & Environmental Science* **2015**, *8* (10), 3022-3029.
135. Stern, L.-A.; Liardet, L.; Mayer, M. T.; Morales-Guio, C. G.; Grätzel, M.; Hu, X., Photoelectrochemical Deposition of CoP on Cuprous Oxide Photocathodes for Solar Hydrogen Production. *Electrochimica Acta* **2017**, *235*, 311-316.
136. Aspnes, D. E., Optical Properties of Thin Films. *Thin Solid Films* **1982**, *89* (3), 249-262.
137. Palik, E. D., *Handbook of Optical Constants of Solids*. Academic press: 1998; Vol. 3.
138. Sihvola, A. H.; Kong, J. A., Effective Permittivity of Dielectric Mixtures. *IEEE Transactions on Geoscience and Remote Sensing* **1988**, *26* (4), 420-429.

139. Izhar, S.; Nagai, M., Transition Metal Phosphide Catalysts for Hydrogen Oxidation Reaction. *Catalysis Today* **2009**, *146* (1-2), 172-176.
140. Jin, S., Are Metal Chalcogenides, Nitrides, and Phosphides Oxygen Evolution Catalysts or Bifunctional Catalysts? *ACS Energy Letters* **2017**, *2* (8), 1937-1938.
141. Stern, L.-A.; Feng, L.; Song, F.; Hu, X., Ni₂P as a Janus Catalyst for Water Splitting: The Oxygen Evolution Activity of Ni₂P Nanoparticles. *Energy & Environmental Science* **2015**, *8* (8), 2347-2351.
142. Peñas, P.; van der Linde, P.; Vijselaar, W.; van der Meer, D.; Lohse, D.; Huskens, J.; Gardeniers, H.; Modestino, M. A.; Rivas, D. F., Decoupling Gas Evolution from Water-Splitting Electrodes. *Journal of The Electrochemical Society* **2019**, *166* (15), H769-H776.
143. Kocha, S. S.; Montgomery, D.; Peterson, M. W.; Turner, J. A., Photoelectrochemical Decomposition of Water Utilizing Monolithic Tandem Cells. *Solar Energy Materials and Solar Cells* **1998**, *52* (3-4), 389-397.
144. Davis, G. E., Scattering of Light by an Air Bubble in Water. *JOSA* **1955**, *45* (7), 572-581.
145. Dorfi, A. E.; West, A. C.; Esposito, D. V., Quantifying Losses in Photoelectrode Performance Due to Single Hydrogen Bubbles. *The Journal of Physical Chemistry C* **2017**, *121* (48), 26587-26597.
146. Leenheer, A. J.; Atwater, H. A., Water-Splitting Photoelectrolysis Reaction Rate via Microscopic Imaging of Evolved Oxygen Bubbles. *Journal of The Electrochemical Society* **2010**, *157* (9), B1290.
147. Holmes-Gentle, I.; Bedoya-Lora, F.; Alherish, F.; Hellgardt, K., Optical Losses at Gas Evolving Photoelectrodes: Implications for Photoelectrochemical Water Splitting. *The Journal of Physical Chemistry C* **2018**, *123* (1), 17-28.
148. Kern, W., The Evolution of Silicon Wafer Cleaning Technology. *Journal of the Electrochemical Society* **1990**, *137* (6), 1887.
149. Osseo-Asare, K.; Wei, D.; Mishra, K. K., Dissolution Windows for Wet Chemical Processing of Silicon and Silicon Dioxide: Potential-Ph Diagrams for the Si-F-H₂O System. *Journal of the Electrochemical Society* **1996**, *143* (2), 749.
150. Hu, S.; Shaner, M. R.; Beardslee, J. A.; Lichterman, M.; Brunschwig, B. S.; Lewis, N. S., Amorphous TiO₂ Coatings Stabilize Si, Gaas, and Gap Photoanodes for Efficient Water Oxidation. *Science* **2014**, *344* (6187), 1005-1009.
151. Kempler, P. A.; Coridan, R. H.; Lewis, N. S., Effects of Bubbles on the Electrochemical Behavior of Hydrogen-Evolving Si Microwire Arrays Oriented against Gravity. *Energy & Environmental Science* **2020**, *13*, 1808-1817.
152. Fernandez, D.; Maurer, P.; Martine, M.; Coey, J.; Möbius, M. E., Bubble Formation at a Gas-Evolving Microelectrode. *Langmuir* **2014**, *30* (43), 13065-13074.
153. Janssen, L.; Hoogland, J., The Effect of Electrolytically Evolved Gas Bubbles on the Thickness of the Diffusion Layer—II. *Electrochimica Acta* **1973**, *18* (8), 543-550.
154. Vogt, H.; Stephan, K., Local Microprocesses at Gas-Evolving Electrodes and Their Influence on Mass Transfer. *Electrochimica Acta* **2015**, *155*, 348-356.
155. Peñas, P.; van der Linde, P.; Vijselaar, W.; van der Meer, D.; Lohse, D.; Huskens, J.; Gardeniers, H.; Modestino, M. A.; Rivas, D. F., Decoupling Gas Evolution from Water-Splitting Electrodes. *Journal of The Electrochemical Society* **2019**, *166* (15), H769.

156. Trotochaud, L.; Young, S. L.; Ranney, J. K.; Boettcher, S. W., Nickel–Iron Oxyhydroxide Oxygen-Evolution Electrocatalysts: The Role of Intentional and Incidental Iron Incorporation. *Journal of the American Chemical Society* **2014**, *136* (18), 6744-6753.
157. Smith, T., The Hydrophilic Nature of a Clean Gold Surface. *Journal of Colloid and Interface Science* **1980**, *75* (1), 51-55.
158. Erb, R. A., Wettability of Metals under Continuous Condensing Conditions. *The Journal of Physical Chemistry* **1965**, *69* (4), 1306-1309.
159. Lubetkin, S., The Fundamentals of Bubble Evolution. *Chemical Society Reviews* **1995**, *24* (4), 243-250.
160. Cui, Z.; Takoudis, C. G., Initial Oxidation of H-Terminated Si (100) in O₃ (950 ppm)/O₂ and Pure O₂. *Journal of The Electrochemical Society* **2003**, *150* (11), G694.
161. Esposito, D. V.; Lee, Y.; Yoon, H.; Haney, P. M.; Labrador, N. Y.; Moffat, T. P.; Talin, A. A.; Szalai, V. A., Deconvoluting the Influences of 3d Structure on the Performance of Photoelectrodes for Solar-Driven Water Splitting. *Sustainable Energy & Fuels* **2017**, *1* (1), 154-173.
162. Leistra, J. A.; Sides, P. J., Voltage Components at Gas Evolving Electrodes. *Journal of The Electrochemical Society* **1987**, *134* (10), 2442-2446.
163. van der Linde, P.; Peñas-López, P.; Soto, Á. M.; van der Meer, D.; Lohse, D.; Gardeniers, H.; Rivas, D. F., Gas Bubble Evolution on Microstructured Silicon Substrates. *Energy & Environmental Science* **2018**, *11* (12), 3452-3462.
164. Kingsbury, D. L.; Marston, P. L., Mie Scattering near the Critical Angle of Bubbles in Water. *JOSA* **1981**, *71* (3), 358-361.
165. Warren, E. L.; Boettcher, S. W.; Walter, M. G.; Atwater, H. A.; Lewis, N. S., pH-Independent, 520 mV Open-Circuit Voltages of Si/Methyl Viologen^{2+/+} Contacts through Use of Radial N+ P-Si Junction Microwire Array Photoelectrodes. *The Journal of Physical Chemistry C* **2011**, *115* (2), 594-598.
166. Fortune, W.; Mellon, M., Determination of Iron with O-Phenanthroline: A Spectrophotometric Study. *Industrial & Engineering Chemistry Analytical Edition* **1938**, *10* (2), 60-64.